Nanotechnological and material science for diabetics and advanced transdermal delivery

Anna Voronova

Thèse de doctorat

Présentée à l'Université de Lille

Ecole Doctorale Sciences pour l'Ingénieur

Micro-, nano-systèmes et capteurs

par Anna Voronova

La délivrance transdermique des médicaments par la nanotechnologie et la science des matériaux : de nouvelles avancées pour la médicine personnalisée du diabète

Soutenue le 14 Octobre 2021 devant le jury composé de :

Rapporteur	Dr. Stéphane DALLE	Institute de Génomique Fonctionnelle (IGF), Montpellier
Rapporteur	Prof. Sylvain GABRIELE	Université de Mons, Belgique
Examinatrice	Dr. Eva JAKAB-TOTH	Centre de Biophysique Moléculaire, CNRS-Orleans
Présidente du jury/ Examinatrice	Prof. Catherine FOULON	Université de Lille
Invité	Dr. Thomas HUBERT	Université de Lille
Directrice de thèse	Prof. Sabine SZUNERITS	Université de Lille
Co-Directeur de thèse	Prof. Amar ABDERRAHMANI	Université de Lille

Doctoral thesis

Presented at the University of Lille

Ecole Doctorale Sciences pour l'Ingénieur

Micro-, nano-systèmes et capteurs

by Anna Voronova

Nanotechnological and material science for diabetics and advanced transdermal delivery

Defended on the 14th of October 2021 before the following committee :

Reviewer	Dr. Stéphane DALLE	Institute of Functional Genomics, Montpellier
Reviewer	Prof. Sylvain GABRIELE	University of Mons, Belgium
Examiner	Dr. Eva JAKAB-TOTH	Center for Molecular Biophysics, CNRS-Orleans
President/ Examiner	Prof. Catherine FOULON	University of Lille
Invited	Dr. Thomas HUBERT	University of Lille
Director	Prof. Sabine SZUNERITS	University of Lille
Co-Director	Prof. Amar ABDERRAHMANI	University of Lille

Blank page

ABSTRACT

The refinement of current drug delivery systems is key for the development of personalized medicine (PM). The rapid progress in materials science and nanotechnology over the last 10 years have allowed true major advances in controlled drug delivery systems. So far, it is possible to deliver drugs through many routes, such as buccal, oral, rectal, parenteral, and mucous membranes. The transdermal administration (TDD) also emerges as an attractive route for delivering drugs and thereby, as a key delivery mode for implementing PM. Indeed, this route offers the advantage of being able to administer drugs which are little or not tolerated when ingested or inhaled, and also of avoiding their degradation by the gastrointestinal system. Additionally, TDD, if non-invasive, may ameliorate the therapeutic efficacy of the drug by improving the adherence to the treatment for patients with chronic disease. For example, TDD may be an alternative for administrating antidiabetics with adverse side effects and/or parenterally injected via needles. However, the administration of drugs by TDD, in a controlled manner and on demand, remains a technological barrier to be overcome. In this thesis, we investigated different approaches to control the non-invasive TDD delivery of insulin and metformin, such as the use of heat in combination with graphene oxide matrices. *In vitro* and *in vivo* tests were carried out to evaluate the effectiveness of the proposed concepts. In addition, mats of electrospun fibers with incorporated graphene have been investigated for oral rather than transdermal drug delivery. Furthermore, the use of nanostructures to inhibit the aggregation of IAPP (Islet Amyloid Polypeptide) and the first promising results will be discussed.

Keywords: diabetes; transdermal delivery; protein aggregation; nanomaterials

RÉSUMÉ

Les avancées remarquables qui ont été réalisées ces dernières années dans la science des matériaux et dans la nanotechnologie, ont permis de faire des progrès importants dans les modes de délivrance de médicaments, et ainsi de progresser dans le développement de la médecine personnalisée (MP). Aujourd'hui, des médicaments peuvent être administrés par de nombreuses voies, comme la voie buccale, orale, rectale, parentérale et des muqueuses. Une autre voie d'administration de médicaments extrêmement pertinente pour la MP du diabète est la voie transdermique (TD). Cette voie offre un avantage de pouvoir administrer des médicaments qui sont peu ou pas tolérés lorsqu'ils sont ingérés ou inhalés, et aussi d'éviter leur dégradation par le système gastro-intestinale. En plus, la TD, si elle est non-invasive, peut améliorer l'efficacité thérapeutique du médicament en améliorant adhésion thérapeutique des patients. Cependant, l'administration de médicaments par TD, de manière contrôlée et à la demande, reste un verrou technologique à surmonter. Dans cette thèse, nous avons étudié différentes approches permettant de contrôler la délivrance non-invasive TD d'insuline et de metformine, comme l'utilisation de la chaleur en combinaison avec des matrices d'oxyde de graphène. Des tests *in vitro* et *in vivo* ont été réalisés pour évaluer l'efficacité des concepts proposés. De plus, des tapis de fibres électrofilées avec du graphène incorporé ont été étudiés pour l'administration de médicaments par voie buccale plutôt que par voie transdermique. En outre, l'utilisation de nanostructures pour inhiber l'agrégation de l'*IAPP* (Islet Amyloid Polypeptide) et les premiers résultats prometteurs sont discutés.

Mots clés: diabète; administration transdermique; agrégation des protéines; nanomatériaux

ACKNOWLEDGEMENTS

This thesis is based on the research conducted in NanoBioInterfaces group (NBI) at the Institute of Electronics, Microelectronics and Nanotechnology (IEMN).

First of all, my gratitude and professional appreciation go to my supervisors Prof. Sabine Szunerits and Prof. Amar Abderrahmani, who made this work possible. Thank you for providing me with extensive personal and professional guidance, continuous support, motivation and patience in corrections of the manuscript.

The completion of this study could not be possible without help of Dr. Rabah Boukherroub, Dr. Alexandre Barras, Dr. Valérie Abderrahmani, Dr. Valérie Pawlowski and Quentin Pagneux. Thank you for all the precious knowledge you shared with me, your suggestions, valuable discussions and accessibility.

I want to thank all former and present colleagues of NanoBioInterfaces group, especially Chengnan Li, Léa Rosselle, Aleksandra Łoczechin, Milica Budimir, Mathias Dolci, Ioana Silvia Hosu, Michele Lodato, Teresa Rodrigues, Inès de Hoon… It was my pleasure to work with you as well as to share unforgettable moments in Lille.

My appreciation would be incomplete without giving credit to the members of Institute of Agrochemistry and Food Technology (IATA), Valencia, Spain, in particular to Cristina Prieto, Maria Pardo Figuerez and Prof. Jose Maria Lagaron, who have equipped me with essential skills of electrospinning technique.

Special thanks go to I-SITE project and the University of Lille for funding of this PhD fellowship.

I would like to acknowledge and give my warmest thanks to my family. Even being far away, I felt all your love and support in good and bad times.

Finally to my caring and supporting Vlad. Thank you to believe in me.

TABLE OF CONTENTS

ABSTRACT **4**

RÉSUMÉ **5**

ACKNOWLEDGEMENTS **6**

OBJECTIVES **11**

CHAPTER 1 ..... **12**

Diabetes and approaches for administration of antidiabetic drugs **12**

1.1. Introduction to the pathology of diabetes 12

1.2. Pathophysiology of diabetes 13

1.3. Complications related to diabetes 16

1.4. Drug administration strategies for diabetes therapy 17

1.4.1. Treatment of type 2 diabetes 19

1.4.2. Treatment of type 1 diabetes 21

1.5. From drug administration to treatment of β-cells via islet amyloid disaggregation 32

CHAPTER 2: **35**

Mucoadhesive electrospun patches for buccal delivery of insulin **35**

2.1. Introduction 35

2.2. Fabrication and characteristics of mucoadhesive PAA@rGO fiber mats 36

2.3. Insulin-loaded mucoadhesive PAA@rGO patches 39

2.4. *Ex vivo* insulin permeation studies 41

2.5. *In vivo* mucoadhesive properties and acceptability of PAA@rGO nanofibers mats by volunteers 44

2.6. Conclusion 45

CHAPTER 3: **46**

***In vivo* studies of minimally invasive insulin loaded insoluble microneedles on pigs** **46**

3.1. Introduction 46

3.2. Fabrication of MoS_2 loaded microneedles based on GelMA and PEGDA hydrogel 48

3.3. *In vitro* characterization of insulin-loaded MoS_2-MNs patch 49

3.4. *In vitro* pharmacodynamic response of insulin-loaded MoS_2-MNs array patch 50

3.5. *In vivo* pharmacodynamic response of insulin-loaded MoS_2-MNs array patch 52

3.6. Conclusion 52

CHAPTER 4: 53

Near-infrared light activatable hydrogels for metformin delivery 53

4.1. Introduction 53

4.2. Metformin hydrogels using graphene oxide (GO) as a cross-linker 55

4.3. Metformin hydrogels using reduced graphene oxide (rGO-COOH) as a cross-linker. 58

4.4. NIR light triggered transdermal metformin release 60

4.5. Influence of temperature on skin structure 62

4.6. *In vivo* studies 63

4.7. Conclusion 64

CHAPTER 5 65

Carbon nanostructures for islet amyloid desintegration 65

5.1. Introduction 65

5.2. Carbon quantum dots synthesis and characterization 66

5.3. Formation of hIAPP aggregates and an effect of carbon quantum dots on its disaggregation 71

5.4. The role of diabetogenic factors on the human amyloidogenesis process 73

CHAPTER 6: 76

Conclusions and perspectives 76

APPENDIX 78

S1. Chemicals 78

S2. Synthesis 79

S2.1. Carboxylic acid enriched reduced graphene oxide (rGO-COOH) 79

S2.2. Fabrication of metformin hydrogels 79

S2.3. Fabrication of PAA@rGO nanofiber mats via electrospinning 79

S2.4. Synthesis of Gelatin Methacrylate (GelMA) 79

S2.5. Preparation of microneedles (MNs) 80

S2.5.1. PDMS mold fabrication 80

S2.5.2. Microneedles' fabrication 80

S2.6. Carbon quantum dots (CQDs) 80

S2.6.1. CQD-1 (carboxylated carbon quantum dots) 80

S2.6.2. CQD-2 (aminated carbon quantum dots) 81

S2.6.3. CQD-3 (fluorinated carbon quantum dots) 81

S3. Characterisations of nanofiber mats 81

S3.1. Swelling degree 81

S3.2. Weight and thickness 82

S4. Drug loading 82

S4.1. Insulin loaded PAA@rGO electrospun nanofibers 82

S4.2. Insulin loaded MoS_2-MNs 82

S5. *Ex vivo* permeation experiments 82

S5.1. Murine skin for metformin loaded hydrogels 82

S5.2. Porcine buccal mucosa and cornea for insulin loaded PAA@rGO nanofibers 83

S6. *In vivo* insulin experiments on pigs 84

S7. *In vitro* photothermal drug release studies 84

S8. Tissue staining 84

S9. Tissue imaging 85

S10. Biological assays 85

S10.1. Determination of metformin activity 85

S10.2. Determination of insulin activity 86

S10.3. Cytotoxicity tests of PAA@rGO bandage 86

S10.4. Cytotoxicity tests of CQDs 87

S10.5. Thioflavin T kinetics assay 87

S10.6. Influence of glucose on hIAPP aggregation 87

S10.7. Influence of palmitate on hIAPP aggregation 88

S10.8. Preparation of peptides (hIAPP, APP) and heterocomplexes (IAPP/APP) 88

S10.9. Western blotting of APP/IAPP aggregates 88

S10.10. Cytotoxicity of heterocomplexes (IAPP/APP) in diabetogenic condition 88

S11. Instrumentation 89

S11.1. Fourier transform infrared spectroscopy (FT-IR) 89

S11.2. Raman spectroscopy measurements 89

S11.3. Scanning electron microscopy (SEM) 89
S11.4. Transmission electron microscopy (TEM) 90
S11.5. Atomic force microscopy (AFM) 90
S11.6. pH measurements 90
S11.7. High-performance Liquid Chromatography (HPLC) 90
S11.8. Microwave reactor 90
S11.9. Size and zeta-potential measurements 90
S11.10. X-ray photoelectron spectroscopy (XPS) 90
S11.11. UV-Vis Absorption 91
S11.12. Fluorescence spectroscopy 91
S11.13. Photothermal effect measurements 91
S11.14. Adhesive strength measurements 91
PUBLICATIONS 92
REFERENCES 93
ABBREVIATIONS AND ACRONYMS 117

OBJECTIVES

This thesis is dedicated to the development of materials and approaches for sufficient delivery of antidiabetic drugs through skin and buccal mucosa, as well as for investigation of the effect of carbon-based materials, in particular carbon quantum dots (CQDs), on islet amyloid aggregates. Different fields of research such as chemical synthesis and material characterization, molecular biology and animal studies will be combined.

Chapter 1 gives a general introduction into the diabetes as a pathology, its types, strategies of treatment and complications. It also highlights the overview of nanomaterials currently used for drug delivery. Different approaches of antidiabetic drugs administration such as subcutaneous, nasal, pulmonary, oral and transdermal will be presented. The last two will be discussed in details, as they were basically used for drug delivery in this thesis. In addition, the concept of islet amyloid polypeptide (IAPP) aggregation will be outlined.

Chapter 2 describes the fabrication of mucoadhesive patch from poly(acrylic acid) (PAA) and β-cyclodextrin using electrospinning technique. Reduced graphene oxide (rGO) was added to the blend in order to endow the patch with photothermal properties. Loaded with insulin, the mucoadhesive mats were tested for on-demand drug delivery under near-infrared (NIR) irradiation *ex vivo* on buccal and corneal tissues.

Chapter 3, is devoted to the testing of photothermally active microneedles prepared from gelatin methacrylate (GelMA) crosslinked with polyethylene glycol diacrylate (PEGDA) and integrated with molybdenum sulfide nanosheets (MoS_2 NSs). These microneedles were applied to porcine ear *in vivo* and blood glucose level (BGL) and insulin concentration were determined.

Chapter 4 outlines transdermal delivery of metformin from light responsive hydrogel. It was found that metformin hydrochloride, the first line drug in the management of type 2 diabetes, can form hydrogels when mixed with graphene oxide (GO) and carboxylated reduced graphene oxide (rGO-COOH) as cross-linkers, based on gelation process. The results of *in vitro* penetration of metformin through human skin will be presented.

Chapter 5 is dedicated to the study of islet amyloid polypeptide (IAPP) fibrillation and an influence of glucose, free fatty acids and β-amyloid on formation of aggregates. The potential of synthesized CQDs to disaggregate islet amyloid polypeptide complexes will be investigated.

Chapter 6 summarizes the results and presents some perspectives on the work.

CHAPTER 1

Diabetes and approaches for administration of antidiabetic drugs

1.1. Introduction to the pathology of diabetes

Diabetes is a group of metabolic diseases defined by a chronically elevated blood glucose level (BGL). There are four types of diabetes including type 1 diabetes (T1D), type 2 diabetes (T2D), gestational diabetes and other diabetes. In TD1, patients cannot produce insulin as a result of an autoimmune destruction of the insulin producing cells within the pancreas, known as β-cells. T2D is characterized by insulin resistance, which corresponds to the deficiency in cellular response to insulin. In non-treated or badly controlled type 1 and type 2 diabetes, hyperglycemia and hypoglycaemia, ensue. Hyperglycemia can lead to a variety of syndromes, notably cardiovascular and neurological complications, while hypoglycaemia results in a lack of energy and ultimately death.

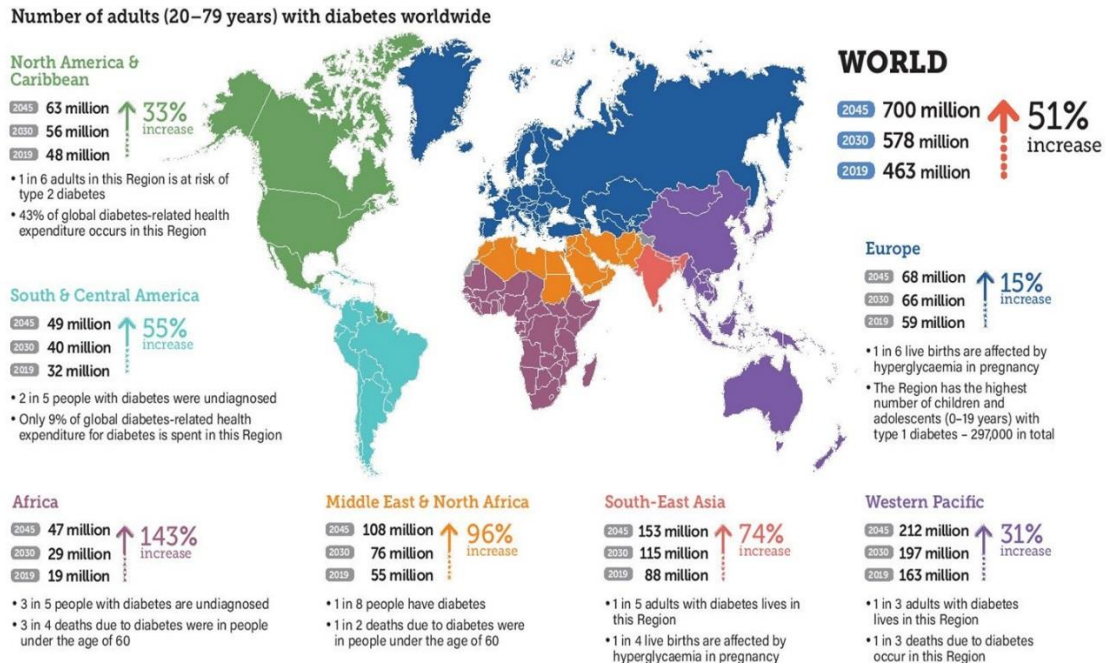

Figure 1.1. Worldwide distribution of adults with diabetes. Prediction of the World Health Organization (WHO) of diabetic patients from 2019 to 2045 in different parts of the world (reproduced with permission from ref.[1]).

The vast interest in finding treatments of people with diabetes is notably linked to the alarming projections from the world health organization (WHO), which predicts approximately 700 million people worldwide to be affected by 2045 (**Figure 1.1**).[1] Diabetes is thus becoming one of the largest public health challenges globally. Diabetes causes 5 million deaths annually in developed countries, mainly due to cardiovascular disease (50%) and kidney failure (10-20%).[2] Diabetes is also one of the leading causes of blindness, 50% of lower limb amputations, and provokes severe complications in viral infections, like COVID-19.[3]. In addition, diabetes increases rapidly at younger ages decreasing considerably the life expectation of the younger generation, becoming lower than that of their parents (**Figure 1.1**).

1.2. Pathophysiology of diabetes

Diabetes is classified according to pathophysiological mechanisms into type 2 diabetes (T2D), type 1 diabetes (T1D) and gestational diabetes mellitus, diabetes diagnosed in the second or third trimester of pregnancy (**Figure 1.2a**).[4] To the three types of diabetes, has to be added other types of diabetes, which result from other causes, diseases of the exocrine pancreas, like cystic fibrosis, and drug- or chemical-induced diabetes such as in the treatment of HIV/AIDS or after organ transplantation.

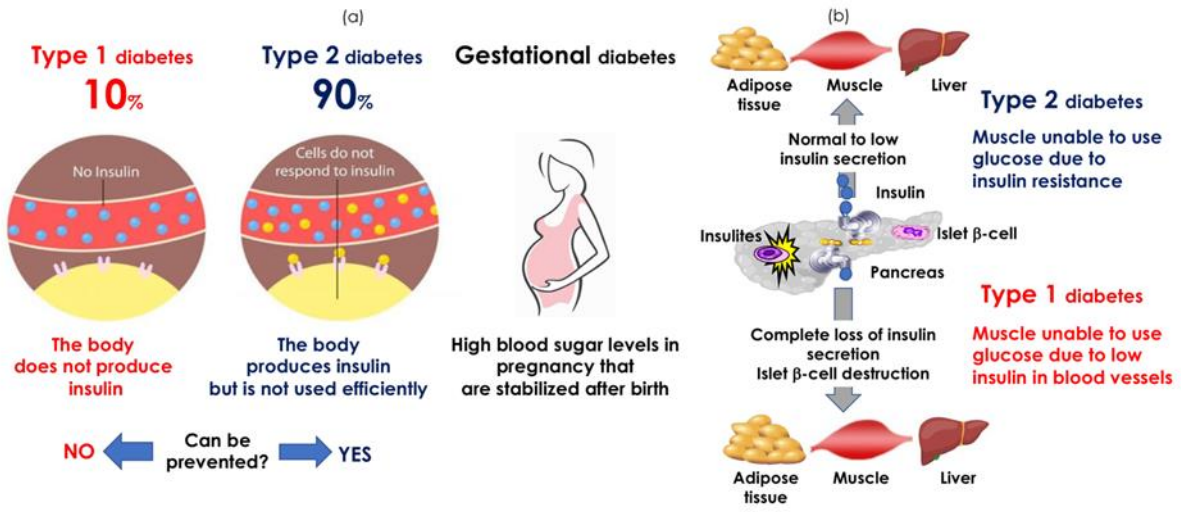

Figure 1.2. Pathophysiology of diabetes. (**a**) Classification of diabetes according to pathophysiological mechanisms. (**b**) Consequences of relative and absolute deficiency of insulin production by islet β-cells. In type 1 diabetes, absolute deficiency of insulin caused by autoimmune destruction of β-cells (insulites) leads to the absence of glucose uptake and metabolism in insulin-sensitive organs including muscle, adipose tissue and liver. Therefore, glucose stays in the blood circulation, possibly leading to diabetic ketoacidosis in the case of a viral infection. In type 2 diabetes, the insulin-sensitive organs become resistant to insulin action

due to the impaired intracellular insulin receptor signaling. Despite the still functioning β-cells, insulin production is insufficient to compensate for insulin resistance. (adapted from https://visual.ly/community/Infographics/health/diabetes-type-1-diabetes-vs-type-2-diabetes and http://www.patiadiabetes.com/en/patia/diabetes/).

Type 2 diabetes (T2D) is the most prominent form with more than 90% of diagnosed cases.[5-7] As obesity itself causes some degree of insulin resistance[8-9], most patients with this form of diabetes are obese or have an increased percentage of body fat distributed predominantly in the abdominal region. In T2D, hyperglycaemia ensues as pancreatic β-cells fail to produce enough insulin to compensate for insulin resistance.[10] The β-cell dysfunction is characterized by impaired insulin secretion in response to glucose (**Figure 1.2b**), which progressively is exacerbated by the loss of β-cell mass (BCM). The risk of developing T2D increases with age, obesity, and lack of physical activity. It occurs more frequently in women with prior gestational diabetes and in individuals with hypertension or dyslipidaemia.[11] Its frequency varies in different racial and ethnic subgroups.[12]

Type 1 diabetes (T1D) represents around 10% of the diabetes diagnosed forms and results from autoimmune destruction of the pancreatic β-cells.[13] Genetic factors contribute to the risk of T1D although the environment including virus, bacteria, pollutants and nutrition is the predominant factor. More than 40 susceptible genes have been identified so far, with the gene coding for human leukocyte antigens (HLA) as the predominant one for predicting the risk of T1D. Some of the risk factors of developing diabetes are presented in **Table 1.1**.

Genetic variation within the HLA gene accounts for approximately 40 - 50% of familial aggregation of T1D.[14] In T1D, the rate of β-cell destruction is strongly variable, being rapid in some individuals, mainly infants and children, and slow in others, notably adults. At an advanced stage of the disease, there is little or no insulin secretion, as manifested by low or undetectable levels of plasma C-peptide.

Other forms of diabetes include familial and genetic forms of diabetes in which mutations within a single gene potentially lead to defective insulin secretion, as exemplified by Maturity Onset of the Diabetes of the Young (MODY). MODY is a group of inherited disorders that account for 1 - 5% of all cases of diagnosed diabetes and 1 - 6% of all pediatric diabetes cases.[15] Usually, MODY onset ensues before 45 years of age. The disease is characterized by autosomal dominant inheritance. In other words, only one mutated gene from parents is sufficient to be affected by this type of disorder. In this case, the father or mother has a 50% chance of having

an affected child with one abnormal gene and a 50% chance of having an unaffected child with two normal genes. Unlike T1D, MODY patients have no β-cell autoimmunity whereas they have β-cell dysfunction. Mutations in genes playing a key role in β-cell function (BCF) and survival are thought to cause β-cell dysfunction and thereby the onset of MODY.

Table 1.1. The main risk factors that influence the development of type 1, type 2 and gestational diabetes (adapted from https://my.clevelandclinic.org/health/diseases/7104-diabetes-mellitus-an-overview).

<table>
<tr><th>Type 1 diabetes</th><th>Type 2 and gestational diabetes</th></tr>
<tr><td colspan="2">• Family history (parent or sibling with certain type of diabetes)</td></tr>
<tr><td rowspan="3">• Injury to the pancreas (by infection, tumor, surgery or accident)</td><td>• Overweight/Obesity</td></tr>
<tr><td>• Race (American, Hispanic, Native American, Asian-American race, Pacific Islander.</td></tr>
<tr><td>• Age (45 and older for type 2 diabetes)
• Age (25 and older for gestational diabetes)</td></tr>
<tr><td>• Presence of autoantibodies (antibodies that mistakenly attack body’s tissues or organs)</td><td>• Lack of physical activity
• Having high pressure
• Having low HDL (high-density lipoprotein) cholesterol (the “good” cholesterol) and high triglyceride level
• Smoking</td></tr>
<tr><td>• Physical stress (surgery or illness)</td><td rowspan="2">• Polycystic ovary syndrome
• Having a history of heart disease or stroke
• Having gestational diabetes or giving birth to a baby weighing >4 kg</td></tr>
<tr><td>• Exposure to illnesses caused by viruses</td></tr>
</table>

There are other genetic forms of diabetes with congenital or acquired origins including neonatal diabetes.[16] In neonatal diabetes, mutations in genes involved in insulin secretion have been identified and cause diabetes in new-born before 6 months. There are also uncommon forms of

immune-mediated diabetes including the autoimmune Stiff-man syndrome and patients with anti-insulin receptor antibodies.[17] Patients with Stiffman syndrome present stiffness of the axial muscles with painful spasms. These symptoms are additional to high glutamic acid decarboxylase (GAD) autoantibodies level, a characteristic shared with T1D. The presence of GAD autoantibodies expects to increase the diabetes risk. More than one-third of patients with Stiffman syndrome will develop diabetes. Patients with anti-insulin receptor antibodies are rare and uncommon form of diabetes. In these patients, the anti-insulin receptor antibodies may lead to the inability of insulin to bind insulin receptor in muscle, liver and adipose tissues. The impaired insulin action results in absolute insulin resistance and ultimately diabetes. Such extreme insulin resistance also termed type B insulin resistance is also found in patients with systemic lupus erythematosus.[18-20] Several genetic syndromes are accompanied by an increased incidence of diabetes. These include the chromosomal abnormalities of Down syndrome[21], Klinefelter syndrome[22], and Turner syndrome.[23]

Diabetes can be induced by drugs or chemicals.[24-25] Many drugs can impair insulin secretion or precipitate diabetes in individuals with insulin resistance. Certain vitamins, drugs and hormones such as the anti-parasite pentamidine, nicotinic acid vitamin and glucocorticoids can impair insulin action.[26] Some patients receiving γ-interferon develop diabetes associated with islet cell antibodies, sometimes leading to severe insulin deficiency.[27] Some endocrinopathies can lead to diabetes.[28] Excess amounts of growth hormones, cortisol, glucagon and epinephrine, leading to acromegaly, Cushing's syndrome, glucagonoma, pheochromocytoma, respectively, can cause diabetes. In general, hyperglycaemia occurs in individuals with pre-existing defects in insulin secretion, and hyperglycaemia typically resolves when the hormone excess is resolve.

1.3. Complications related to diabetes

Complications related to diabetics are classified as microvascular or macrovascular. Microvascular complications include nervous system damage (neuropathy), renal system damage (nephropathy) and eye damage (retinopathy). Macrovascular complications are cardiovascular disease, stroke, and peripheral vascular disease. Cardiovascular diseases cause up to 65% of mortality cases in diabetics.[29] In addition, these people are from 2 to 4 times more likely to develop strokes and heart disease compared to people without diabetes.[29] Excess of LDL (low density lipoprotein), also called "bad" cholesterol caused by diabetes may provoke atherosclerosis, generating fatty plaques in arteries.[30] More than 70% of people with T2D have high blood pressure, that can also give a rise in a risk to have kidney disease called nephropathy.[31] According to the American Diabetes Association (ADA) nephropathy develops

in about 20% to 30% of patients with type 1 or type 2 diabetes. Moreover, people having both T2D and nephropathy are at increased risk for developing many other diabetic complications, such as coronary heart disease and stroke.[32] Diabetic peripheral neuropathy (DPN) is a common complication estimated to affect 30% to 50% of individuals with diabetes.[33-36] Hyperglycaemia found to be the primary risk factor for developing of DPN. Other factors include hypertension, alcohol consumption, cigarette smoking as well as age and duration of the disease.[37-39] Diabetic retinopathy, which is the most common microvascular complication, is the leading cause of changes of retina and blindness among diabetic people. It has a relation to the duration of diabetes: almost all patients with T1D suffering from diabetes for 20 years and longer have retinopathy, while this number is about 60% for patients with T2D.[12, 40-42] The tactic for reducing the risks of complications related to diabetes must include improvements in glycemic control, blood pressure, and cholesterol level, since hyperglycemia, high blood pressure, and hypercholesterolemia are known to be the most significant risk factors.[43]

Since the life expectancy of people with diabetes can be shorten up to 15 years[44], it is also important to make life-style changes in order to control the disease. Increase of physical activity, healthy diet and reduce energy intake may also decrease a risk for T2D.[45] But in most cases to achieve a control, antidiabetic medication is required. To improve the comfort of drug intake, avoiding needle injections and to provide with on-demand delivery, alternative routes of administration should be implied.

1.4. Drug administration strategies for diabetes therapy

Together with the search of new antidiabetic drugs with the least side effects but with highest efficiency, different administration approaches are being relentlessly searched for (**Figure 1.3a**). Many of the antidiabetic drugs are small organic molecules, notably for T2D, while therapeutic peptides such as insulin and amylin are mostly considered for T1D (**Figure 1.3b**). For class II, drug formulations should promote the dissolution of the drug, with a minimum influence on the fat of the drug after administration. For class III drugs, the low bio-availability is addressed in formulations as increased bio-availability will decrease the large variability effect in different individuals. Furthermore, peptides such as insulin can be oxidized and denaturised in the acid environment of the gastrointestinal (GI) tract, losing its therapeutic activity. Next to the low pH, gastric enzymes are major barriers for antidiabetic drugs such as insulin when administered orally.[46-48]

Other routes have been considered in diabetes treatment such as nasal, pulmonary, buccal, and transdermal approaches (**Figure 1.3**).[49-61]

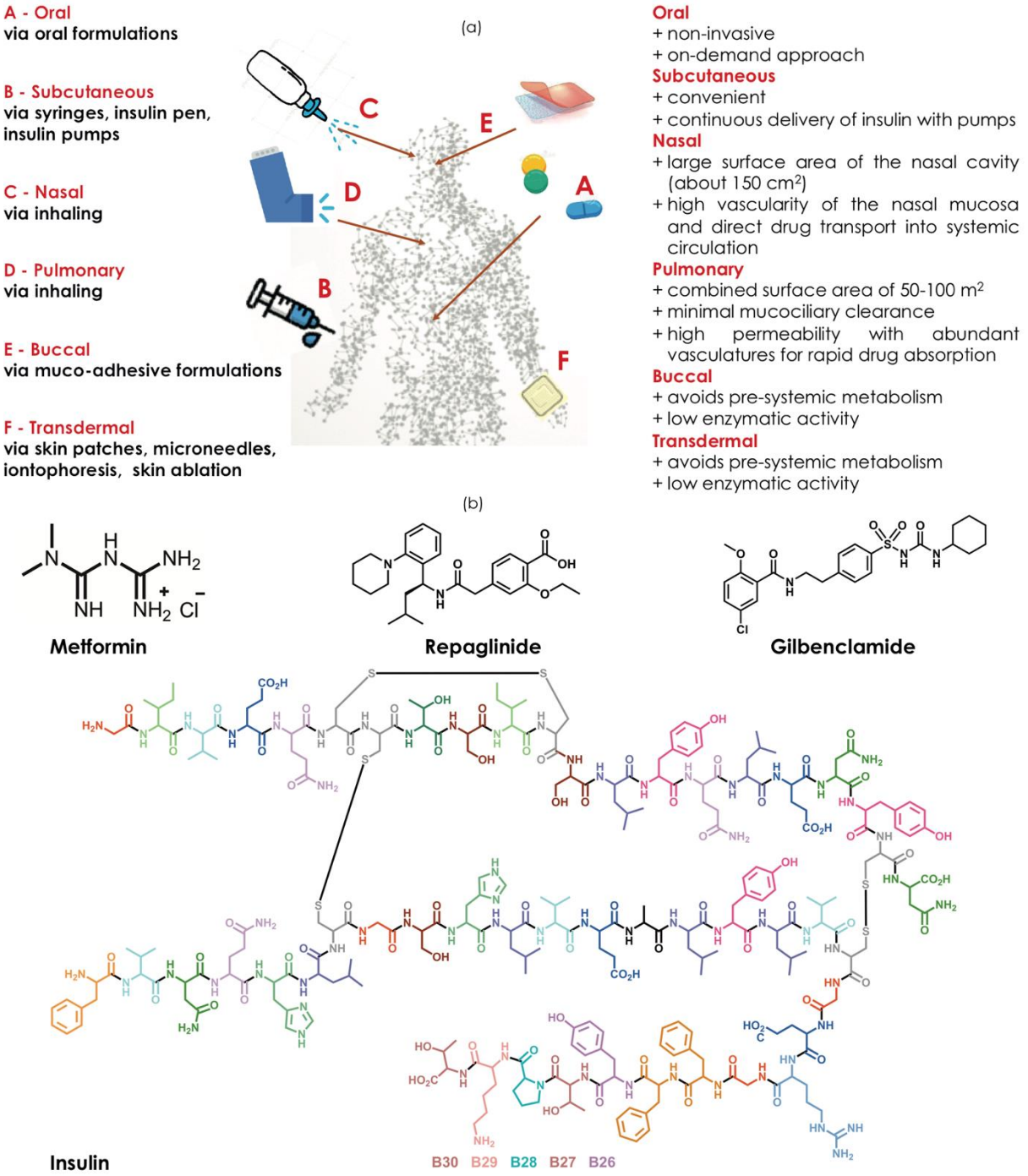

Figure 1.3. Antidiabetic drugs. (**a**) Current standard of care for type 1 and type 2 diabetes and their advantages. (**b**) Chemical structures of common antidiabetic drugs. Adapted from ref.[62]

1.4.1. Treatment of type 2 diabetes

Type 2 diabetes involves complex interactions of metabolic and genetic defects. Initially and often throughout their lifetime, patients with T2D do not need insulin treatment to survive. Dietary modifications and exercise accompanied by the supplementation of oral insulin sensitizers are the first line treatment for T2D.[63] The classes of medication approved for treatments of T2D include sulphonylureas[64-67], glinides[68-71], biguanides[72-75], α-glucosidase inhibitors[76-79], peroxisome proliferator-activated receptor agonists[80-86]. Metformin hydrochloride, belonging to biguanides, remains the most widely prescribed antidiabetic medicine for the treatment of T2D worldwide.[87] Metformin lowers BGLs without causing hypoglycaemia or stimulating insulin secretion. It also improves insulin action by reducing gluconeogenesis, glycogenolysis and lipids production. Metformin is particularly attractive as it is orally administrated and has several relevant medical advantages.[88-89] Beyond the antidiabetic effect, there is growing evidence pointing out the potential protective effects of metformin against neurodegeneration, fibrosis, cancer, and COVID-19.[90-92] However, there are still several concerns in the current use of metformin, in particular its relatively low bioavailability reaching 55%,[93-94] its short biological half-life of only 1 - 3 h,[95] and induced lactic acidosis.[96] Repeated applications of high doses (2.5 g daily dosage) may be required for an effective treatment, resulting in reduced patience compliance and occurrence of gastrointestinal (GI) syndromes such as diarrhea and nausea, weight loss up to anorexia, and taste disturbance. These concerns have led to the search of innovative formulations for improving bioavailability, decreasing the dosing frequency and GI side effects of metformin.[97].To overcome the side effects, improve bioavailability, and decrease the dosing frequency, several innovative formulations for metformin administration were proposed (**Table 1.2**).

Table 1.2. Innovative metformin-based formulations and routes of their administrations.

Formulation	*Route of administration*	*Activity and features*	*Ref.*
Porous silicon-based microparticles (μPSip)	Subsequence absorption	Due to tuned pore size and pH function, controlled metformin release over 26 h was achieved	98

Selenium nanoparticles (Se NPs)	Single low dose injection	Remarkable protective antidiabetic effects, illustrated by significant decreases in fasting blood glucose and insulin levels after 8 weeks treatment	99
Intercellular stimuli-sensitive chitosan-based metformin particles	Intracellular	Increased the anti-diabetes activity, improved insulin resistance in mice	100
Niosomal dispersions entrapped in alginate beads	Oral	Significant improvement of metformin hypoglycaemic effect	101
Poly(methylvinylether-co-maleic acid)based hydrogel microneedles	Transdermal	Delivery of metformin bypassing the GI tract	102
Hydroxypropyl methylcellulose-based fast dissolving film	Transmucosal	Rapid onset of action	103

Transdermal delivery, that will be discussed below in this thesis, is one of the promising approaches of metformin administration for treatment of T2D. Most of the studies are based on the development of metformin loaded hydrogel microneedles (**Figure 1.4a**). The team of Donnelly showed that a microneedles (MNs) patch made from an aqueous blend of poly(methylvinylether-co-maleic acid) crosslinked by esterification with polyethylene glycol (PEG) to which a metformin drug reservoir was attached, containing 75 mg metformin HCl, delivers 28.1 ± 2.3 mg in 24 h. *In vivo* studies allowed to detect metformin HCl in rat plasma at 1 h post microneedle application at a concentration of 0.6 ± 0.5 μg mL^{-1}, increasing to 3.7 ± 2.5 μg mL^{-1} at 3 h. (**Figure 1.4b**).

With the aim of improving patient's compliance and comfort avoiding skin penetration by needles, we will propose transdermal hydrogels formed by simple mixing of metformin with carboxylated reduced graphene oxide (rGO-COOH), in a volume ratio of 1:9 (v:v) . The release of metformin will be photothermally driven due to the presence of rGO-COOH.

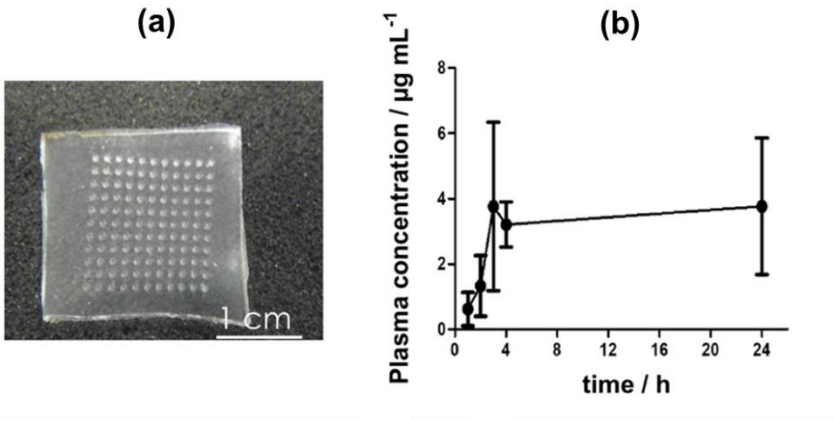

Figure 1.4. Transdermal delivery of metformin. (**a**) Digital image of hydrogel-based microneedle array in swollen state. (**b**) *In vivo* plasma profile of metformin following application of hydrogel MNs and solid metformin HCl at a dose of 100 mg. Reprinted with permission from ref.[102]

1.4.2. Treatment of type 1 diabetes

The T1D therapy is currently mainly based on two approaches: insulin replacement and islets or pancreas transplantation. Insulin, the most widely used and known therapeutic agent for T1D, is a peptide hormone produced by β-cells of the pancreas and acts as a gate conducting blood glucose into cells, providing them with the energy to function, remains. Insulin is one of the first proteins to be fully sequenced. Its structure represents 51 amino acids arranged in two chains, an A chain (21 amino acids) and B chain (30 amino acids) that are linked by two disulfide bonds (**Figure 1.3b**). Commercial production of human insulin in the early 1980s enabled production of synthetic human insulin in virtually unlimited quantities and in a cost-effective way.[104] To alter the pharmacokinetic properties of insulin, the B26–B30 region of the insulin molecule, not critical for insulin receptor recognition (**Figure 1.3b**) is generally substituted. Thus, the insulin analogs are still recognized by and bind to the insulin receptor. The types of insulin currently available on the market include rapid-acting insulin, short-acting insulin, intermediate-acting insulin, long-acting insulin, ultra-long acting insulin and insulin mixtures.

1.4.2.1. Insulin delivery modes

Insulin delivery via subcutaneous injection.

Subcutaneous injection is the most widespread mode of insulin administration into human body. Conventional syringes marked in insulin units (30, 50 or 100 IU) or pen-like devices as well as insulin containing cartridges allow to deliver insulin daily by multiple injections.[105] In general

an injection of slow-acting basal insulin in the morning or evening is required as well as frequent dosing of a rapid-acting insulin prior to meals. This invasive mode of administration is often associated with several concerns such as the needle phobia, injection pain, self-injection, lifestyle restriction, negative social stigma, poor self-efficacy, patient compliance, leading, sometimes, some patients to stop the treatment. Furthermore, the imperfect reproducibility of the insulin physiology, the risk of lipodystrophy (and potentially insulin resistance), the heat sensitivity of solutions that must be kept cool, make the need of alternative routes for insulin delivery essential.[106-108]

Insulin delivery via insulin pumps

Insulin pens constructed as a combination of disposable insulin cartridges and external continuous-insulin pumps found to be an alternative convenient method of insulin administration for diabetic patients intolerant to daily injections.[109] The principle of action of insulin pump is utilization of electromechanical pumps with superimposed meal-related boluses, providing a constant supply of rapid-acting insulin into the subcutaneous tissue at pre-selected rates. Insulin delivery by pumps is more efficient than multiple daily injections for stimulating blood glucose variability.

Insulin delivery via nasal cavity

Nasal antidiabetic drug delivery takes advantage of the large absorption surface area of the nasal cavity (about 150 cm^2) with high vascularity of the nasal mucosa and direct drug transport intosystemic circulation thus bypassing the GI tract associated low oral bioavailability (**Figure 1.4a**).[51-53] Nasal administration of fine insulin powder allows the partial delivery of insulin into the lungs, where it enters the blood through tiny blood vessels. Seeming the perfect administration route, several limitations impedes this approach to a certain extent. [54] One issue is the rapid (half-life of 0.25 - 0.5 h) clearance by the mucociliary mechanism, the primary innate defence mechanism of the lung, removing inhaled particles before they can reach the delicate tissue of the lungs. Only small amounts of insulin are therefore detected in the bloodstream after nasal administration.[61] Furthermore, permeation limitation across the mucus layer and nasal epithelium and enzymatic degradation similar to those of oral delivery impedes this approach. A variety of additives including alkylglycosides were tested to enhance the absorption of nasally applied insulin into the bloodstream,[59-60] and have shown to be relatively safe with stable insulin formulations in spray flasks,[58] making this mode of insulin administration appealing for patients who need consecutive daily insulin treatment.

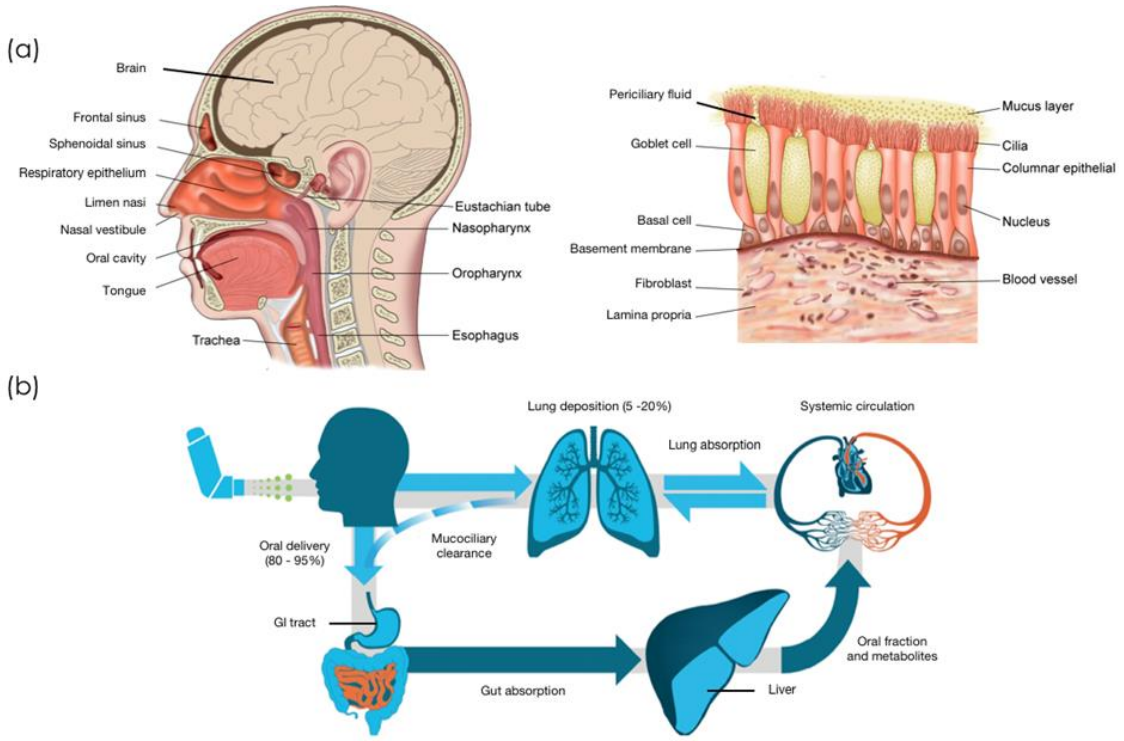

Figure 1.4. (**a**) Nasal drug administration (adapted from ref.[52]). (**b**) Pulmonary delivery where, in general, >20% of the drug is deposited in the lung, with the rest being swallowed orally. Deposited compounds in the lung are also cleared by mucociliary clearance and systemic absorption through lungs. Adapted from ref.[50-51]

An interesting aspect of insulin, not related to regulating BGLs directly, is that in the brain, insulin acts as a growth factor, regulates energy homeostasis, and is involved in learning and memory acquisition. Pre-clinical studies have shown that nasal insulin is neuroprotective for Alzheimer's disease, Parkinson's disease, and traumatic brain injury. Indeed, insulin can be detected in the central nervous system within minutes following nasal administration.[57]

Nasal insulin delivery has been proposed as an alternative to subcutaneous injection, as it is easier and less painful way of insulin administration. The first inhaled powder form of recombinant human insulin approved by FDA appeared on the Europe and USA markets in 2006 [110]. To overcome the limitations like low delivery payload, poor reproducibility, mucosal irritation, some insulin containing formulations that at warm physiological temperature within the nasal cavity convert to a gel have been proposed.[111] But due to low bioavailability, only small amounts of insulin are detected in the bloodstream after nasal administration of up to 160 IU.[61] Until now, a variety of additives including alkylglycoside are tested to enhance the absorption of nasally applied insulin into the bloodstream to facilitate glucose lowering effects for the treatment of diabetes,[59-60] but nothing remains conclusive.

Insulin delivery via lungs

Human lungs (**Figure 1.4**) with a combined surface area of 50 - 100 m^2, 1000-fold larger than that of the nasal cavity and several times larger compared to the 2 m^2 of skin. Both lungs contain about 274-790 million alveoli involved in gas and liquid exchange and transport of liquids delivered from alveoli to the blood.[56] Different to the columnar epithelium of the GI tract and the nose, its alveolar epithelium has a thickness of 0.1 - 0.2 μm with minimal mucociliary clearance and presents high permeability as well as abundant vasculatures, allowing rapid drug absorption. This makes alveoli and the associated vascular network a sought-after method of delivering antidiabetic drugs to the systemic circulation. However, while corticosteroids and other drugs might be delivered effectively, hydrophilic macromolecules such as insulin have limited permeation through the mucus layer (1 - 10 μm thickness) that covers the pulmonary epithelium. Moreover, 90% of inhaled insulin is lost in its passage to alveoli to enter the blood stream. The other barriers to overcome for insulin absorption includes pulmonary enzymes and macrophages. Most proteins on the alveoli are subjected to degradation by proteases or clearance by macrophages, which also secret short-lived peroxidases, mediators, able to degrade the therapeutic protein.

While some drugs like corticosteroids and others were found to be good candidates for effective pulmonary administration, hydrophilic macromolecules such as insulin have limited permeation through the 1 - 10 μm thick mucus layer that covers the pulmonary epithelium. A major part of insulin (90%) sticks to the air passages before reaching the lung alveoli to be absorbed to the systemic circulation to reduce the blood sugar. In addition, most proteins are subjected to degradation by proteases or clearance by macrophages in the alveoli of the lung, which also secret short-lived peroxidases, and inflammatory mediators able to degrade the therapeutic protein. The problem that needs to be resolved is how to deliver insulin into the alveoli directly without being deposited on the air passages on its way to the alveoli. So far, no such a way has been found, and it may be an unreachable target especially due to the presence of billions of tentacles (cilia) on the surface of the cells lining the air passages that pick up any particulate matter from the breathed air that passes by. Some of the FDA approved inhalation systems like Exubera[112] and Afrezza[113] presented on market in 2006 and 2015 were withdrawn based on side effects, such as the notable increased risk of hypoglycaemia for people smoking and for patients with unstable or poorly controlled lung disease such as asthma or chronic obstructive pulmonary disease. In addition, there was a high risk of carcinogenic effects from inhaled insulin. This makes research in this domain extremely challenging.

Other two approaches consist of insulin delivery vial oral cavity and transdermal delivery. These approaches will be investigated in more details from a material science aspect in this thesis.

Insulin delivery via oral cavity

Indeed, the literature on orally administered insulin formulations is most widely presented among other delivery routes. Oral administration of insulin is largely preferred to other routes due to the convenience and good patient compliance. However, the oral delivery of insulin remains a challenge due to the hydrophilic nature of insulin and its limited ability to across the lipid bilayer of biological membranes. The formulations for oral insulin administration are mostly presented as sprays and gels containing insulin-loaded nanoparticles[114-134]

Within the oral cavity, there are three other categories for drug delivery being sublingual (through mucosal membranes lining the floor of the mouth), buccal (through the mucosal membranes lining the cheeks) and local (into the oral cavity). When selecting one over the another, one has to consider their differences in anatomy and permeability. The structure of oral mucosa incudes oral epithelium, basement membrane, lamina propria and submucosa (**Figure 1.6a**). The thickness of oral mucosa differs depending on the region: from 100-200 μm for the floor of the mouth, the ventral tongue, and the gingivae to 500-800 μm for the buccal mucosa. [135] The sublingual mucosa is accessible and convenient, with relatively good permeability for majority of drugs..

One of the attractive methods for mucoadhesive patch preparation is electrospinning. This low-cost, simple and versatile technique is based on the production of ultrafine nanofibres by charging and ejecting a polymer melt or solution through a spinneret under a high-voltage electric field and to solidify or coagulate it to form a filament. (**Figure 1.5a**). Drug loaded nanofibers provide with large surface-to-volume ratio and high porosity allowing immediate drug release.[136] The choice of polymer for the electrospinning of trasmucosal patch depends on polymer's adhesive force. Poly(acrylic acid) (PAA) and poly(vinylic alcohol) (PVA) with the mucoadhesive force of 185% and 94.8% respectively are ideal candidates for this purpose.[137] To this end, Sharma et al. proposed bio-degradable poly(vinyl alcohol)-based nanofiber mats loaded with insulin. (**Figure 1.5b**). *In vivo* studies, when applying 2.5 IU insulin loaded into PVA-based patch on the sublingual lining in rats (**Figure 1.5c, green line**), showed decline in the blood glucose concentration and the effect lasted for an average period of 10 hours.

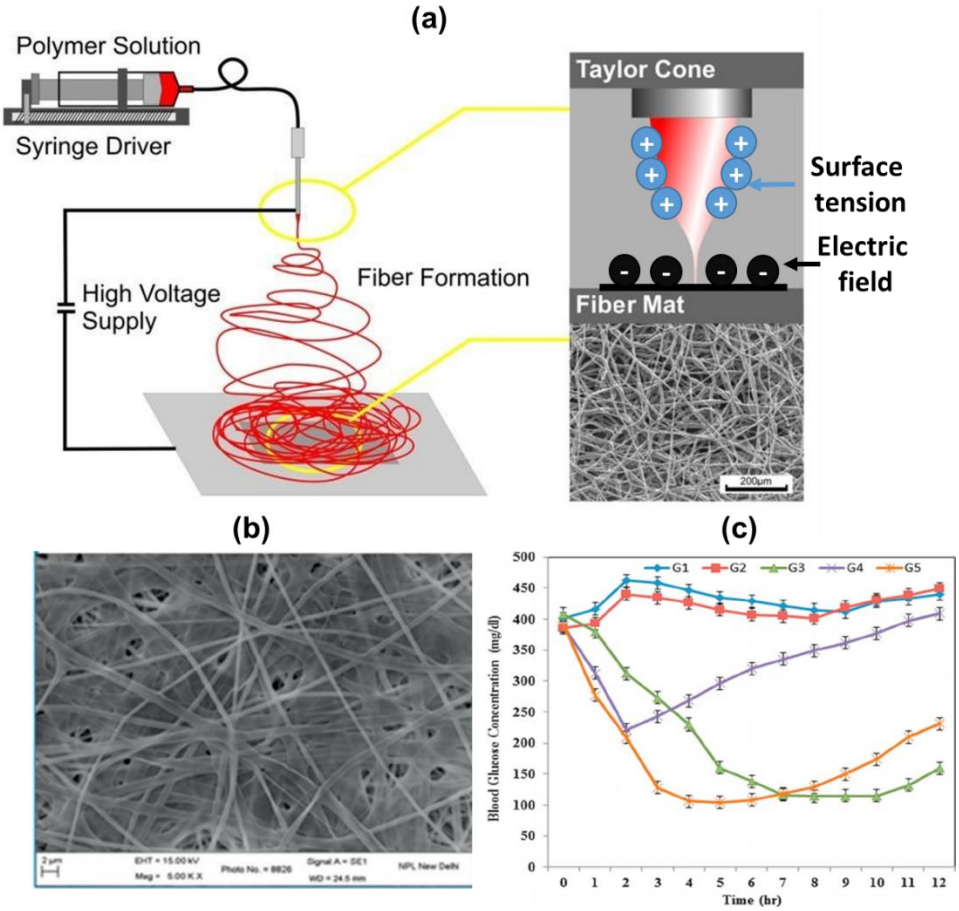

Figure 1.5. (**a**) Schematic representation of electrospinning process. (**b**) SEM image of PVA-based electrospun nanofibers. (**c**) Blood glucose concentration curves of *in vivo* studies in rats. Adapted from ref .[138-139]

Due to rich blood supply, the sublingual mucosa is able to produce a rapid onset of action that makes it applicable for drugs with short delivery period and infrequent dosing requirements. From this point of view, buccal mucosa is more suitable for systematic transmucosal drug administration, like insulin, as it is less permeable with slower onset of action. Moreover, smooth muscle and relatively immobility of mucosa make it preferred over other sites for retentive systems used for drug delivery. Although compared to buccal mucosa, the sublingual mucosa is better permeable it is not appropriate for an oral transmucosal delivery systems, because this region lacks an expanse of smooth muscle or immobile mucosa. In addition, constant saliva washing interferes with the substances placed for drug delivery. [140-141]

Buccal mucosa has appeared as another promising delivery site for antidiabetic drugs such as insulin.[55] It offers a series of advantages as it avoids pre-systemic metabolism of insulin via low enzymatic activity and ease of accessibility of buccal absorption site. Buccal insulin delivery is attracting increased attention as it is painless and holds on-demand features[142-143].

The buccal mucosa is well-vascularized, allowing drugs to be rapidly absorbed into the venous system underneath the oral mucosa (**Figure 1.6a**). Moreover, this system circumvents first-pass hepatic metabolism by directing absorption via venous system that reaches the heart directly through internal jugular vein. Indeed, it is distinct from oral administration. In addition, due to lower concentration of enzymes, buccal route is more attractive in terms of protein delivery. Mucoadhesive buccal drug delivery is expected to improve drug bioavailability, to increase the patients' s therapy compliance, to sustain drug delivery and to increase the onset of action with the possibility to remove the formulation if therapy is required to be discontinued.[144-145] But it is also necessary to take into account the inconvenience of buccal route drug administration such as the barrier properties of mucosa, smaller total area available for drug absorption, salivary scavenging, risk of swallowing delivery device, washing away of drug and continuous dilution of dissolved drug by saliva.[146]

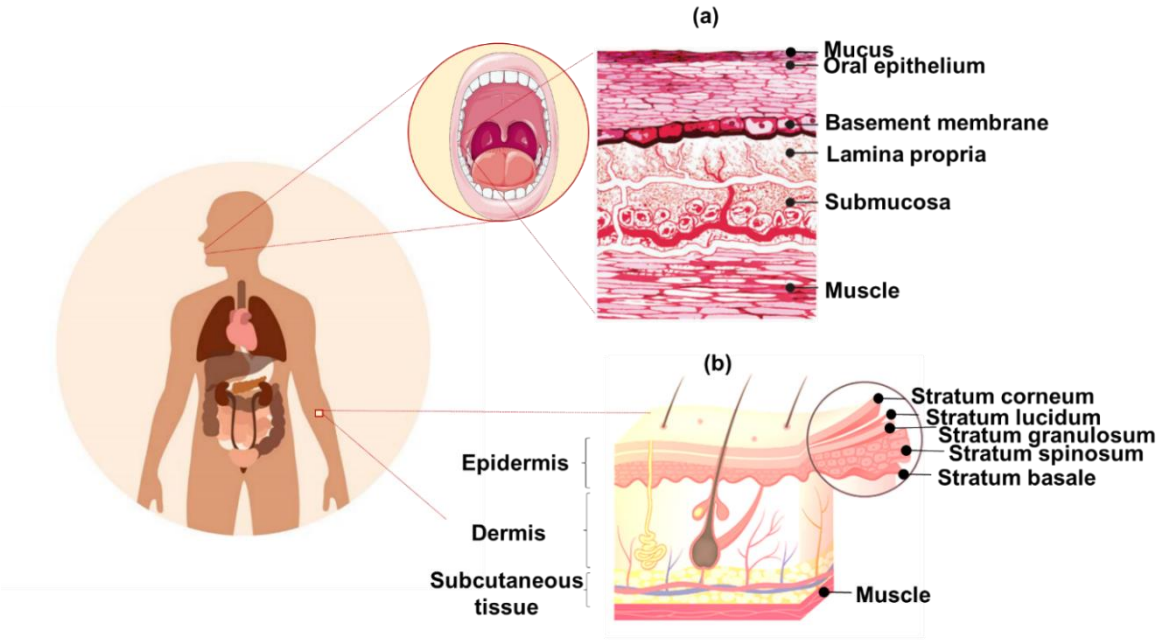

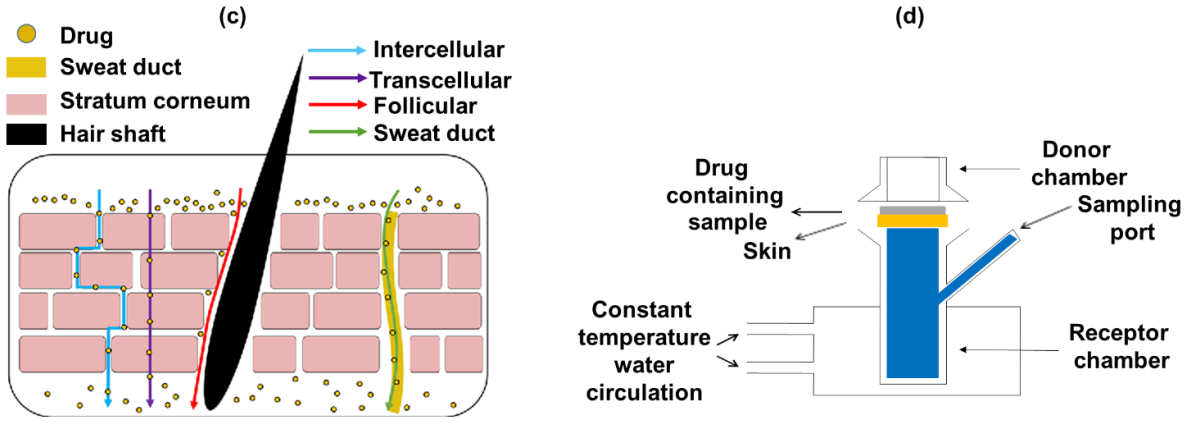

Figure 1.6. (**a**) Buccal delivery route and structure of buccal mucosa. (**b**) Transdermal delivery route and skin structure. (**c**) Different possible routes for the penetration of small drugs passively through the skin. (Adapted from ref.[147-148]) (**d**) Schematic representation of Franz diffusion cell used in transdermal delivery approach.

In this thesis we will investigate a buccal delivery of insulin from the mucoadhesive poly(vinylic alcohol)-based nanofiber mats produced by electrospinning. Unlike those described above, they will be cross-linked with a cross-linking agent such as β-cyclodextrin in order to attain insolubility in water. This step will allow to make nanofibers reusable for loading and release of insulin.

Transdermal delivery of insulin

The other approach developed in the thesis is transdermal delivery. Currently, delivery of drugs through the skin, known under the term transdermal delivery (TDD), has attracted much interest from the scientific community as well as from pharmaceutical companies.

Skin – the largest organ of human body – is composed of three histological layers, which are the epidermis, dermis and hypodermis (subcutaneous tissues) (**Figure 1.6b**). For successful passive skin permeation, drug should enter into the stratum corneum (SC) and then penetrate across it. The stratum corneum is the outermost layer of the skin with a thickness about 10-20 μm, and attracts special attention for TDD as it is this layer with limits the passive diffusion of most drugs. It consists of corneocytes and lipids forming brick and mortar structures. The routes of drug penetration via the SC can be classified as transcellular, intracellular, follicular and through sweat glands in the skin (**Figure 1.6c**). Only drugs with lipid-soluble properties can overcome the SC barrier properties. Compounds with small molecular weight have found to penetrate the SC via the intercellular route. In this delivery approach drugs pass through the

corneocytes that contain highly hydrated keratin provide an aqueous environment from which hydrophilic drugs can pass.[149] Indeed, the drugs that can be delivered passively via the skin have to meet a number of requirements such as high lipophilicity, nontoxicity, small molecular weight (usually <500 Da), melting point < 250 °C, aqueous solubility, octanol/water partition coefficient ≈ 1-5. **Figure 1.6d** depicts a classical Franz diffusion cell used for permeation experiments in transdermal administration approach. It consists of donor chamber, where the compound of interest is places, membrane or skin sample for drug diffusion and receptor chamber. It is usually filled with liquid, where the drug is soluble and a part of it is withdrawn through sampling ports at definite time intervals. In order to maintain the sink conditions[150], the amount of liquid withdrawn is replace by the receptor chamber's solution.

Considering that, some enhancement methods were proposed in order to expand the list of compounds for successful transdermal administration. One of the way is utilization of chemical compounds, e.g. alcohols, surfactants, sulfoxides, that act as penetration enhancers. Despite their important function in increasing the passive diffusion of the drugs, chemical enhancements usually irritate the skin and disrupt the ordered SC lipid bilayers or corneocytes structure organization. Therefore, lots of efforts were put into the development of other approaches, one of them being the use of nanocarriers.[151] The size of nanocarriers was found to be most crucial for TDD, as particles with small diameter can more easily penetrate the skin. Another approach is based on the use of physical enhanced strategies (**Figure 1.7**).

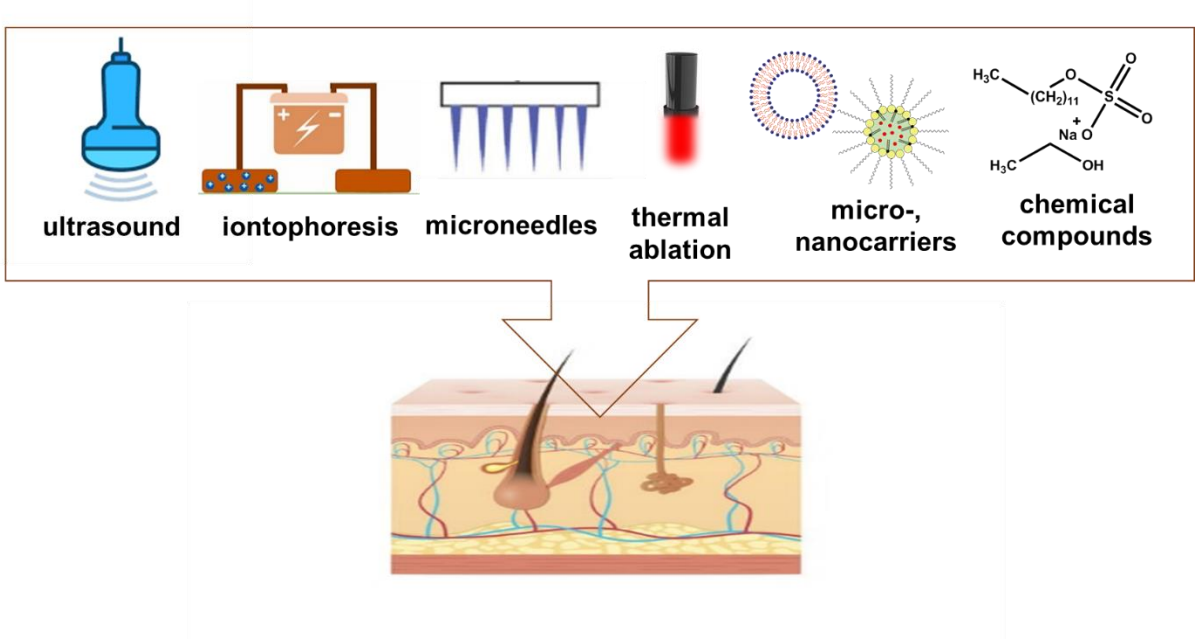

Figure 1.7. Enhancementsfor transdermal delivery (inspired by ref. [147])

Sonophoresis, based on ultrasound at low frequencies, enhances the flux of large molecular weight substances through the skin. [152] Higher voltage pulses are involved in electroporation used for the creation of pores in the skin with the possibility to deliver therapeutics with high molecular weight[153]. Iontophoresis is a technique where small electrical currents (from 0.5 to 20 mA) applied to anode and cathode to increase permeation of ionisable drugs into the skin. [154-156] Microneedles (MNs) array, consisting of a plurality of micro-sized tips ranging in length from 25 - 2000 μm offer a highly promising solution for overcoming the barrier that the skin creates to deliver small molecular as well as macromolecular therapeutics such as proteins peptides and vaccines. They also can be classified as solid[157-158], hollow[159], coated[160], dissolving[161-162] and hydrogel-forming[163-164]. Solid MNs are applied to the skin in order to create microconduits. After removal of MNs, drug loaded patch deposited onto the microcondiuits allows the passive diffusion of drugs. Solid microneedles are generally made of silicon, metal, ceramic and polymers. [165-167] Hollow MNs are usually fabricated from similar materials as solid MNs, but their design is different. In hollow MNs the interior part of needles is loaded with the drug solution or dispersion that is delivered to the skin after its piercing with MNs. In coated MNs the tips are covered with the drug solution. Their structure is based on metals or polymers and this type of MNs has been used for delivery of macromolecules such as insulin.[168]. For the preparation of dissolving microneedles the desired drug is mixed with biocompatible and soluble polymers such as poly(vinyl)alcohol, pullulan, hyaluronic acid[161, 169-170] etc. In contact with skin, the polymer needles dissolve with gradual drug release. It was shown that dissolving MNs can successfully deliver insulin.[171] For hydrogel forming MNs, blank microneedles made of polymers are combined with drug loaded reservoir. The technology is based on the swelling of needles after their insertion into the tissue following the drug diffusion from the reservoir into the skin.[172-175]

Another promising approach allowing to enhance drug delivery through the skin is based on its thermal ablation. The generation of local heat leads to the generation of transient microchannels of typically 50–100 μm in diameter, which enables the transdermal delivery of a wide range of drugs including macromolecules.[176-177] Multiple lasers have been tested for laser assisted drug permeation, but only few of them cause minimal damage of the skin and can be applied for transdermal drug delivery (**Figure 1.8a**). CO_2 based laser emits a wavelength of 10600 nm and causes tissue vaporization due to heating of water, which in turn yields in thermal necrosis of the tissue. Erbium-doped yttrium aluminum garnet (Er:YAG) laser light at 2940 nm is efficiently absorbs by water molecules. Due to its reduced thermal injury (comparing with CO_2

laser) it is used in cosmetology for instance for the scars treatment. Alexandrite and Ruby lasers, unlike CO_2 and Er:YAG, do not achieve the removal of the SC, which means they cannot be used for TDD. The lasers with emission wavelength in near-infrared (NIR) region would be highly favorable for TDD, as light of these lasers penetrate deep into the tissue with minimal absorption by the skin. Indeed, skin is considered transparent in this wavelength region. To achieve the required heat transfer, the interest of the use of photothermal agents such as reduced graphene oxide has been shown. Reduced graphene oxide (rGO) is a 2D carbon-based material consisted of carbon atoms with sp^2 hybridization. It is produced by chemical, thermal and UV treatment of graphene and graphene oxide with reducing agents[178] (**Figure 1.8b**). The interest of using rGO as an enhancer for transdermal delivery is caused by its ability to rapidly convert a low power NIR laser irradiation into heat. [179] In addition, due hydrogen bonding, electrostatic and π-π interactions between the aromatic rings of rGO and most of organic drug molecules, the last ones can be loaded onto the surface of rGO with the combination of phototherapy. It has been shown that combination of reduced graphene oxide and poly(ethylene glycol) dimethacrylate can form hydrogels under UV light. Afterwards loaded with insulin, they showed ability to deliver insulin through porcine skin in controlled manner under NIR irradiation.[180]

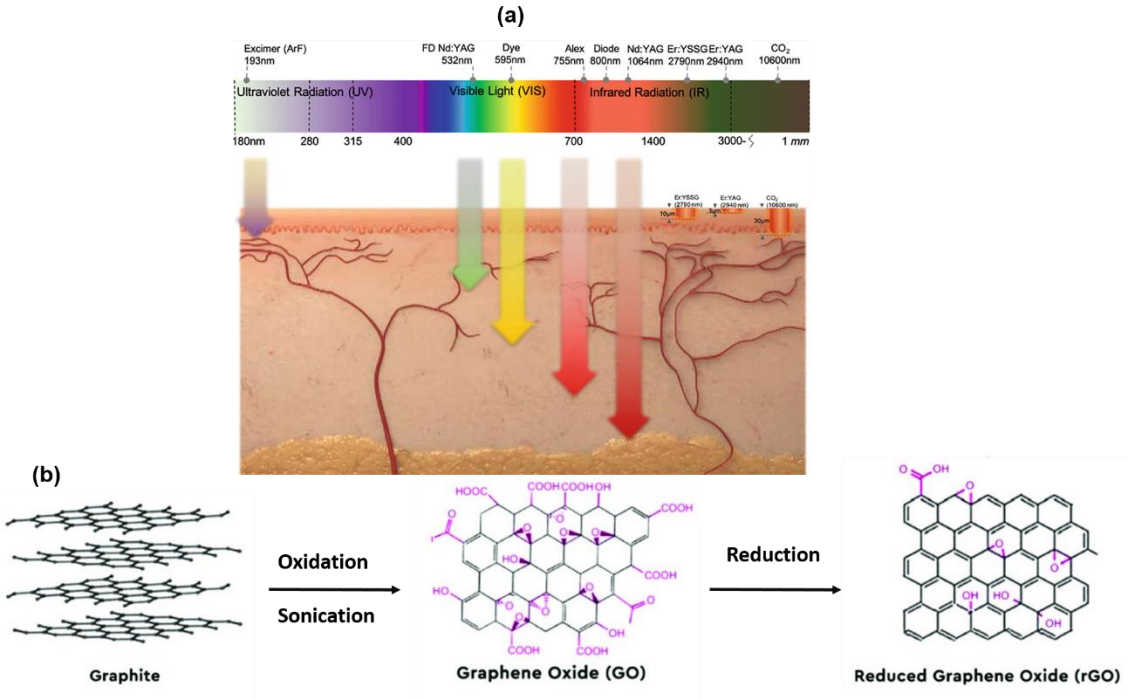

Figure 1.8. (a) Presentation of skin tissue and penetration depth of different laser and their emission wavelength. Reprinted from ref.[181] (**b**) Schematic presentation of rGO synthesis using graphite and GO as precursors (adapted from ref. [182])

1.5. From drug administration to treatment of β-cells via islet amyloid disaggregation

Next to the development of drug delivery approaches for diabetic patients, a growing body of evidence suggests that β-cell failure in T2D, relies on the formation of pancreatic islet amyloid deposits, indicating that islet amyloid may have an important role in β-cell loss in this disease. The major component of islet amyloid is the islet amyloid polypeptide (IAPP) amylin, co-secreted with insulin from β-cells. In T2D, this peptide aggregates to form highly insoluble amyloid fibrils in the pancreatic islets of Langerhans that are toxic to β-cells. While the mechanism responsible for islet amyloid formation in T2D is still unclear,[183] the search for inhibitors of islet amyloid fibril formation might prevent the progression to β-cell failure in T2D and should therefore be considered as a therapeutic approach to treat this disease. IAPP, like insulin, plays an important role lowering the level of glucose by inhibiting glucagon secretion. Human amylin, co-secreted by pancreatic β-cells along with insulin, is composed of 37 amino acids and the fibrillation process of this native peptide results in the formation of cytotoxic fibrils with a diameter of approximately 5 to 15 nm, leading to β-cell death and disease **(Figure 1.9a)**.[184] Together with low pH, high insulin-to-hIAPP ratio and Zn concentration, amylin stays inside β-cells granules at mM concentration range without formation of amyloid aggregations.[185] While after secretion, the physiological environment changes may cause the formation of toxic aggregates, leading to β-cells death **(Figure 1.9b)**. The cytotoxicity of amyloidogenic protein aggregates may be due to interaction with the lipid membranes, oxidative or endoplasmic reticulum stress and mitochondrial signaling pathway dysfunctions.[186]

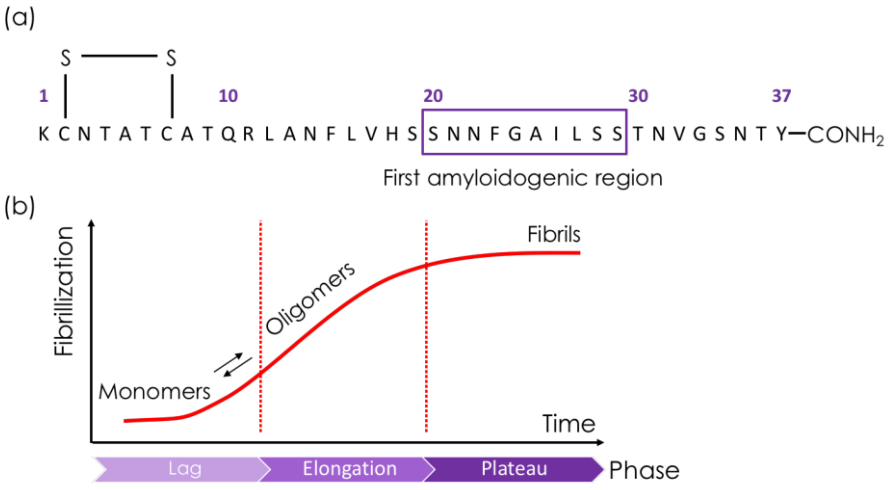

Figure 1.9. Islet amyloid aggregation. (**a**) Human amylin sequence. Redraw from ref. [183] (**b**) Distinct stages of fibrillation process. Reproduced with permission from ref. [184]

The role and precise way of IAPP contribution into development of diabetes is still has to be established. It is suggested that under prediabetic conditions, there is an onset of impaired glucose tolerance, high fasting glucose levels, and insulin resistance. Because of that, β-cells are stressed and induce more production of insulin. Since insulin and IAPP are co-processed and co-secreted, increased insulin production also results in enhanced IAPP levels. Enhanced IAPP/insulin levels in turn take part in the formation of critical nuclei responsible for the fibrillation of the hormone into amyloid. The amyloid aggregation processes results in injury and death of β-cells, that synthesize both insulin and IAPP, thereby progressing the development of T2D (**Figure 1.10**)[187]

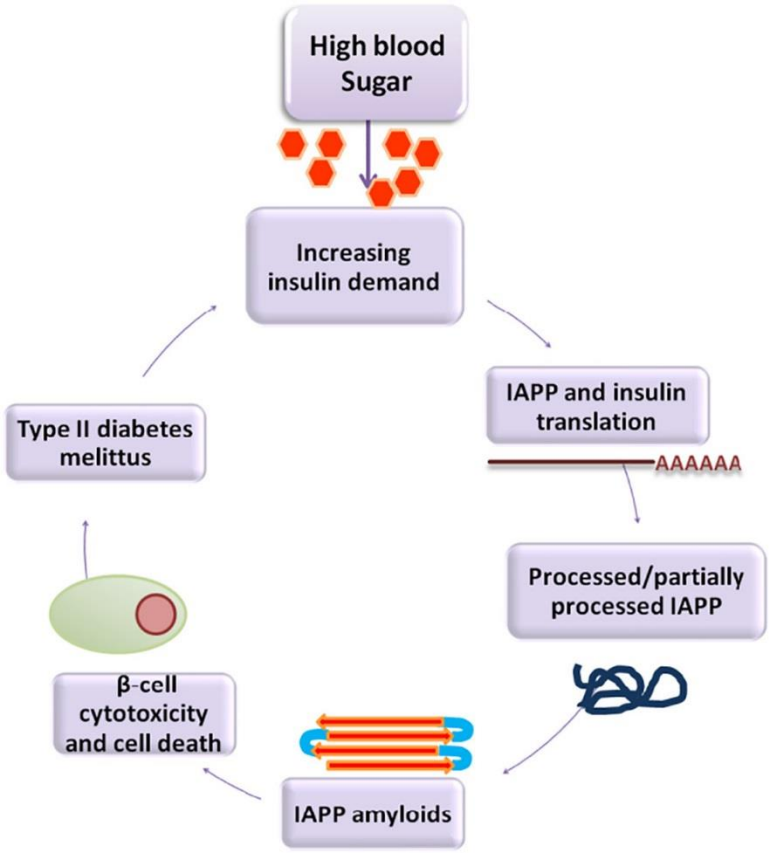

Figure 1.10. Mechanism of IAPP aggregation cascade proposed by ref.[187]

As the fibrillation process found to be harmful for β-cells, a number of efforts was made to find an agent for its efficient inhibition. Some materials as small molecules, metal complexes, gold nanoparticles, magnetic nanoparticles have been screened in order to reduce the cytotoxic effect of formed aggregates.[188-189] Among the others, graphene quantum dots (GQDs) and carbon quantum dots (CQDs) have drawn extensive attention due to their unique structure and

properties such as low toxicity, good biocompatibility, zero-dimension and fluorescence acivity.[190-191] Recently, Koppel et al.[192] examined the catalytic effects of LPS (lipopolysaccharide) on the formation of IAPP fibrils with their mitigation with zero-dimensional carbon quantum dots (CQDs) (**Figure 1.11**). To form fibrils, 25 μM IAPP were incubated with LPS (0.78 μg/mL) at 37°C for 8h. The ThT assay demonstrated an enhancement in fluorescence intensity for co-incubated solution of IAPP and LPS compared to IAPP solution, which indicates that LPS promotes fibrillation of IAPP. When co-incubated with CQDs, fluorescence intensity falls significantly for both IAPP and IAPP/LPS solutions, suggesting the disintegration effect presented in CQDs. (**Figure 1.11.I**). The formation and disintegration of formed aggregates was also confirmed by TEM imaging (**Figure 1.11.II**).

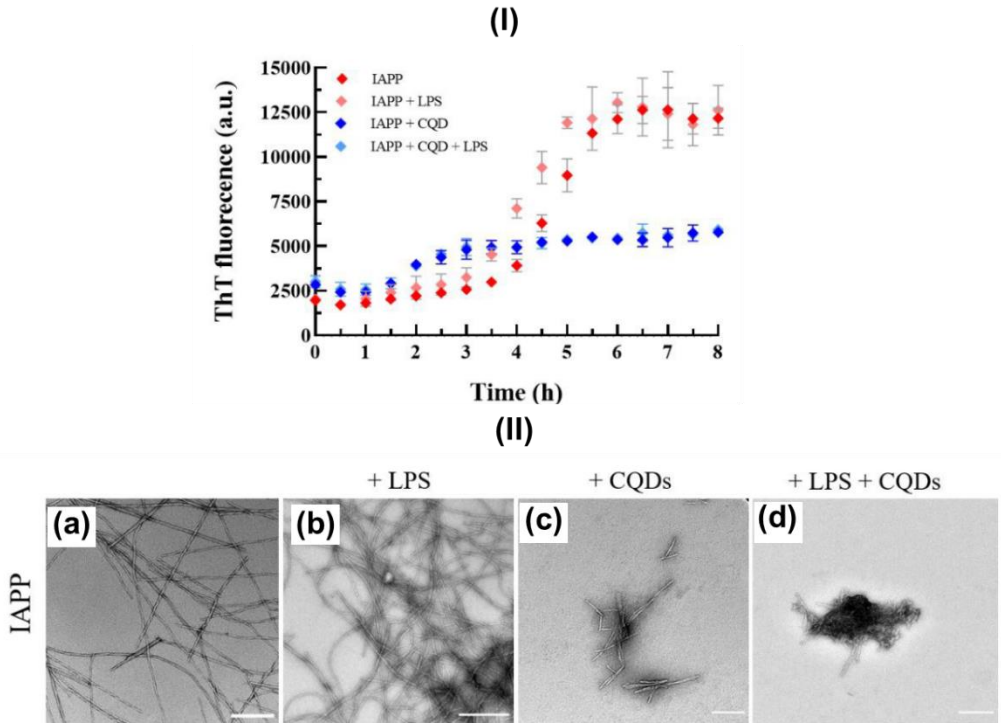

Figure 1.11. (**I**) Aggregation kinetics and morphologies of IAPP in the presence of LPS and CQDs. (**II**) TEM imaging: (**a**) IAPP fibrils alone, (**b**) IAPP/LPS fibrils, (**c**) IAPP fibrillation in the presence of CQDs, (**d**) IAPP/LPS fibrillation in the presence of CQDs. Reprinted from ref.[192]

Since the inhibition effect of CQDs on IAPP when co-incubated together was investigated, we will be mainly focused on the ability of CQDs to disintegrated already formed fibrils. For this purpose, IAPP will be fibrillated via incubation at 37°C and CQDs will be further added. The process will be monitored by ThT assay and AFM imaging.

CHAPTER 2:

Mucoadhesive electrospun patches for buccal delivery of insulin

2.1. Introduction

Electrospinning of fiber mats incorporating therapeutic agents have become widely explored for the development of fast-dissolving drug delivery systems.[193-197] In contrast to other forms of drug carriers, such as liposomes and nanoparticles, electrospinning technology provides great flexibility in the therapeutic to be loaded into the fiber matrix and the material itself.[198] Being different from transdermal drug delivery route, mucosal surfaces are lacking the stratum corneum barrier, resulting in faster drug delivery. The inherent barriers for efficient buccal mucosal drug delivery are the keratinized tissue and the elimination of the drugs to the flashing action of saliva in the absence of uni-directional mucoadhesive mouth patches.[199]

While electrospun drug reservoirs have high drug entrapment efficiency, the delivery of the drug is guided by drug diffusion out of the matrix, as well as by the degradation/dissolution of the carrier polymer. A different concept is the controlled release of active principles at a certain time point, putting the patient into the centre of action. Antinbasak et al. [200] have demonstrated lately the utilization of reduced graphene oxide (rGO) loaded poly(acrylic acid) (PAA) based hydrophilic nanofiber matrix for photothermal release of antibiotics. PAA was electrospun in the presence of beta-cyclodextrin (20 wt.% of PAA) as a cross-linker. The formed PAA@rGO matrix features good photothermal heating properties reaching 51±2 °C upon laser (980 nm) irradiation at a power density of 1 W cm^{-1}.

We investigated the usefulness of such PAA@rGO matrixes as mucoadhesive films for buccal and cornea linings as well as for the on-demand delivery of insulin via photothermal activaiton (**Figure 2.1**). We speculated that the presence of ionizable groups such as carboxyl groups of PAA and rGO together with hydroxyl groups of the cyclodextrin cross-linker ensures the interaction with the mucosal membranes. Indeed, as will be shown in the following mucoadhesive studies confirmed excellent muco-adhesion and could be imployed for *in vitro* insulin release studies and *ex vivo* permeation studies using pig cheek lining and pig eyes.

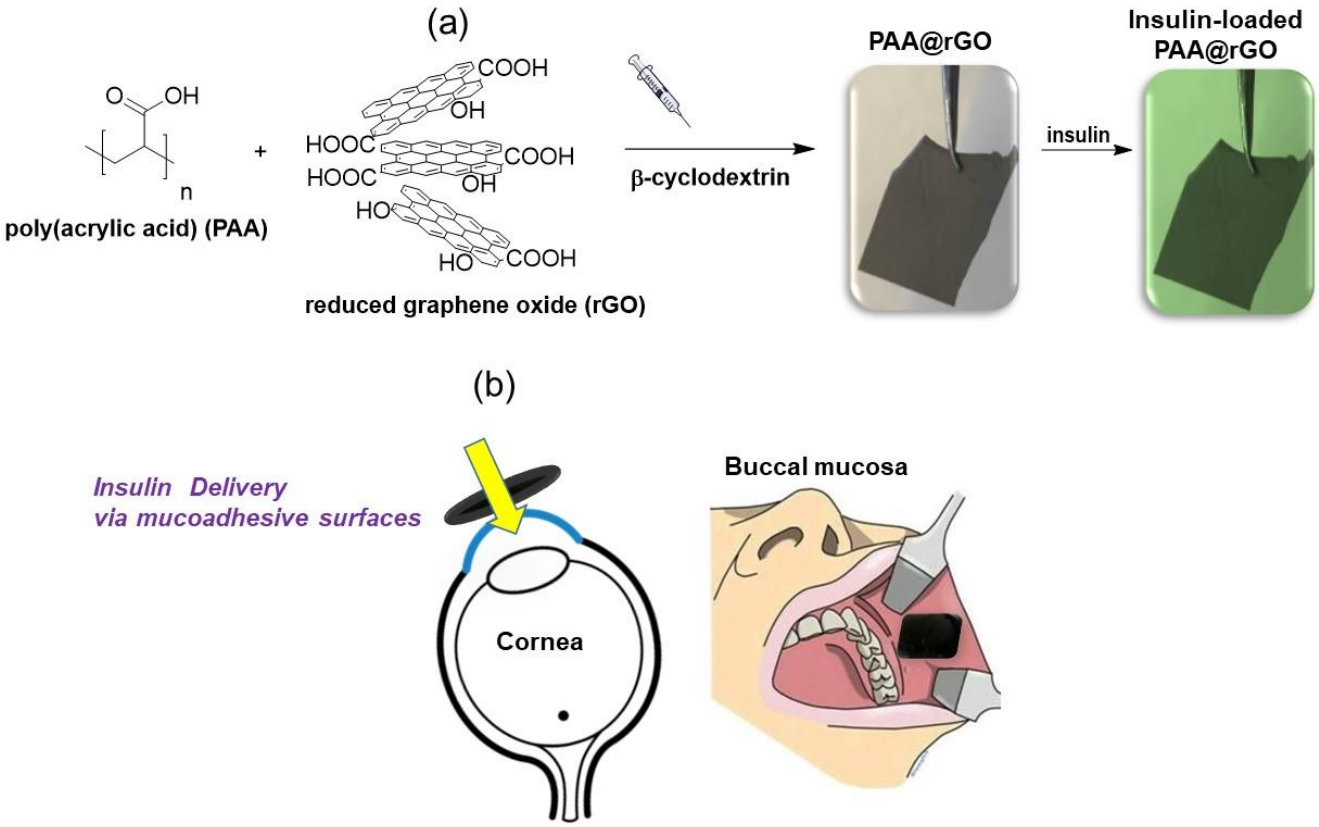

Figure 2.1. (**a**) Illustration of the formation of β-cyclodextrin cross-linked PAA@rGO nanofiber mats using electrospinning method. (**b**) Heat triggered on-demand insulin release via mucoadhesive interfaces such as cornea and buccal mucosa.

2.2. Fabrication and characteristics of mucoadhesive PAA@rGO fiber mats

Buccal and cornea mucoadhesive patches were fabricated by electrospinning a mixture of PAA, β-cyclodextrin (20 wt.% of PAA) and rGO (2.4 wt.%). The patches consist of a dense fiber mat (**Figure 2.2a**) with fibers of 400±150 nm in diameter. Most importantly, PAA@rGO were water-insoluble and the fibrous nanostructures remained preserved even upon immersion for 1 week in water at 37°C (**Figure 2.2b**). This contrasts with rGO-free PAA fibers which dissolve immediate after immersion in water. The PAA@rGO films proved to be also stable upon immersion into saliva (**Figure 2.2c**). This makes it different to others works in which the nanofiber film disintegration was initiated upon contact with stimulated salivary fluid in a time frame of about 150 s.[201]

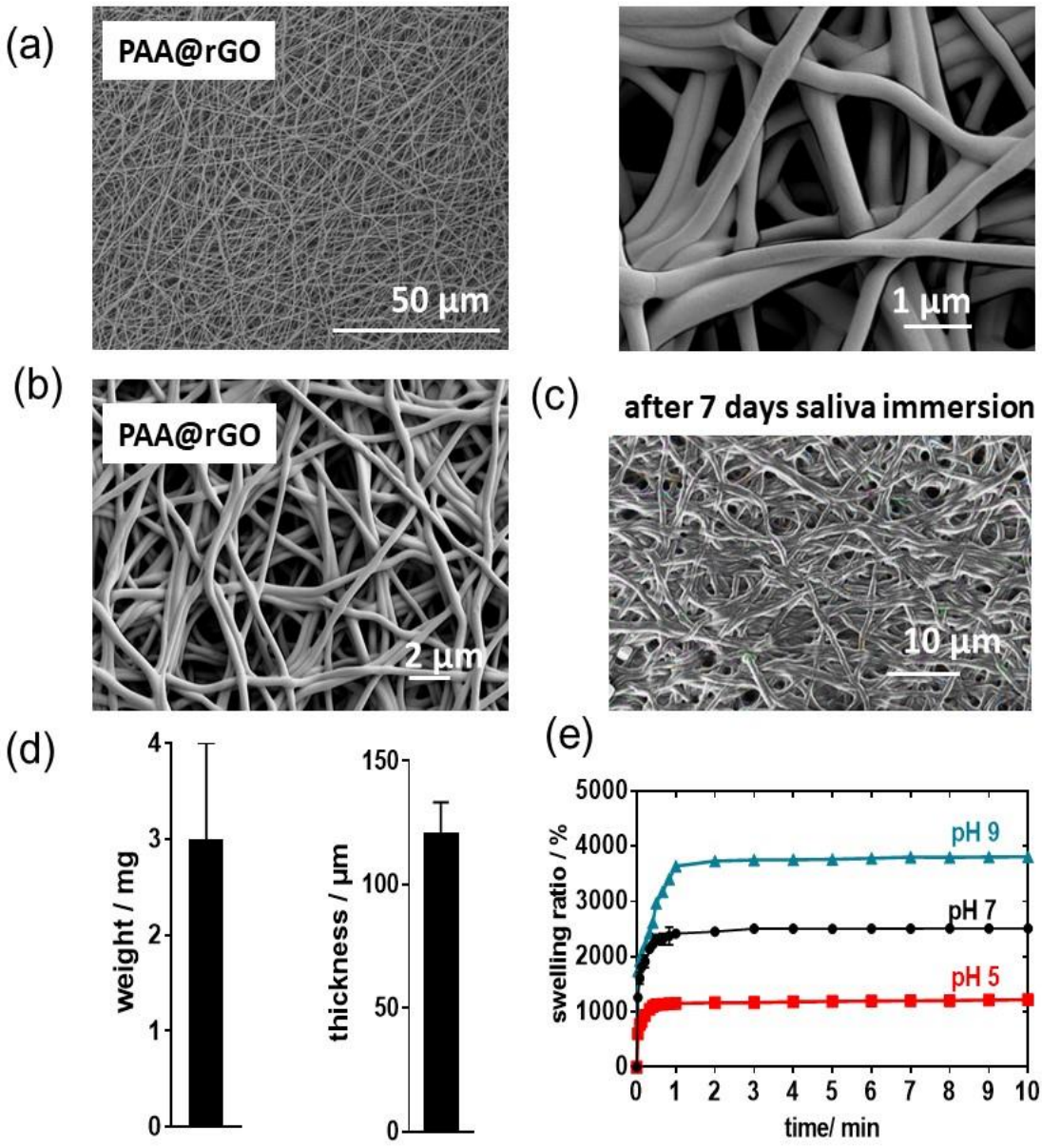

Figure 2.2. Characteristics of mucoadhesive PAA@rGO fibre mats: (**a**) SEM images of PAA@rGO at different magnifications (left 1000×, right 15000×). (**b**) SEM of PAA@rGO after immersion in water for 1 week at 37°C. (**c**) Stability of the nanofiber film immersed in artificial saliva solution for 1 week at 37°C. (**d**) Weight and thickness characteristics of four different batches of PAA@rGO. (**e**) Swelling behaviour in water over time as a function of pH.

Fiber mats assessed from four different batch fabrications were observe to have an average weight of 3.2±1.0 and thickness of 120±18 μm (**Figure 2.2d**). The degree of swelling was fast **(Figure 2.2e**), reaching up to 2000 % of its weight in the first 30 s and a steady state after 1-2 min, with a strong swelling when exposed to alkaline pH. The results of swelling behaviour correlate with other works,[202] where the swelling ratio increased with increasing solution pH.

The presence of rGO was validated by the characteristic Raman bands at 1350 cm^{-1} (D-band) and 1580 cm^{-1} (G-band) (**Figure 2.3a**). The presence of rGO endows the mucoadhesive patch with photothermal properties (**Figure 2.3b**). Irradiation of PAA@rGO with a near infrared laser (980 nm, 500 $mWcm^{-2}$) resulted in a surface temperature of 51±2 °C within 5 min. The mechanical properties of PAA@rGO were also assessed (**Figure 2.3c**). The maximal displacement at which the applied force dropped abruptly is identified as the breaking point[203] between the patch and the mucoadhesive surface, buccal tissue in our case. PAA@rGO adheres well to the buccal tissue and shows a mucoadhesive force of 0.74±0.3 N cm^{-2}, in the order of previously reported mucoadhesive forces.[204] The results of mucoadhesion for PAA-based patches correlate with the studies of Park et al.[205], where the authors describe the dependency of mucoadhesion on carboxyl-group density of polyacrylic acid and suggest that mucoadhesion occurs according to adsorption mechanism[206], in particular through hydrogen bonding.

The biocompatibililty of PAA@rGO mats was assessed on the HeLa and ARPE-19 cell lines (**Figure 2.3d)**. The toxicity was evaluated using the resazurin assay, based on the conversion of non-fluorescent dye to a fluorescent molecule by mitochondrial and cytosolic enzymes. No loss in cell viability and loss of metabolic activities was observed upon incubation of both cells for 24 h respectively. Lack of cytotoxicity suggests that no residual monomers, which could lead to potential cytotoxicity, are. Furthermore, eventual detrimental effect of thermal activation of PAA@rGO patch on cell viability was determined. Thermal activation of the PAA@rGO mats for 10 min at 500 mW cm^{-2} did not induce any change in cell viability.

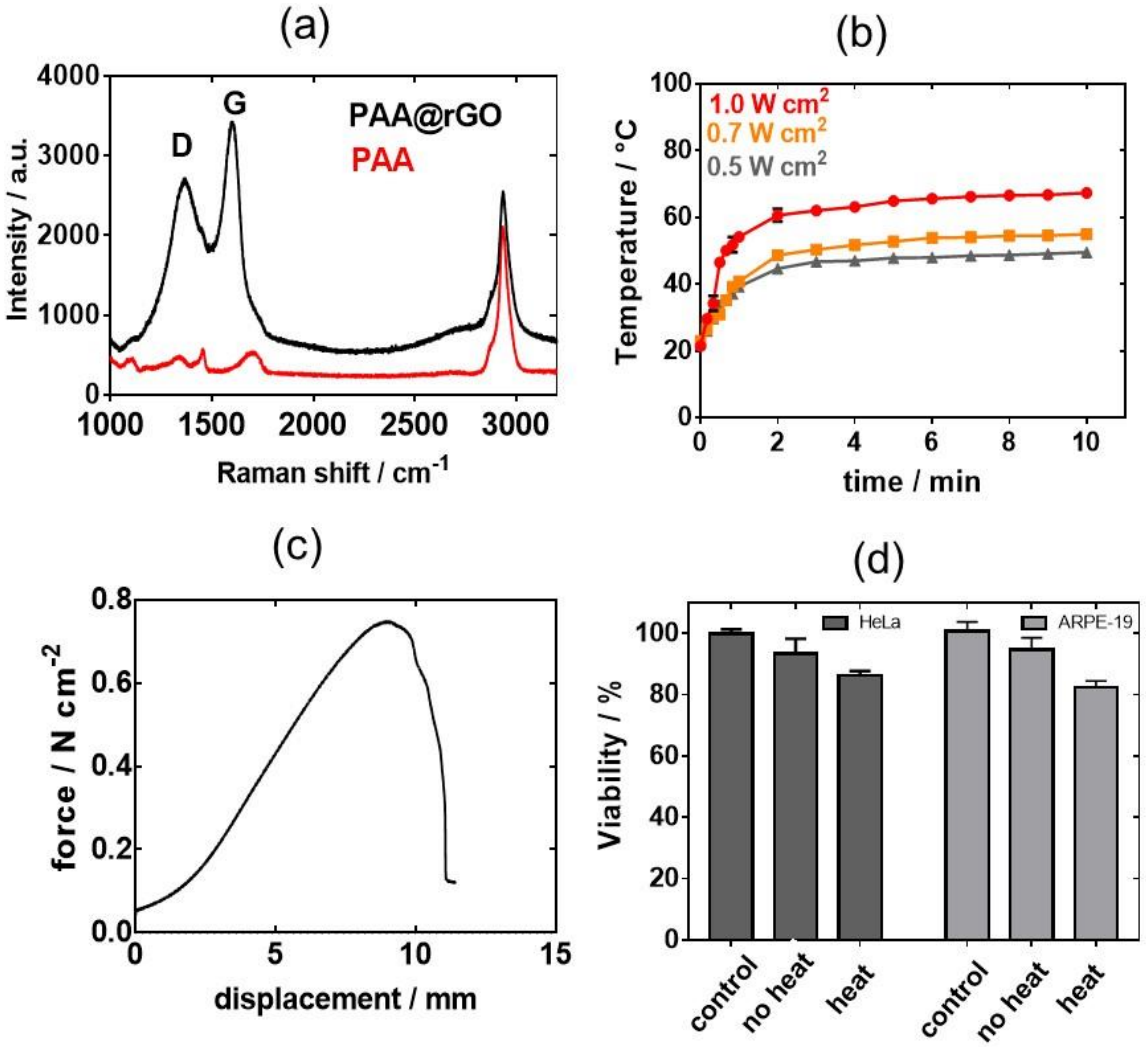

Figure 2.3. Characterization of PAA@rGO. (**a**) Raman spectra of PAA and PAA@rGO mats. (**b**) Photothermal heating curves of the patch at 980 nm illumination as a function of power density (0.5-1 W cm^{-2}). (**c**) Tensile tests via Force-displacement curve of PAA@rGO on porcine buccal mucosa. (**d**) Cell viability of ARPE-19 and HeLa cells in the presence of PAA@rGO without and with heat activation at 0.5 W cm^{-2} for 10 min.

2.3. Insulin-loaded mucoadhesive PAA@rGO patches

Diabetes is one of the leading causes of early mortality worldwide.[207] As all current antidiabetics are unable to achieve a long-term glycaemic control, insulin administration remains currently the only option to control blood glucose levels efficiently. To decrease blood glucose concentrations, 250-330 nM (145-192 µg mL^{-1}) of insulin is needed. Human insulin (200 µg mL^{-1}) was consequently integrated into PAA@rGO fibre mats through the simple immersion of the sample for 3 h under continuous shaking at 4 °C. The loading capacity for human insulin was evaluated through the determination of the concentration of insulin in solution before and after loading using HPLC, as reported recently.[208]

Insulin could be loaded (89% loading efficiency) onto the mucoadhesive patches over a time span of 60 min (**Figure 2.4a**). These loading efficiencies are comparable to rGO loaded hydrogels (80%), as reported by ref.[209] The loading capacity was found to be pH-dependent, with a higher insulin loading at pH 4 (**Figure 2.4a**). At pH 5 insulin is positively charged and interacts more strongly with the negatively charged backbones of PAA@rGO fibers.

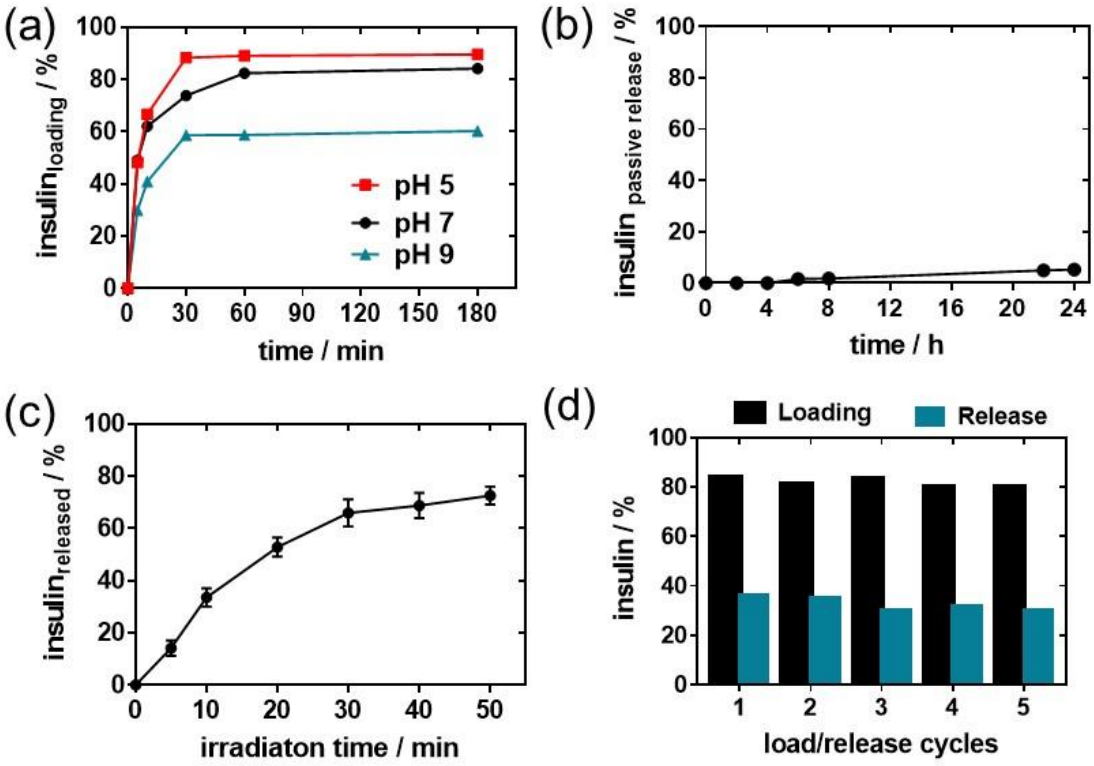

Figure 2.4. Insulin loaded PAA@rGO. (**a**) Human insulin (200 µg mL^{-1}) loading capacity as a function of solution pH. (**b**) Passive release over time. (**c**) Photothermal release with time upon illumination at 980 nm using a laser power of 0.7 W cm^{-2}. (**d**) Loading and release of insulin into the patch.

To determine the amount of insulin passively released from the mucoadhesive patch, the patch was immersed for 24 h in a solution of pH 7.4 (**Figure 2.4b**). About 5% of insulin was released, mostly due to some insulin being at the surface of the fibres, while most remained entrapped. Most importantly, after 24 h, no further insulin was released. This contrasts with the amount of insulin released upon photothermal irradiation for 10 min (**Figure 2.4c**).

The good heating capacity of the mucoadhesive patch results in an efficient heat triggered insulin release, reaching 150 μg (75%). Besides the sufficient photothermal release, PAA@rGO fibre mats featured appropriate reusability. Reloading of the mats with insulin followed by photothermal activation for 10 min could be performed with the same efficacy for 5 successive cycles (**Figure 2.4d**).

2.4. *Ex vivo* insulin permeation studies

The distinct keratinization of the oral mucosa negatively impacts on the passage of drugs through the mucosa and limits therapeutic efficiency.[210] The absorption of insulin from the patches through buccal mucosa (**Figure 2.5a**) has been assessed by *ex vivo* permeability studies, using pig-based models with close resemblance to the human buccal mucosa.[204, 211] For this, porcine buccal mucosa was separated from the underlining tissue using a scalpel, rinsed with PBS and fitted into Franz diffusion cells within 2 h after harvesting to preserve the membrane permeability and to ensure tissue integrity. To determine the permeability of insulin, electrospun fibre patch (1.5×1.5 cm^2, 2±0.3 mg) were loaded with 500 μg mL^{-1} of insulin by immersion into 1 mL solution at 4 °C for 1 h. With a loading efficiency of 82% (**Figure 2.4a**), this accounts for 410 μg mL^{-1} insulin integrated in the patch. This patch was placed on the top of the porcine buccal mucosa (**Figure 2.5b)** and both passive and heat-initiated permeations of insulin were assessed (**Figure 2.5c**). As expected, without heat activation, the insulin-loaded fiber mat showed limited insulin permeation through the epithelial cells of the porcine mucosa. In contrast, photothermal laser activation for 10 min resulted in substantial insulin penetration across the buccal tissue. After 6 h, 12±2% of insulin (which accounts for 41.1 μg mL^{-1} insulin) has permeated the porcine mucosa model, with about 16±1 % of insulin having been detected in the porcine lining. In total, the heat activated patches were able to transport 28±2 % (82 μg mL^{-1}) of the loaded insulin into the buccal lining. These findings are in line with recently reported buccal patches by Vaidya and Mitragotri using insulin loaded biodegradable polymeric patches using chitosan as mucoadhesive matrix and ionic liquids (ILs)/deep eutectic solvent (DES) as the transport facilitator.[204] An insulin flux of 16.6±2.9 μg cm^{-2} h^{-1} was recorded, being considerably elevated compared to that previously reported for photothermal activated insulin flux *via* porcine skin (as J=0.8±0.2 μg cm^{-2} h^{-1}).[209] It is in comparable with results using an electrothermal activation approach with a flux using transdermal iontophoresis in and menthone as a skin enhancer.[212] As the buccal mucosa is deficient of a stratum corneum layer, insulin can pass unhindered into the entire buccal epithelium.

The efficient mucosal insulin delivery under heat might further arises from the fluidization of the upper epithelium of the buccal tissue upon temperature increase, thereby indicating a paracellular mode of insulin transport. Fluorescence analysis of harvested buccal tissue before and after heat treatment and delivery of FITC-labeled insulin (**Figure 2.5d**) showed no structural damage of the tissue at the application site with the fluorescence signal remaining localized to the outside the tissue without heat application. After 10 min heat application and observing the fluorescence stained tissue after 6h, fluorescence of 500 µm in depth is observed, equal to the thickness of buccal non-keratinized structures. Eventual, the increased temperature induces mucus thinning effect and the protective role of PAA@GO against saliva proteases could be reasons for the efficient insulin delivery.

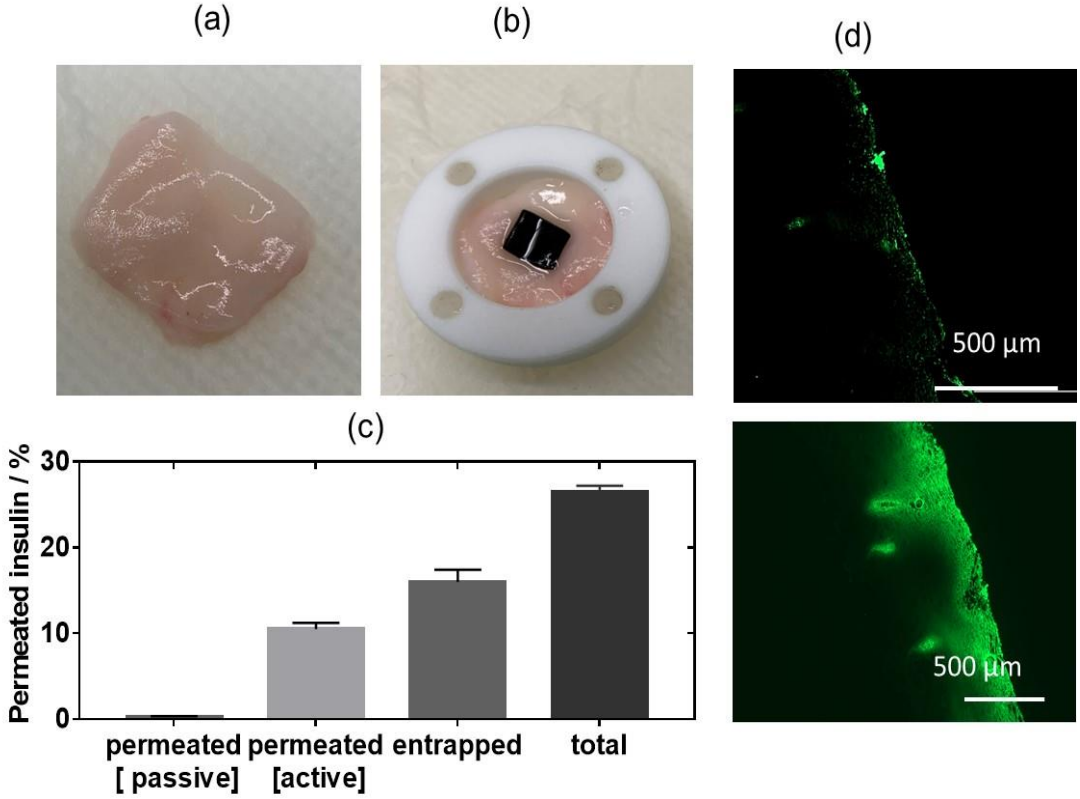

Figure 2.5. *Ex vivo* insulin permeation studies of insulin-loaded PAA@rGO nanofiber mats *via* porcine buccal mucosa: (**a**) Photographic image of porcine buccal tissue harvested and used for permeation studies. (**b**) Photograph of porcine buccal tissue fixed into Franz diffusion cell and immobilization of insulin-patch on top. (**c**) Cumulative permeation profile of insulin through the buccal tissue after 6 h upon passive or photothermal activation (10 min action with laser at 980 nm). Error bars represent means of ± SEM (n=3). (**d**) Fluorescence images of buccal tissue treated with a FITC-insulin loaded PAA@rGO patch passively (above) and with (10 min, 980 nm, 500 mW cm^{-2}) activation (below).

In addition, comparable experiments were performed on pig cornea (**Figures 2.6a, b**), coated with a mixture of mucus, epithelial cells, proteinaceous and lipoidal material that adhere firmly to the corneal surface. Permeation of insulin *via* the pig cornea was comparable to that of pig buccal mucosa, with limited passive diffusion; 13±1% of insulin permeated the cornea and 25±1% remained on the cornea tissue after 6 h, corresponding to a total insulin of 37±1% i.e. 151±3 μg mL^{-1} and an insulin flux of 24.3±3.1 μg mL^{-1} h^{-1} (**Figure 2.6c**). This flux is several-times larger than that achieved using photothermal activation *via* porcine skin and 1.5 times using buccal mucosa.

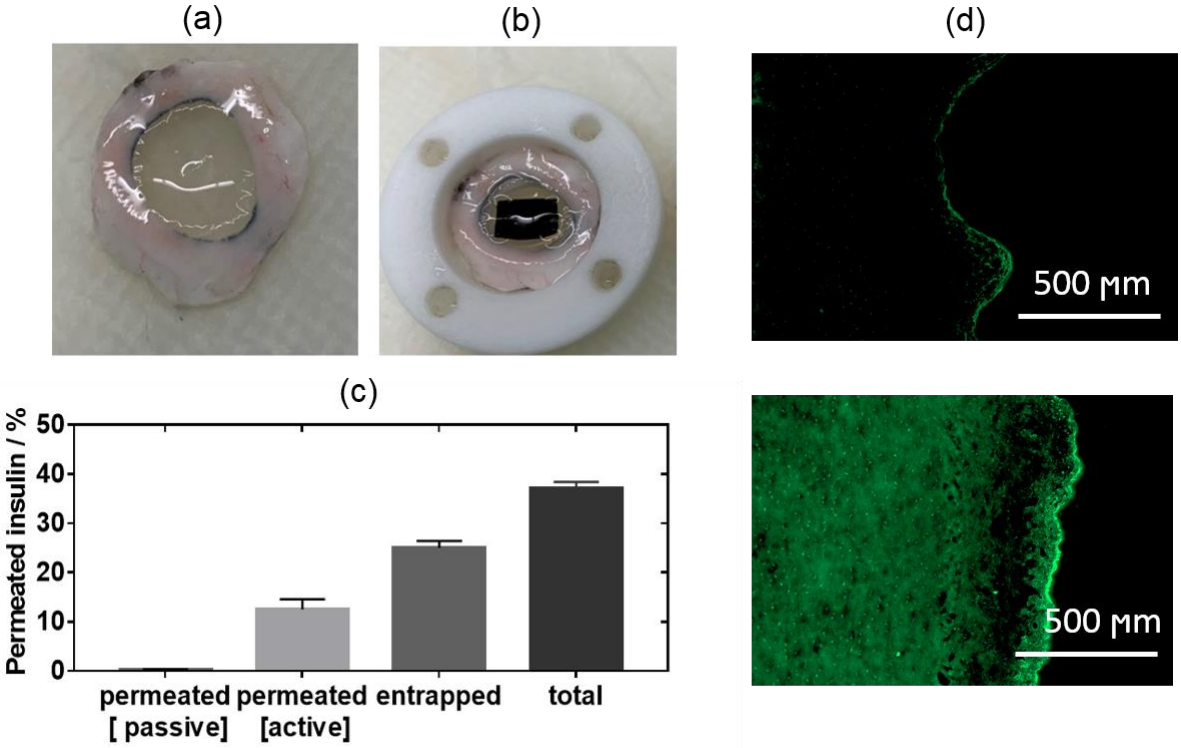

Figure 2.6. *Ex vivo* insulin permeation studies of insulin-loaded PAA@rGO nanofibers mats *via* porcine cornea: (**a**) Photographic image of porcine corneal tissue harvested and used for permeation studies. (**b**) Photograph of porcine corneal tissue fixed onto Franz diffusion cell and immobilization of insulin-patch on top. (**c**) Cumulative permeation profile of insulin through the cornea after 24 h upon passive or photothermal activation (10 min irradiation at 980 nm, 500 mW cm^{-2}). Error bars represent means of ± SEM (n=3). (**d**) Fluorescence images of corneal tissue treated with a FITC-insulin loaded PAA@rGO patch passively (above) and with (10 min, 980 nm, 500 mW cm^{-2}) activation (below).

2.5. *In vivo* mucoadhesive properties and acceptability of PAA@rGO nanofibers mats by volunteers

Finally, we applied PAA@rGO nanofibers mats to 6 healthy adult volunteers (3 male, 3 female) aged between 25 and 49 years to obtain information about *in vivo* residence time and patch acceptability (**Figure 2.7ab**). The adhesion evaluated for a time span of 120 min was excellent, with all bandages residing for 120 min in the 6 cases (**Figure 2.7b**). The volunteers rated the patch as excellent (note of 9.3) with most of volunteers feeling comfortable (note 8.3) while wearing the patches in the buccal cavity. 2 male volunteers considered it "mentally" difficult to have a nanomaterial in the mouth and the discomfort was related to this rather than the bandage itself. All volunteers agreed that the patches have no taste (note 10). The rating for removing the bandage is evaluated as medium (note of 6.1) indicating that it remains difficult to remove the bandage once installed removal easy. None of them reported interference with speak nor effects on saliva production and swallowing.

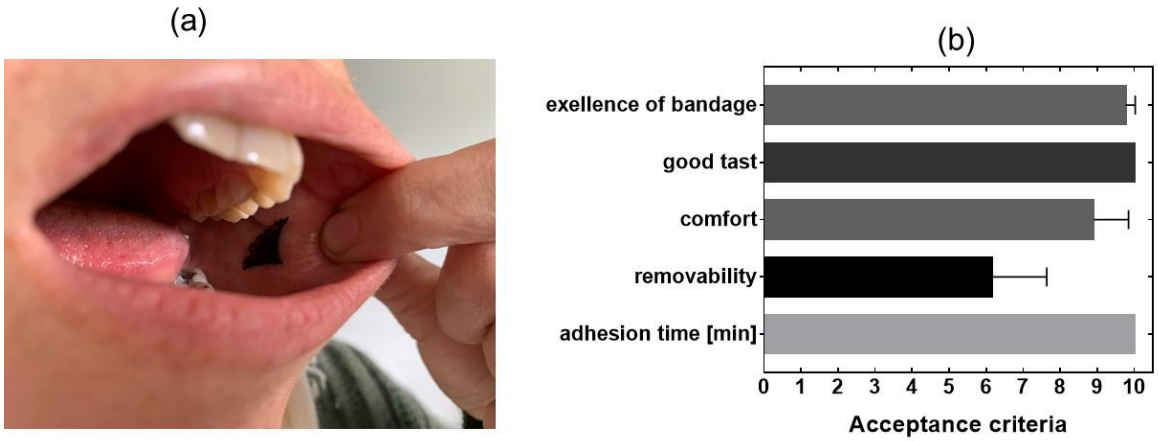

Figure 2.7. *In vivo* mucoadhesive performance of PAA@rGO nanofibers mats placebo: (**a**) Photograph of placement of mucoadhesive patches in humans attached by 5 s pressure application. (**b**) Acceptability evaluation of 6 adult volunteers on the adhesion time, overall bandage excellent, comfort, taste and removability in a scale of 0 (bad)-5 medium-10 (excellent).

2.6. Conclusion

In this chapter, the utility of a poly(acrylic acid) (PAA) based fiber mat for photo-thermal initiated insulin delivery was demonstrated. Reduced graphene oxide (rGO) was the photothermal agent in these fibers, formed by electrospinning of poly(acrylic acid) (PAA) in the presence of β-cyclodextrin as a cross-linker resulting in water insoluble mucoadhesive fiber mats. The resulting hydrogel fiber mat allowed an efficient loading of a therapeutic peptide like insulin, while maintaining a good fibrous morphology. The flux of insulin across the mucosal lining of porcine buccal mucosa as well as porcine corneas as *ex vivo* models was investigated. reaching J=16.6±2.9 μg cm^{-2} h^{-1} for buccal mucosa and J= 24.3±3.1 μg mL^{-1} h^{-1} for porcine cornea. This result confirms that buccal mucosa is suitable for the non-invasive delivery of insulin via electrospun fiber mats-based mucoadhesive patches. Efficient release of insulin by photothermal activation supports the idea of using mucoadhesive patches containing insulin for treating patients with diabetes. For type 2 diabetes, which is most prominent form of diabetes, basal insulin therapy is often added to oral diabetes medication regimens that do not provide optimal glucose management. In general, this biotherapy does not require high dose of insulin. The quantity of insulin released from our mucoadhesive patches could be in line with their use in basal therapy. Therefore, compared to multiple insulin injection, this mode of delivery offers a huge advantage by increasing the compliance of diabetes-treated patients, as it is resilient and can be easily self-administrated. In this perspective, this study allows for future preclinical studies aiming to test the efficiency of this original platform to on-demand deliver insulin and to treat diabetes in animal models of diabetes. Although these dates can not be directly related to human buccal mucosa since porcine mucosa epithelium is about 3-times thicker than in humans, insulin released from PAA@rGO fiber mats clearly show to penetrate buccal mucosa lining deeply.

CHAPTER 3:

In vivo studies of minimally invasive insulin loaded insoluble microneedles on pigs

The content below was done in collaboration work with Bilal Demir (CEA-TECH Region, Lille, France). The microneedles were fabricated by Bilal Demir. The author performed or coordinated *in vivo* studies on pigs.

3.1. Introduction

Microneedle-based technologies have in particular opened promising avenues to overcome the barrier of the skin's stratum corneum for larger therapeutic agents such as proteins and peptides.[213-216] Having been discovered several decades ago, microneedles delivery systems have gained much attention only in the middle of 1990s. By now, a large variety of microneedle arrays (MNs) have been manufactured including polymeric [217-225], silk fibroin[226-229], as well as hydrogel-based microneedles [230-235]. So far, next to hollow microneedles [236], biodegradable systems [229, 235] as well as swelling microneedles [231] are engineered for improving the delivery of therapeutics over a prolonged time. Drug delivery using swelling has the advantage over biodegradable systems that they are reusable. Often the amount of released drug is limited. Drug release from microneedles upon an external stimulus is one way to overcome these limitations. To this end, photothermal active graphene oxide (GO) was integrated into dissolvable polymeric microneedles, but to reinforce the scaffold rather than providing it with a stimuli-responsive matrix. Light to heat converting approaches might be an additional consideration. In addition, microbial contamination and infection of the micropores formed by microneedles represent an important issue to overcome. Heat produced along the tips of the microneedle array might be one way of limiting this effect. We found that many of the challenges can be addressed by the application of microneedles prepared from gelatin methacrylate (GelMA) crosslinking with polyethylene glycol diacrylate (PEGDA) (**Figure 3.1a-b**). GelMA is a hydrogel that has gained popularity recently as a photo-cross linkable biomaterial for tissue engineering applications [235, 237] as well as for sustained release of proteins [238]. In this work, we opted for the integration of molybdenum sulfide nanosheets (MoS_2 NSs) [239-241]. While two-dimensional (2D) materials such as graphene oxide (GO) [242] and reduced graphene oxide (rGO) [243-247] have been successfully integrated into various hydrogels and fiber mats, we assessed the suitability of MoS_2 as a photothermal component in the MNs delivery system.

MoS_2, a layered semiconductor with a narrow band gap (1.2 eV for multilayer MoS_2), exhibits a strong near-infrared (NIR) optical absorption and is well-adapted for biomedical applications where NIR photothermal activity and chemical stability are required [240]. In contrast to peptides and proteins adsorption on GO and rGO nanosheets, where H-bonding, π–π stacking and/or electrostatic interactions are dominating, molecular dynamics simulations validated that aromatic residues of peptides and proteins do interact less strongly with MoS_2 nanosheets [248]. Therefore, release of therapeutic peptides such as insulin should be favored under these conditions.

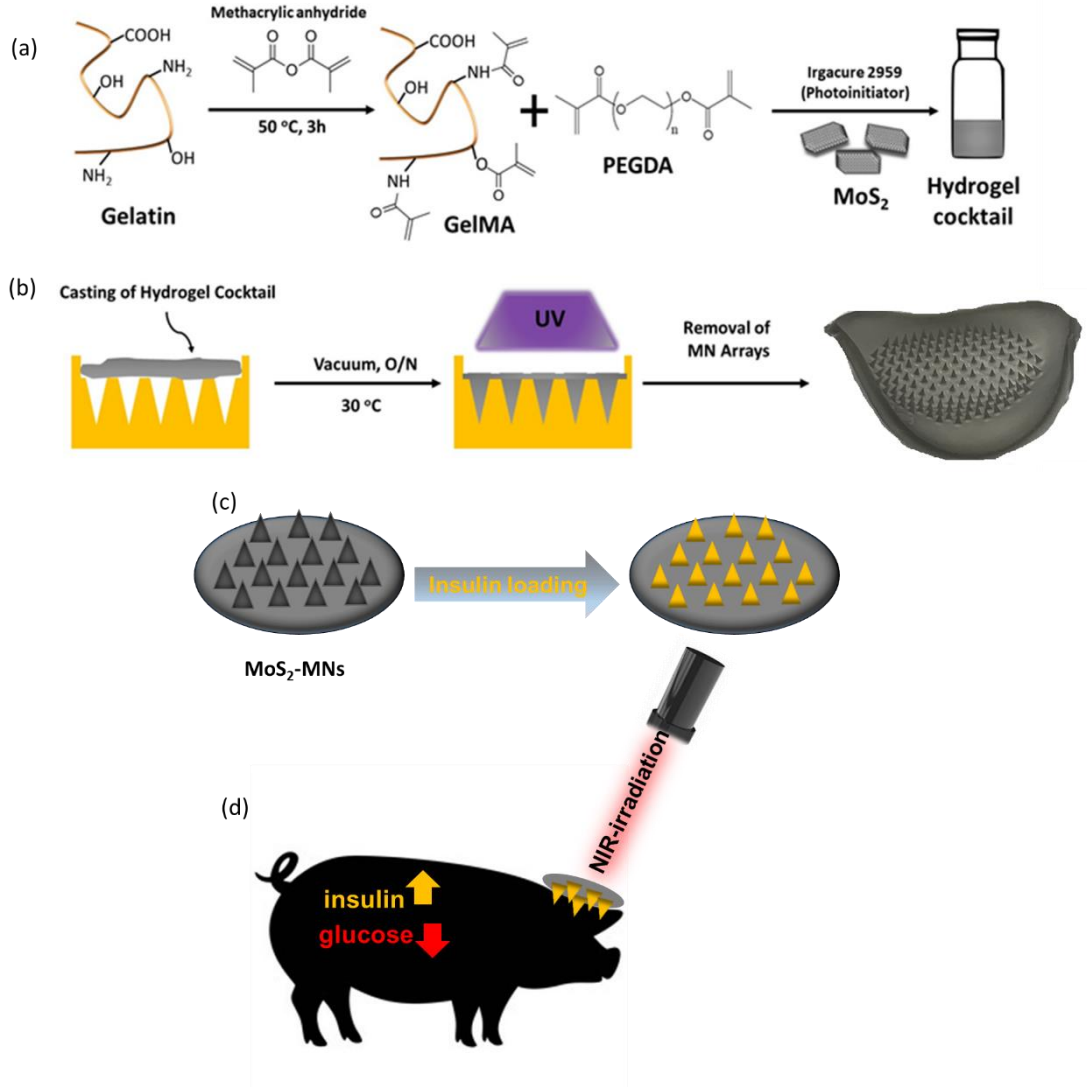

Figure 3.1. (**a**) Schematic representation of MoS_2-hydrogel cocktail preparation. (**b**) Process of microneedles formulation. (**c**) Illustration of loading of insulin into MoS_2 microneedles. (**d**) Near-infrared (NIR) light triggered on-demand delivery to control the glycemic level in pigs.

3.2. Fabrication of MoS_2 loaded microneedles based on GelMA and PEGDA hydrogel

Gelatin methacrylate (GelMA) hydrogels are formed when methacrylic anhydride reacts with the primary amine groups of gelatin at 50°C (**Figure 3.1**). The formed GelMA can be crosslinked under UV irradiation in the presence of an appropriate photo-initiator, which upon UV light absorption, generated free radicals that subsequently induced GelMA polymerization. The critical factors influencing the final physio-chemical properties of GelMA hydrogels are, next to the degree of gelation functionalization, the parameters of photo-crosslinking such as exposure time and UV intensity. In this study, GelMA was mixed with polyethylene glycol diacrylate (PEGDA), a commercially available hydrogel precursor with equal photopolymerization properties like GelMA, and MoS_2 to obtain a hydrogel cocktail for the fabrication of microneedles (**Figure 3.1a-b**). PEGDA, owing to its polyethylene glycol (PEG) units, provides an additional hydrophilic environment necessary for preserving the biological activity of many biomolecules, as insulin [247]. The incorporation of MoS_2 endows the MNs with photothermal heating properties (**Figure 3.2b**). Irradiation of hydrogels without and with increasing amounts of MoS_2 resulted in a fast light to heat conversion reaching more than 80°C for MNs hydrogel formed using 1.2 mg MoS_2 and 5 min irradiation. Indeed, MoS_2 exhibits an absorption bands in the UV-Vis as well as in the NIR (**Figure 3.2a**) adapted for photothermal heating [249].

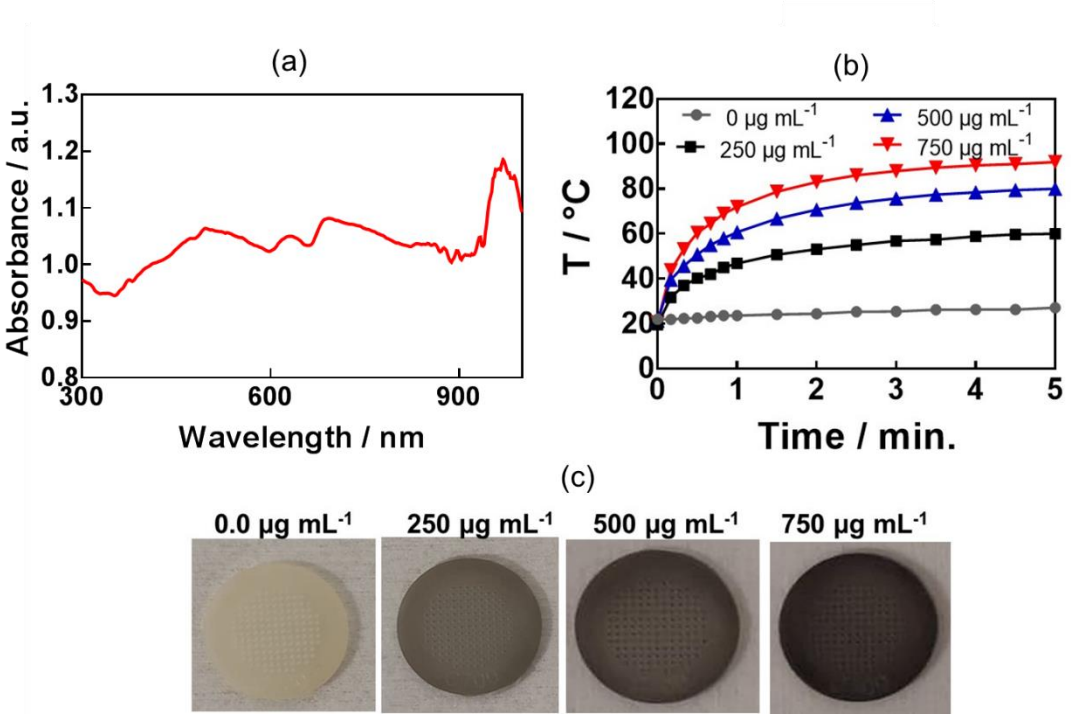

Figure 3.2 Characterization of MoS_2-MNs array formed from a GelMA:PEGDA cocktail using different amounts of MoS_2: (**a**) UV-Vis spectrum of MoS_2 dispersion in water.

(**b**) Photothermal heating properties of the MoS_2-MNs array under irradiation with a laser at 980 nm (0.5 W cm^{-2}) as a function of MoS_2 amount in the hydrogel cocktail. (**c**) Photographic images of the MNs with increasing amount of incorporated MoS_2.

3.3. *In vitro* characterization of insulin-loaded MoS_2-MNs patch

The loading capacity of the MoS_2-MNs patch for insulin was investigated in the following by keeping the patch immersed in 100 µg mL^{-1} of insulin at 4°C for 8h (**Figure 3.3a**). The entrapment efficiency, determined by HPLC from the insulin remaining in solution [250], was as high as 80±2% (80 µg of insulin), which correlates to 2.3 IU for hydrogels formed using 5 min UV irradiation . Generally, to correct high concentrations of blood sugar in humans, 0.3-1.0 IU kg^{-1} insulin is needed to decrease the blood glucose by 50 mg dL^{-1}.

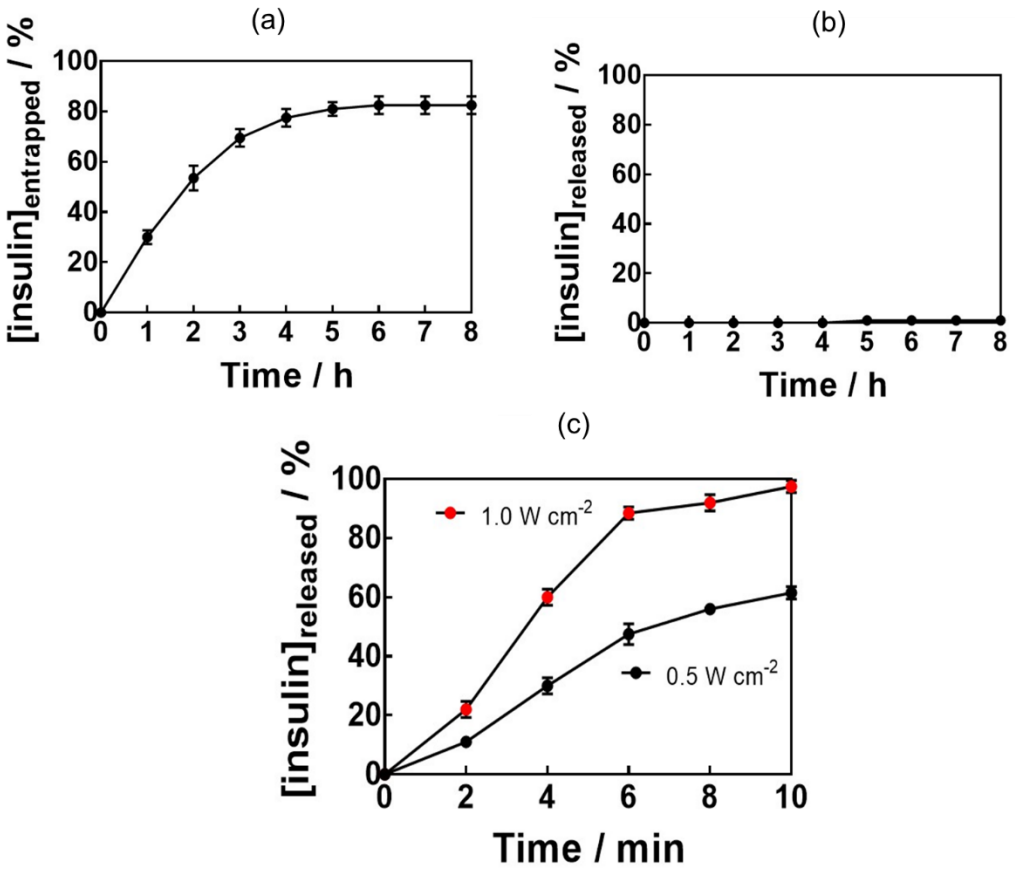

Figure 3.3. **Insulin entrapment and release behavior of MoS_2-MNs patches:** (**a**) Entrapment efficiency of human insulin into MoS_2-MNs formed from hydrogel cocktails containing 500 µg mL^{-1} of MoS_2. Loading with insulin was achieved by keeping the MNs at 4°C for 8h. An insulin stock solution of 100 µg mL^{-1} was used and corresponds to 100%. (**b**) Passive cumulative *in vitro* release profile of insulin from the patch into PBS (pH 7.4). (**c**) Cumulative *in vitro* release

profile of insulin from the patch in PBS (pH 7.4) upon application of different laser power densities at 980 nm, as determined by HPLC: 1.0 W cm^{-2} (red) or 0.5 W cm^{-2} (black) for 10 min. Results are presented as the mean ± standard deviation of four experiments.

To evaluate the passive release characteristics of the MoS_2-MNs patch, they were immersed into PBS at 37°C (body temperature) for 12 h. Not more than 1 µg of insulin could be detected from the 80 µg loaded into the gel, indicating that passive release was restricted (**Figure 3.3b**). **Figure 3.3c** depicts the cumulative *in vitro* release profile of insulin from the MoS_2-MNs array into PBS (pH 7.4) upon laser irradiation for 10 min with a laser power of 0.5 or 1.0 W cm^{-1} at 980 nm. In a time span of several minutes, up to 100 µg of insulin were released from the patch in a power density-dependent manner.

3.4. *In vitro* pharmacodynamic response of insulin-loaded MoS_2-MNs array patch

Figure 3.4a exhibits a standard permeation profile of insulin recorded for MoS_2-MNs patch loaded with 100 µg of insulin. The high molecular weight and hydrophilic character of insulin restricted passive skin permeation and no skin permeation of insulin was detected without photothermal activation. When a mouse skin was subjected to 10 min heating at 0.5 W cm^{-2} after a lag time of about 20 min, sustained transdermal transport of insulin occurred over a time period of 3 h. The total amount of permeated insulin after 2 h equals to 20.3 ± 2.5 µg, which is superior to other integrated microneedles [231], corresponding to an insulin flux of 15.6 ± 1.3 µg cm^{-2} h^{-1} (2.0 ± 0.4 µM cm^{-2} h^{-1}), reported by Pillai et al. addressing insulin delivery from poloxame-407 gels using transdermal iontophoresis in the presence of menthone as a skin enhancer [251].

The activity of released insulin was evaluated, *in vitro*, on a immortalized human hepatocytes (IHH) cell line model using native insulin as a positive control and the same culture without insulin as a negative control as described previously. [252] **Figure 3.4c** indicates that the insulin activity (Akt phosphorylation, pAkt/Akt ratio) increased when IHH cells were treated with native insulin in comparison to non-treated cells (p-Akt/Akt ratio of 3.7 versus 1.0 for the negative control). A comparable p-Akt/Akt ratio of 3.5 was determined on the released insulin, indicating that all the activity was preserved under photothermal release from MoS_2-MNs patch.

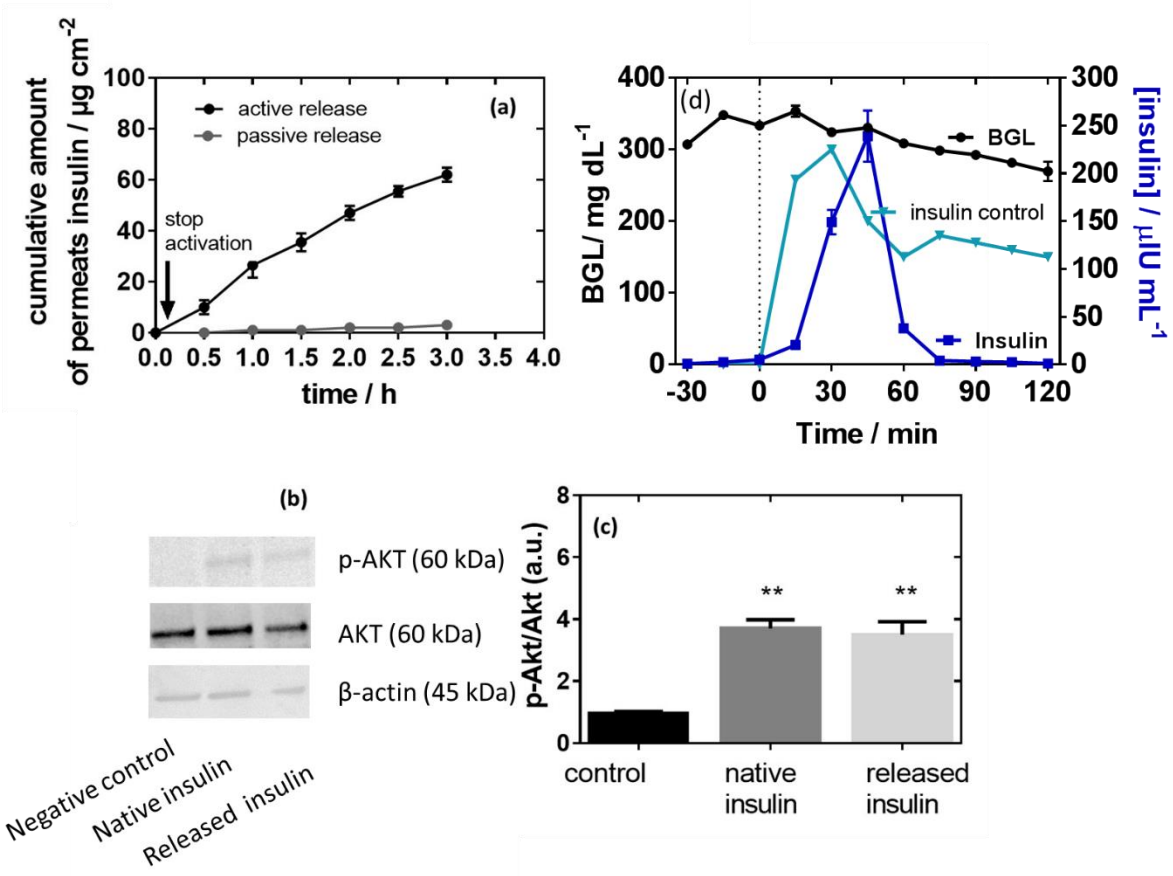

Figure 3.4. ***In vitro*** **and** ***in vivo*** **permeation studies:** (**a**) Cumulative permeation profile recorded for MoS_2-MNs arrays loaded with 100 µg of insulin passive (grey) and active (black) upon laser irradiation (980 nm) for 10 min at 0.5 W cm^{-2} (n=3). Error bars represent means of ± SEM. (**b**) Insulin activity determined on IHH cells via Western blotting of p-Akt/Akt cell lysates from IHH cells incubated under several conditions: without insulin, with native insulin or with photoreleased insulin; (**c**) Insulin activity shown by the ratio between p-Akt and Akt (A.U.) for all the samples in comparison to a negative control (control) (cells without insulin treatment). One-way ANOVA and multicomparisons test. The results are expressed as the mean ± SEM of at least 3 independent samples for each group, (*$p < 0.05$, **$p < 0.01$). (**d**) Measurement overtime of blood insulin (dark blue line) and blood glucose level (BGL, black line) in minipig carrying MoS_2-MNs arrays (MNs) patch loaded with human insulin (2.88 IU). In a control experiment (bright blue), insulin was injected subcutaneously (2.88 IU) and blood insulin was dosed over time.

3.5. *In vivo* pharmacodynamic response of insulin-loaded MoS_2-MNs array patch

To investigate the efficiency of the MoS_2-MNs arrays to lowering blood glucose level (BGL), MoS_2-MNs arrays loaded with 100 μg mL^{-1} (2.88 Insulin units) of insulin were applied on the pancreatectomized Göttingen minipig as a valuable model of insulin-dependent diabetes.[253] Subcutaneous insulin injection was used as a control. Of particular relevance, diabetic minipigs share many similarities with humans with regard to pharmacokinetics of compounds after subcutaneous administration, structure and function of the gastrointestinal tract, morphology of the pancreas, and the overall metabolic status of the two species.[254-255] Application of a MoS_2-MNs array loaded with human insulin on the ear of the minipig resulted in a reduction of the BGL after 30 min from the start of the patch application. The decrease of the BGL coincides with a peak in the plasma insulin concentration, confirming the hypoglycemic effect of insulin released from the patch (**Figure 3.4d**).

3.6. Conclusion

In this chapter we presented the first on-demand insulin delivery strategy via microneedles using photothermal activation rather than dissolution of microneedles to liberate the cargo. We showed that microneedles formed using molybdenum sulfide nanosheets loaded onto crosslinked gelatin methacrylate with polyethylene glycol diacrylate represent an appealing platform for on demand insulin delivery under NIR irradiation. The *in vitro* insulin release profile revealed a remarkable fast release rate, which can be tuned via the applied laser light power. The presence of MoS_2 allowed microneedles to show photothermal behavior. The heating properties of the MoS_2-MNs array under irradiation with a laser at 980 nm (0.5 W cm^{-2}) were found to be depended on the amount of MoS_2 in the hydrogel cocktail. The *in vivo* glucose tolerance test as well as an insulin transdermal delivery were tested on mini-pigs, underlying the ability of the smart insulin patch for clinical opportunities for type 1 diabetic patients for pin-free and safe insulin delivery.

CHAPTER 4:

Near-infrared light activatable hydrogels for metformin delivery

The content below is based on an article content that was published in collaboration work with Chengnan Li. The hydrogels were fabricated by Chengnan Li. The author performed the characterizations and *in vitro* studies.

4.1. Introduction

Advancements in materials science have impacted positively to the development of on-demand drug delivery.[256] Among the various external stimuli, the high spatial and temporal resolution of near-infrared (NIR) light, has shown to be highly beneficial for drug delivery.[257-260] NIR-triggerable drug delivery platforms are largely based on NIR absorbing nanomaterials, notably on reduced graphene oxide (rGO) based matrixes.[180, 261-263] The effectiveness of rGO as NIR-absorbing photothermal agent compared to other carbon allotropes is due to the rapid light-to-heat conversion of rGO under low-power NIR irradiation. This has made rGO preferential filler in polymeric blends and composite hydrogels.[264-269] Next to efficient drug delivery, near-infrared light has also been considered as external trigger to enhance transdermal drug delivery.[177, 180, 259, 261, 270-271] Transdermal drug delivery systems are more and more considered for personalized medicine and are a pain free alternative to hypodermic injections. [271-272]

In this chapter, the formulation of light responsive transcutaneous patch, based on gelation between rGO and metformin will be shown as well as its use for the transdermal delivery of metformin.

Metformin hydrochloride is a commonly used anti-hyperglycemic agent and represents currently the first line drug in the management of type 2 diabetes.[273] While metformin is conveniently administered orally in the form of tablets, some patients experience side effects including nausea, abdominal pain and indigestion, often leading to a discontinuation of the treatment. Furthermore, metformin exhibits an unfavorable pharmacokinetics profile, with low and variable oral bioavailability (50-60%) and a biological half-life time in the range of 0.9-2.6 h.[273-274] Therefore, frequent applications of high doses of metformin (0.5-2g twice daily) are required for an effective treatment. To overcome these limitations, transdermal delivery of metformin has been identified as an effective alternative.[259, 275-279] The transdermal administration route allows metformin to be delivered into the body bypassing

the gastrointestinal tract and avoiding many of the unpleasant side effects. Additionally, the enhanced bioavailability of metformin allows reducing the administered daily dose amount and its frequency. The transdermal delivery of metformin is currently limited to the use of thermo-responsive microneedles, where metformin is released upon needle melting,[259, 275, 278-279] and the use of hydrogel-based microneedles.[277] The advantage of hydrogel-based microneedles over thermo-responsive microneedles is that once applied to the skin they can be withdrawn and remain intact. Onto these microneedles metformin reservoirs were integrated to have access to a sufficient amount of metformin.

In this chapter, we investigate the potential of thermo-responsive metformin gels as a transdermal controlled release system. Hydrogels are extensively used in controlled-release systems due to their hydrophilic character and good biocompatibility. These systems are commonly prepared using self-assembly processes and benign conditions in contrast to polymeric gels for which toxic photo-initiators and cross-linkers are employed for their formation. [180, 280] We show here that simple mixing of metformin with graphene-based derivatives, such as graphene oxide (GO) or carboxylated reduced graphene oxide (rGO-COOH), as cross-linkers in a volume ratio of 1/9 results in metformin gel formation. The gelation process is believed to be driven mainly by hydrogen bonding and electrostatic interactions. Photothermal activation of GO/metformin and rGO-COOH/metformin gels results in a stepwise dissolution of the gel and release of active metformin. *In vitro* assessment of the key target Glucose-6 Phosphatase (G6P) gene expression using Human hepatocyte model[252] confirmed that metformin activity[281] was unaffected by photothermal activation.

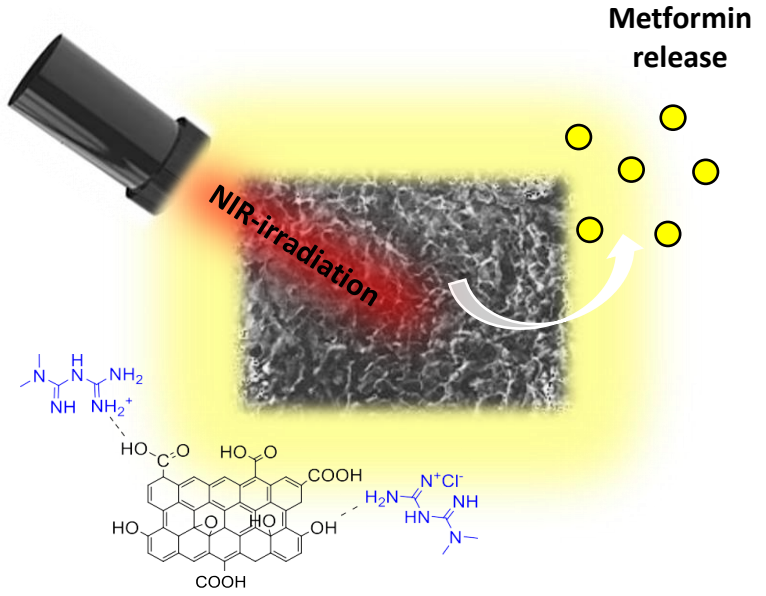

Figure 4.1. Schematic representation of metformin release from GO/metformin hydrogels trigged by NIR laser.

4.2. Metformin hydrogels using graphene oxide (GO) as a cross-linker

Figure 4.2a depicts the formation of a metformin hydrogel, using graphene oxide (GO) as a cross-linker. The hydrogel is obtained under mild conditions by mixing GO/metformin in a weight ratio of 10/1. **Figure 4.2b** exhibits the SEM images at different magnifications of a lyophilized sample, revealing a porous structure with a pore size of about 10±5 µm. The characteristic Raman features of GO and the GO/metformin gel present the G band centered at around 1585 cm^{-1} corresponding to the in-plane sp^2 C-C stretching, and the D band at 1350 cm^{-1} due to defects in the GO structure (**Figure 4.2c**) . The ratio of ID/IG is 0.76 for GO and increased to 0.93 for GO-metformin arguing for an increase in defects due to the gelation process. The UV-Vis spectrum of GO/metformin (**Figure 4.2d**) comprises a strong absorption band in the ultraviolet at 233 nm, characteristic of metformin as well as contributions from GO (π-π* of the aromatic bonds at ~230 nm and a shoulder at ≈310 nm due to n-π* of C=O)[282], along with a slight increase of the absorption tail until the near-infrared region.

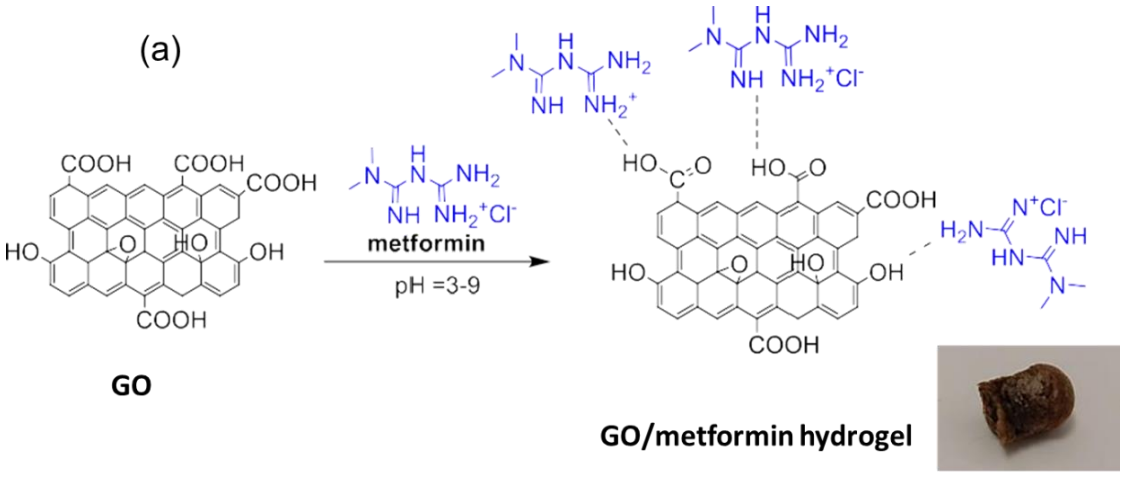

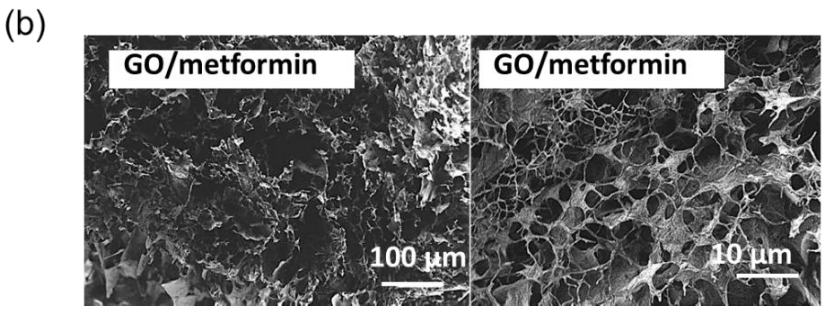

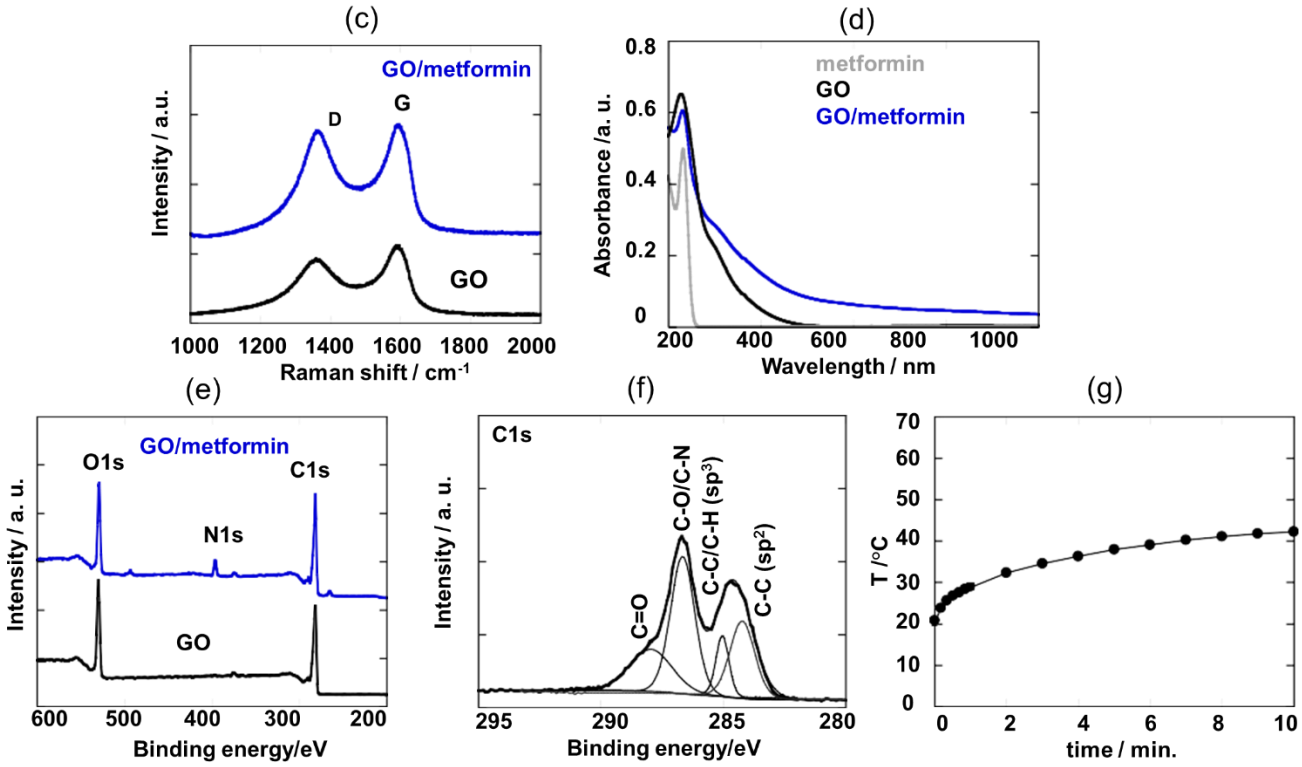

Figure 4.2. (**a**) Graphene oxide (GO) based metformin encapsulated hydrogel together with photographic image of the lyophilized gel. (**b**) SEM images of lyophilized GO/metformin gel. (**c**) Raman spectra of GO (black) and GO/metformin (blue). (**d**) UV-Vis of metformin (grey), GO (black) and GO/metformin (blue). (**e**) XPS survey spectra of GO (black) and GO/metformin (blue). (**f**) C_{1s} high resolution spectrum of GO/metformin. (**g**) Change of temperature upon laser irradiation at 980 nm (1 W cm^{-2}) for 10 min.

While the XPS survey spectrum of GO shows only the presence of C and O with a C/O ratio of 2.1, GO/metformin (**Figure 4.2e**) shows in addition the presence of nitrogen of 5.4 at. % . The C_{1s} high resolution spectrum of GO/metformin displays bands at 284.4, 285.0, 286.6, 288.3 eV corresponding to C=C (sp^2), C-C (sp^3)/C-H, C-O/C-N, and C=O, respectively (**Figure 4.2f**).[283] As metformin lacks aromatic structures, strong hydrogen bonding and electrostatic interactions between GO and metformin are believed to drive the gelation process.[269]

The photothermal heating curve of GO/metformin is in accordance with the UV-Vis spectrum: the hydrogel achieves a moderate heating capacity at 980 nm (**Figure 4.2g**), resulting in a solution temperature of 41°C after 10 min irradiation.

The stability of the GO/metformin hydrogel is strongly pH dependent (**Figure 4.3a**).[269] Immersion of GO/metformin gel into NaOH (0.1 M, pH 12) results in a fast decomposition of the gel most likely due to the deprotonation of –COOH groups of GO under basic conditions, decreasing hydrogen bonding occurrence with metformin. With a pKa of 12.4 for metformin breaking of electrostatic interactions with negatively charged GO can occur as well. Lowering the pH reduces the degree of negative charge on GO (**Figure 4.3c**) and electrostatic interaction; however hydrogen-bonding between GO and metformin limits the full collapse of the GO/metformin hydrogel until pH 3. The release profile of metformin at ambient conditions (T=23°C) is in accordance with the stability of the GO/metformin gels (**Figure 4.3b**): a release of about 5 µg mL^{-1} between pH 3 and 9, while the instability of the gel at pH 12 results in a complete release of metformin as expected. This high pH is, however, not adequate for most medical applications.

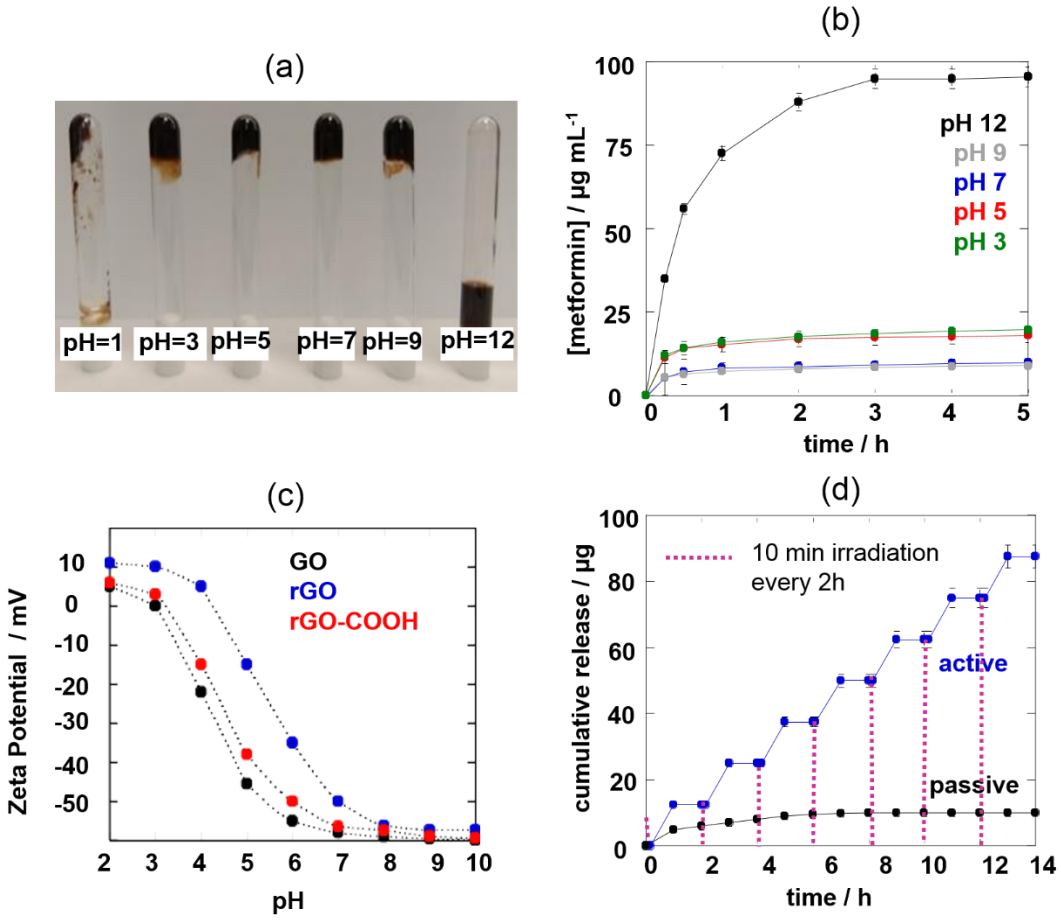

Figure 4.3. (**a**) GO/metformin gel formation as a function of solution pH. (**b**) Release profiles of metformin from freeze-dried samples upon immersion into solutions of different pH (3, 5, 7, 9, and 12). (**c**) Zeta potential of GO, rGO and rGO-COOH as a function of solution pH. The data points are averaged over three parallel experiments. (**d**) Metformin release from

GO/metformin gel into PBS (pH 7.4) upon photothermal irradiation of the GO/metformin gel at 980 nm (10 min at 1 W cm^{-2} every 2 h) in comparison to passive release.

The effect of photothermal heating on metformin release from the gels immersed in PBS (pH 7.4) was further assessed. As depicted in **Figure 4.3d**, photothermal heating using a laser density of 1 W cm^{-2} (corresponds to a steady-state temperature of 47°C) leads to improved metformin release from the GO/metformin gel, where about 12 μg (12%) of metformin is released per laser activation, while without activation a total amount of 9 μg (9%) is released in the first two hours and then remains constant. The amount of metformin released is comparable to other reports using NIR melting microneedles with metformin release between 12-24%. [275, 278]

4.3. Metformin hydrogels using reduced graphene oxide (rGO-COOH) as a cross-linker

We were intrigued if replacing highly oxidized GO, with known suboptimal absorption of NIR light, with reduced GO (rGO) would allow to optimize metformin release. Partial restoration of the aromatic network in rGO affords a significant increase in NIR absorbance and rGO has become of particular interest as a highly effective photothermal agent.[284] However, as can be seen in **Figure 4.4**, the crosslinking properties of rGO with metformin are too weak due to absence of hydroxyl and carboxylic functions on rGO needed for hydrogen bonding formation and decreased electrostatic interactions with metformin (**Figure 4.3c**) at more acidic pH.

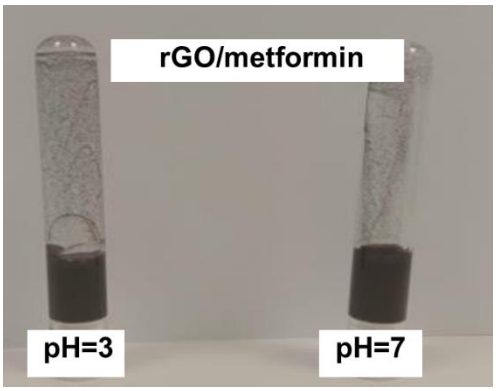

Figure 4.4. rGO/metformin gel formation as a function of solution pH.

Therefore, to enrich rGO with carboxylic acid groups, we synthesized water dispersible rGO-COOH. The synthetic procedure is based on the reaction of GO with chloroacetic acid under strong basic conditions (**Figure 4.5a**).[285] Furthermore, by performing the carboxylation reaction at elevated temperature, a partial reduction of GO was achieved, as evidenced by the increased absorption tail in the NIR region of the UV-Vis spectrum (**Figure 4.5b**). XPS analysis

confirmed the formation of rGO-COOH/metformin (**Figure 4.5c**) by the presence of 5.3 at % N next to C and O. The high resolution C_{1s} spectrum of rGO-COOH/metformin shows bands at 284.6, 286.6, 288.5 and 292.7 eV corresponding to C-C, C-O/C-N, C=O and O-C=O (**Figure 4.5d**).

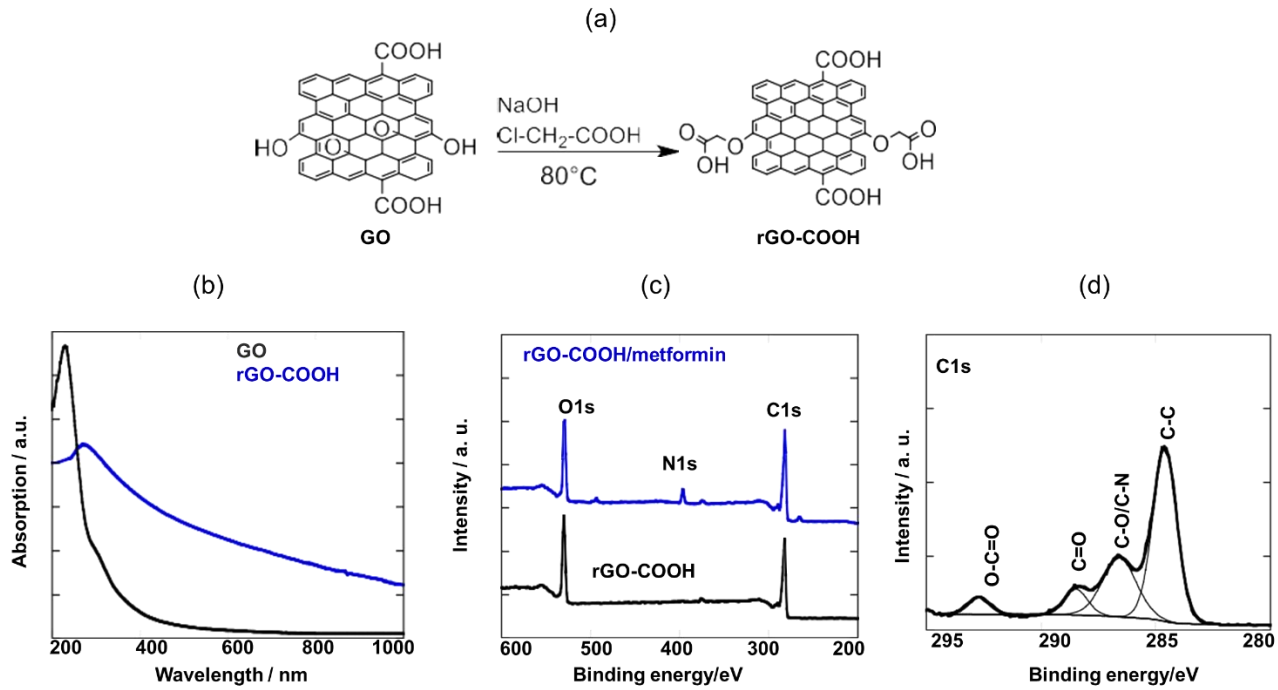

Figure 4.5. (**a**) Synthetic procedure for the preparation of rGO-COOH. (**b**) UV-Vis spectrum of GO and rGO-COOH. (**c**) XPS survey spectrum for rGO-COOH (black) and rGO-COOH/metformin (blue). (**d**) C_{1s} high resolution XPS spectrum of rGO-COOH/metformin.

The gelling process of rGO-COOH with metformin is also pH dependent with stable gels obtained at pH< 7 (**Figure 4.6a**). The formed gel has a porous structure with an average pore size of 25 ±10 nm (**Figure 4.6b**), somehow larger than that of GO/metformin. Using rGO-COOH as a cross-linker rather than GO significantly improves the photothermal properties of the rGO-COOH/metformin gel (**Figure 4.6c**) due to favorable light-matter interaction of rGO-COOH, showing stronger absorption in the near infrared compared to GO (**Figure 4.5b**).

The better heating ability of rGO-COOH results in an increased metformin release from the gel upon laser activation at 1 W cm^{-2} (corresponding to a steady-state temperature of 61°C) where about 25 µg (21%) of metformin is released per laser activation (resulting in a total of 75 µg for 3 laser activation cycles of 10 min each). Passive release is increased due to the larger pore size attaining a total amount of 11 µg (11%) in the first two hours and then remains constant (**Figure 4.6d**).

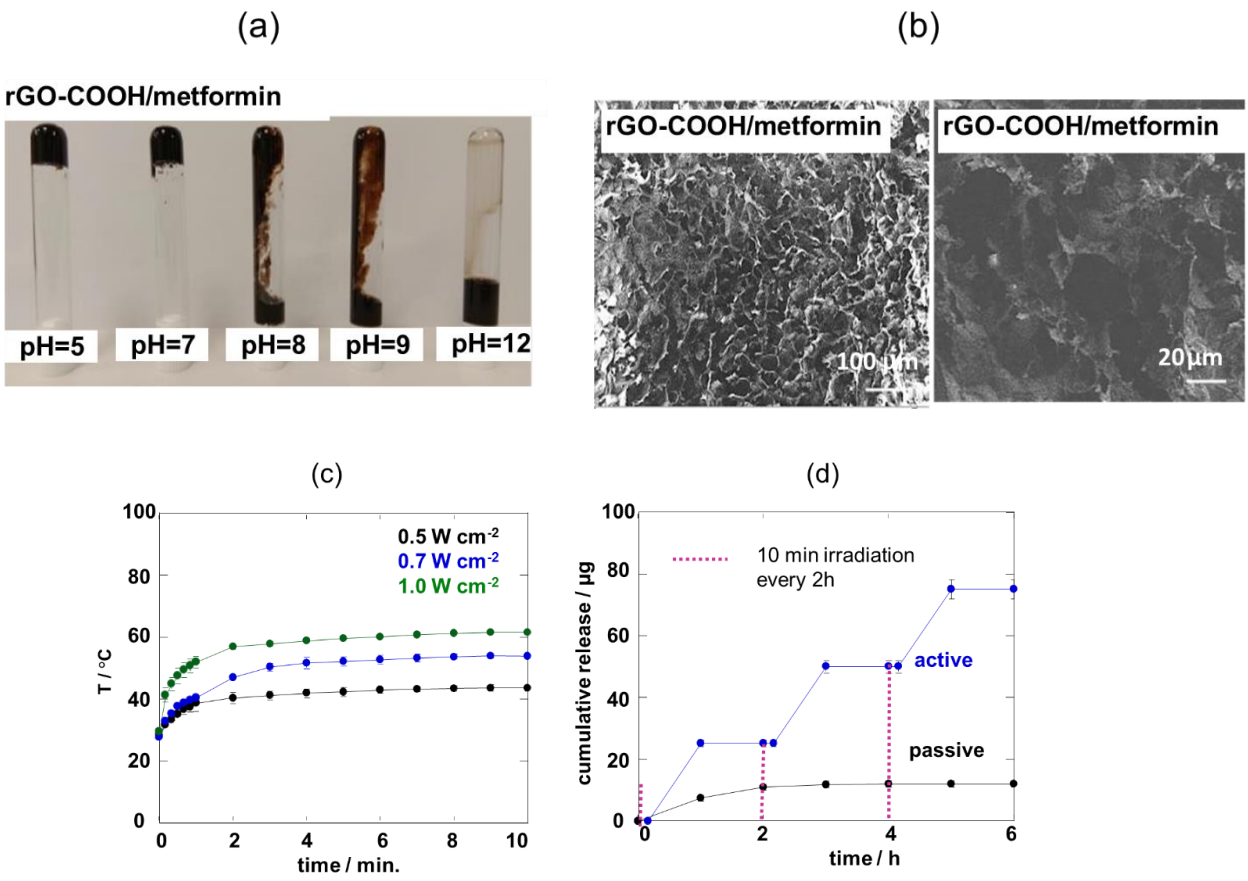

Figure 4.6. (**a**) Photographs of rGO-COOH/metformin gels at different pH. (**b**) SEM images of a rGO-COOH/metformin gel. (**c**) Change of temperature upon laser irradiation at 980 nm at 0.5, 0.7 and 1.0 W cm^{-2} laser power for 10 min. (**d**) Metformin release from a rGO-COOH/metformin gel into PBS (pH 7.4) upon photothermal irradiation of the GO/metformin gel at 980 nm (10 min at 1 W cm^{-2} every 2h) in comparison to passive release.

4.4. NIR light triggered transdermal metformin release

The rGO-COOH/metformin heatable hydrogel is further implemented in *ex vivo* transdermal drug delivery studies using mice skin in Franz diffusion cells. **Figure 4.7a** represents the cumulative permeation profile of metformin from rGO-COOH/metformin gels (500 µg) passively and under the impact of one-time NIR laser irradiation at 1 W cm^{-2} (corresponding to about 61 °C) and at 0.7 W cm^{-2} (corresponding to about 54 °C). After 6 h permeation, 80±8 µg cm^{-2} (16% of total patch as determined by HPLC, 1 W cm^{-2}) and 56±5µg cm^{-2} (12%, 0.7 W cm^{-2}) metformin had diffused through the skin. The combined metformin delivery for a day is 319±8 µg cm^{-2} (64%, 1 W cm^{-2}) and 222±10 µg cm^{-2} (45%, 0.7 W cm^{-2}). The passive release after 24 h corresponds to 50±5 µg cm^{-2} (10%). The efficiency of thermal- induced transdermal metformin delivery of rGO-COOH/metformin gel is competitive with the hydrogel microneedles reported recently by Migdadi et al., reaching a release percentage of 12.94±2.96%

and 37.53±3.17% after 6 and 24 h, respectively.[277] About 5-30 µg (5-6%) of metformin was further found to be trapped in the skin (**Figure 4.7b**).

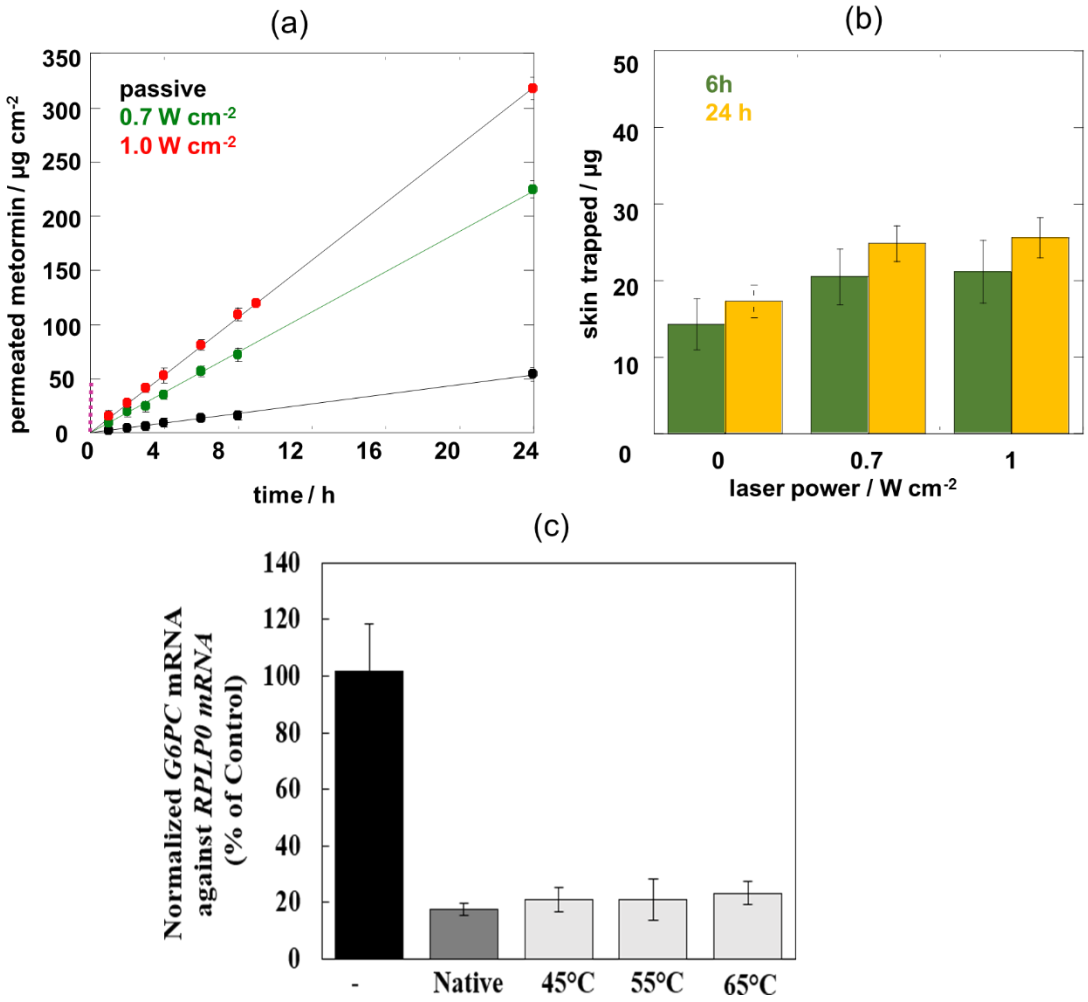

Figure 4.7. *Ex vivo* permeation profiles of metformin assessed using Franz diffusion cell: (**a**) rGO-COOH/metformin gel of 500 µg metformin activated one time for 10 min at 0.7 W cm^{-2} (green) or 1.0 W cm^{-2} (red) as well as without activation (black); (**b**) Amount of metformin trapped in the skin; (**c**) *The Glucose 6 Phosphatase Catalytic (G6PC)* mRNA level of human IHH hepatocyte cells exposed to heated (45, 55 and 65 °C) and native metformin for 24 h. The G6PC mRNA was normalized against the RPLP0 mRNA. Similar result was found upon normalization against *TBP* mRNA. The expression levels from untreated cells (-, Control) were set to 100%. Data are the mean ± SEM of three independent experiments made in triplicates. To ensure that NIR laser irradiation did not alter the activity of metformin, G6PC mRNA in human IHH hepatocytes cells exposed to metformin photothermally heated at 45 °C, 55 °C and 65 °C, which approximately correspond to 0.5, 0.7 and 1.0 W cm^{-2}, was measured. Reduction of the G6PC expression in hepatocytes, leading to diminished gluconeogenesis, partly accounts

for the improved insulin sensitivity and the antidiabetic effect of metformin. [281] As previously observed, exposure of IHH cells to native metformin results in drastic reduction of the G6PC expression (**Figure 4.7c**). The effect of metformin heated at 45 °C, 55 °C and 65 °C on the decrease of G6PC mRNA level was comparable to that of caused by native metformin (**Figure 4.7c**), indicating that the laser irradiation enabling the transdermal metformin delivery does not affect the drug activity.

4.5. Influence of temperature on skin structure

The thermal damage to the skin tissue was further evaluated. When skin is exposed to temperatures above the physiological temperature over an extended period of time, skin tissue damage can occur.[286] It has been recently demonstrated that heating rGO loaded hydrogels in contact with a skin at a laser power density of up to 5 W cm^{-2} did not induce any significant histological changes to the skin.[261] **Figure 4.8** shows the histological analysis of human skin in contact with rGO-COOH/metformin gel before and after laser irradiation (10 min, 0.5-1.0 W cm^{-2}) using conventional hemotoxylin and eosin (H&E) staining. At a laser power density up to 0.7 W cm^{-2} (corresponding to 52°C) normal dermis characteristics are observed. The epidermis as well as the dermis are unaffected. These results are in agreement with reports by others using Cu_7S_4 loaded microneedles, where tissue necrosis in the dermis could be visualized after NIR irradiation for 3 min and 1 min, respectively. [287] Application of ≥ 1 W cm^{-2} laser power results however in skin damage.

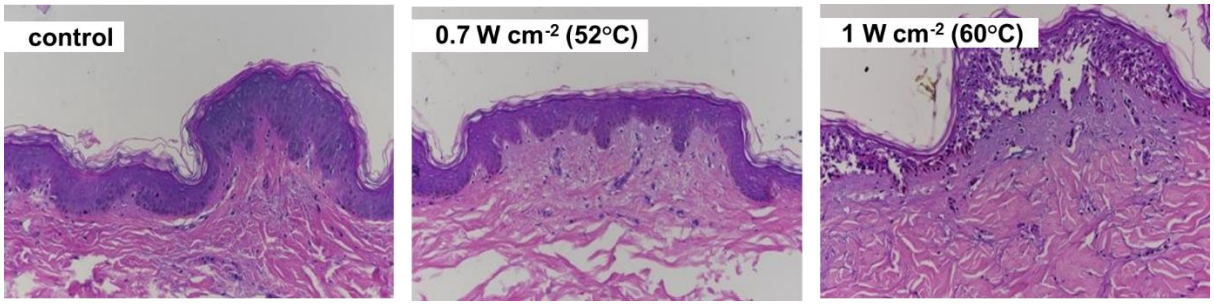

Figure 4.8. Bright-field micrograph of histological section of an *ex vivo* human skin model before (control) and after 10 min laser irradiation at 0.7 W cm^{-2} and 1 W cm^{-2}.

4.6. *In vivo* studies

Animals were separated into four groups. In the negative control group animals received carboxymethylcellulose (CMC) (0.5%) via oral gavage. The second groups received CMC (0.5%)/metformin (**Figure 4.9**) orally in the same manner as the negative group. The third group was composed of animals where metformin (200 mg/kg) was subcutaneously injected. These results were compared to the fourth group treated with rGO-COOH/metformin gels (1 g metformin loading) and being activated for 10 min at 0.7 W cm^{-2}. As seen from the plasma profile in **Figure 4.9**, a maximal concentration was detected after 30 min when administered orally and under subcutaneous injection. Using the metformin based rGO/COOH patch for the delivery of metformin via photothermal activation for 10 min, a maximal plasma concentration was detected after 1h activation where a concentration of 13±2 µg mL^{-1} was detected, in line with other reports.[277] It decreased thereafter slowly until the 2 h endpoint.

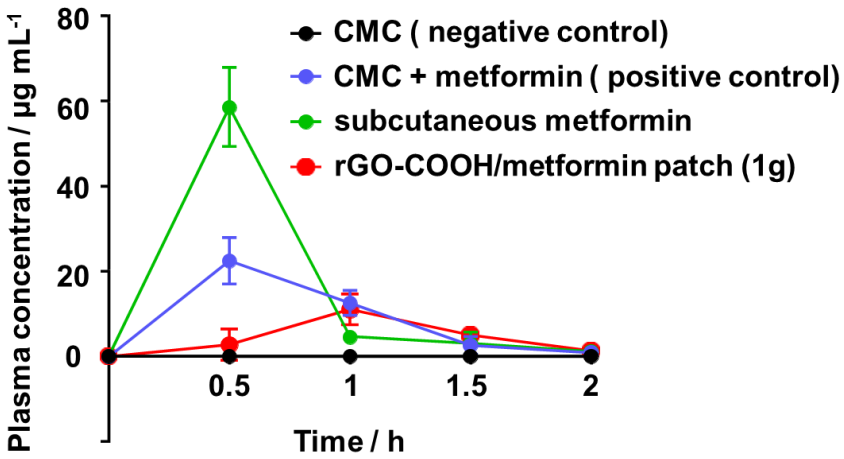

Figure 4.9. *In vivo* plasma profiles of metformin following oral administration with only CMC (black) or CMC+metformin (blue), subcutaneous metformin injection (green) and following application of the rGO/metformin gel and activation for 10 min at 0.7 W cm^{-2}. n=3 per group

4.7. Conclusion

In this chapter, we presented a novel formulation of a metformin releasing hydrogel based on a simple and straightforward mixing of carboxyl enriched reduced graphene oxide (rGO-COOH) with metformin hydrochloride. Delivery of the antidiabetic drug was achieved by weakening the gelation forces through photothermal heating. The proposed delivery system could release metformin in an intermittent cycle administration with near-infrared light on/off cycles, which increased release in the laser on state. Using mice skin as *ex vivo* model in Franz diffusion cells, these supramolecular drug reservoirs could deliver transdermally 319±8 μg cm^{-2} (64%, 1 W cm^{-2}) and 222±10 μg cm^{-2} (45%, 0.7 W cm^{-2}) in a day, with about 5-30 μg (5-6 %) of metformin being trapped in the skin. In vitro assessment of the key target Glucose-6 Phosphatase (G6P) gene expression using Human hepatocyte model confirmed further that the biological activity of metformin remained unaffected by photothermal activation. *In vivo* studies indicated in addition the rise in metformin plasma level, 1h after patch activation.

CHAPTER 5

Carbon nanostructures for islet amyloid desintegration

5.1. Introduction

Human islet amyloid polypeptide (hIAPP) also called as amylin is a hormone co-expressed and co-secreted with insulin in pancreatic β-cells in a ratio between 1:10 and 1:100 (hIAPP:insulin). [288] hIAPP plays a key role in glucose homeostasis. hIAPP helps the anabolic effect of insulin by strongly inhibiting the glucagon secretion. In addition, it controls adiposity and triggers in brain an inhibitory effect in satiety .[289] In most patients with diabetes, hIAPP is structurally modified by several factors including hyperglycemia. hIAPP aggregates from its non-toxic native monomers to cytotoxic oligomers. hIAPP oligomers contribute to β-cell death and thereby, to β-cell mass reduction in T2D and the progression of the disease towards complications. [290-291] Moreover, it has been shown that hIAPP can reach the brain, in which it interacts with β-amyloid (Aβ) aggregates for forming various heterocomplex fibrils and oligomers.[292] These complexes might not only account for the development of Alzheimer disease, but might also be responsible for the destruction of pancreatic β-cells in T2D [293-294].

Inhibition of hIAPP oligomers and complexes formed with Aβ is suggested as a therapeutic strategy for improving β-cell survival and slowing the progression of diabetes towards complications. [295] In recent years, several inhibitors preventing the formation of amylin β-sheets and the aggregation of the peptide together with destabilization of fibril have been synthetized [296-302]. The first inhibitors were short peptides and small molecules with high affinity and specificity for amylin.[297, 303] Next, nanoparticles-based inhibitors have been developed. [304-306]Indeed, it is known that the interactions between carbon nanoparticles and peptides are dominated not only by hydrophobic and π–π stacking interactions, but also by the surface curvature. Numerical computation of tetramer and octamer hIAPP with or without diverse carbon nanoparticles such as graphene, single-wall carbon nanotubes (SWCNTs) and fullerene C60 revealed that peptides can be strongly adsorbed onto graphene and SWCNTs, while C60 prevents aggregation to a lesser extent. [307] Experimentally, various GO nanosheets and graphene quantum dots (GQDs) have been widely described for inhibiting the formation of hIAPP fibrils in water. [308]

In this chapter, we investigate the possibility of carbon quantum dots (CQDs) to disintegrate amylin aggregates formed under physiological conditions using thioflavin T assay (ThT). In addition, first promising results about co-oligomerization of hIAPP with β-amyloid will be presented.

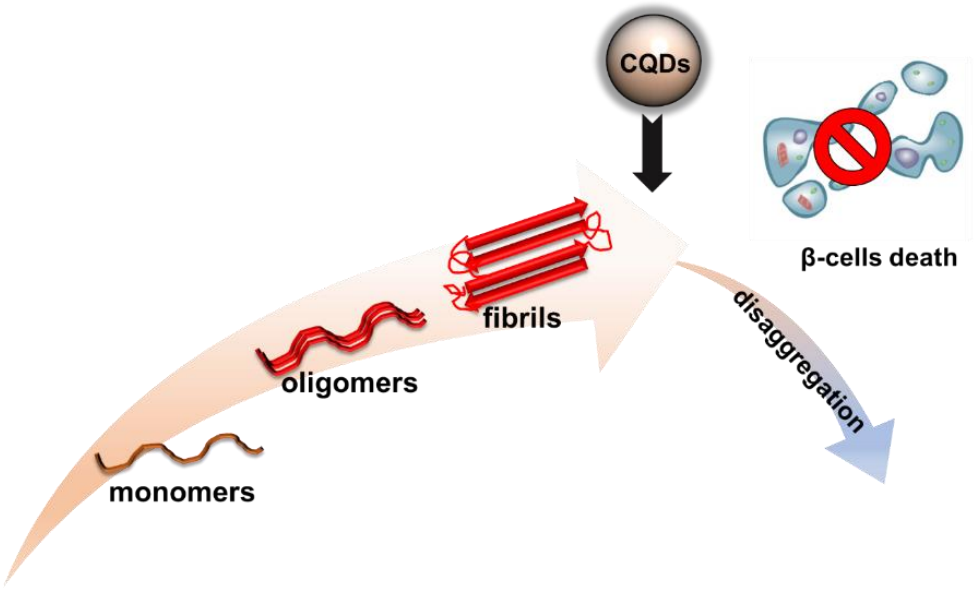

Figure 5.1. Schematic representation of amylin aggregation and its disintegration after carbon quantum dots (CQDs) treatment.

5.2. Carbon quantum dots synthesis and characterization

For producing functionalized CQDs from different organic precursors, high temperature conditions in a close Teflon-line reactor named hydrothermal synthesis is mostly used. [309] It has the advantage in terms of high fluorescence of produced CQDs, but on the other hand, it is time consuming and lacks of reproducibility. To overcome these limitations, microwave-assisted synthesis of CQDs can be performed.[310-311] This rapid, homogeneous, temperature and pressure controlled method leads to the formation of quantum dots with uniform size distribution.[312] Hence, microwave-assisted method was used for preparation of 3 types of carbon dots: carboxylic acid-modified CQDs (CQD-1) from glucosamine as a precursor and β-alanine as a surface passivating agent, aminated CQDs (CQD-2) from the same precursor but passivated agent was changed to ethylenediamine and fluorinated CQDs (CQD-3) mixing glucose and hydrofluoric acid to catalyse dehydration reaction (**Figure 5.2**). To remove larger precipitates, the CQDs suspension was centrifuged and then dialyzed against water with a final yield of 0.8%, 3.4% and 2.5 % for CQD-1, CQD-2 and CQD-3 respectively. Transmission electron microscopy (TEM) images (**Figure 5.2 (a)-(c)**) showed that the CQDs were almost spherical with an average particle size of ≈26, ≈19 and ≈22 nm

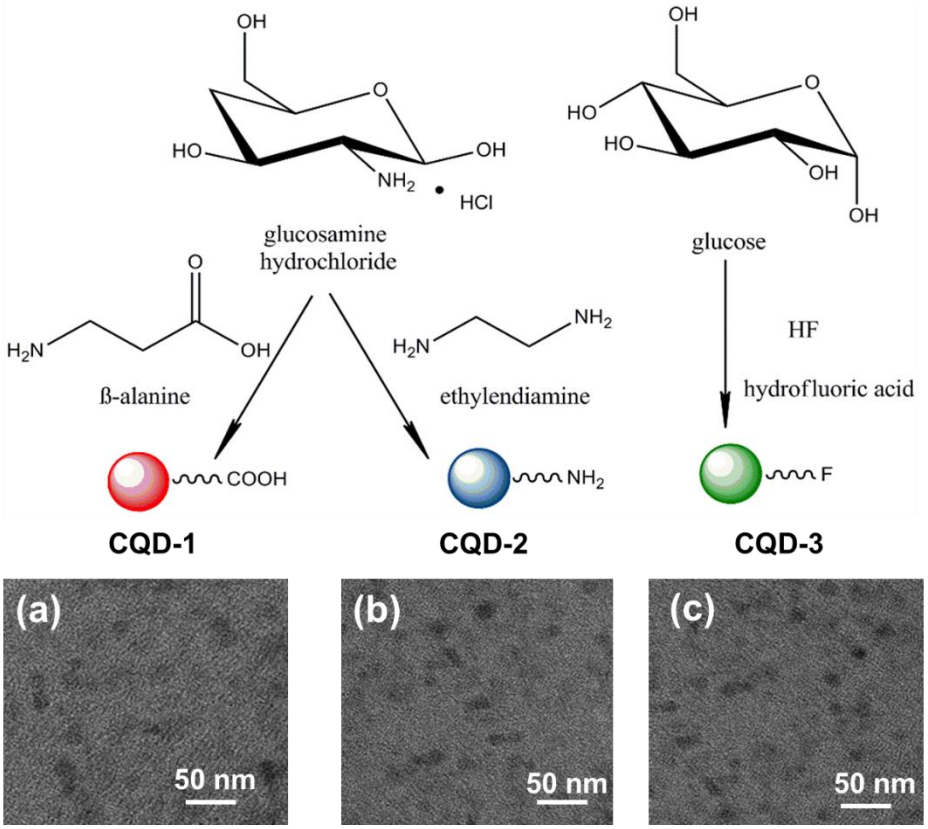

Figure 5.2. Schematic representation of carbon quantum dots synthesis and their TEM images CQDs-1 (a) ,CQDs-2 (b) and CQDs-3 (c) respectively.

The chemical composition of the carbon dots was assessed by X-ray photoelectron spectroscopy The C_{1s} high resolution XPS spectra of the CQDs depict different carbon features (**Figure 5.3a**). In the case of CQD-1, the high-resolution spectrum of the C_{1s} reveals the presence of fives peaks corresponding to C=C (283.8 eV), C–C/C–H (285.0 eV), C–N/C–O (286.8 eV), C=O (287.9 eV) and –O–CQO (289.2 eV). The presence of carbonyl and carboxylic functions is additionally validated by the presence of a band at 530.7 eV (C=O) in the O_{1s} high resolution spectrum, next to 531.5 eV (C–O). The N_{1s} high resolution spectrum can be curve-fitted with bands at 398.3 eV (pyridinic C=N–C), 399.1 eV (pyrrolic N–H) and 400.3 eV (graphite-like structure N–C3). For the CQD-2 (**Figure 5.3b**), the deconvoluted spectrum of C_{1s} assigned fives peaks: C=C (283.8 eV), C–C/C–H (285.0 eV), C–N/C–O (286.2 eV), C=O (287.2 eV) and –O–C=O (288.3 eV). The band at 530.1 eV (C=O) with the band 531.6 eV (C–O) in the O_{1s} high resolution spectrum verified the presence of oxygen functions. The N_{1s} high resolution spectrum shows comparable bands as CQD-1: 398.3 eV (pyridinic C=N–C), 399.2 eV (pyrrolic N–H) and 400.9 eV (graphite-like structure N–C3).

In case of CQD-3 (**Figure 5.3b**) the high-resolution spectrum of the C_{1s} indicated the presence of four peaks corresponding to C=C (284.2 eV), C–C/C–H (285.9 eV), –O–C=O (289.0 eV) and C–F (290.1 eV). The F_{1s} high resolution spectrum was fitted with the band at 685.2 eV. The oxygen content in the CQD-1 and CQD-2 was determined to be 22.8 at% and 14.4 at%, respectively. Higher nitrogen content (13.7 at%) was found in CQD-2 in comparison with CQD-1 (5.7 at%). The fluorine content in CQD-3 was found as 3.9 at%.

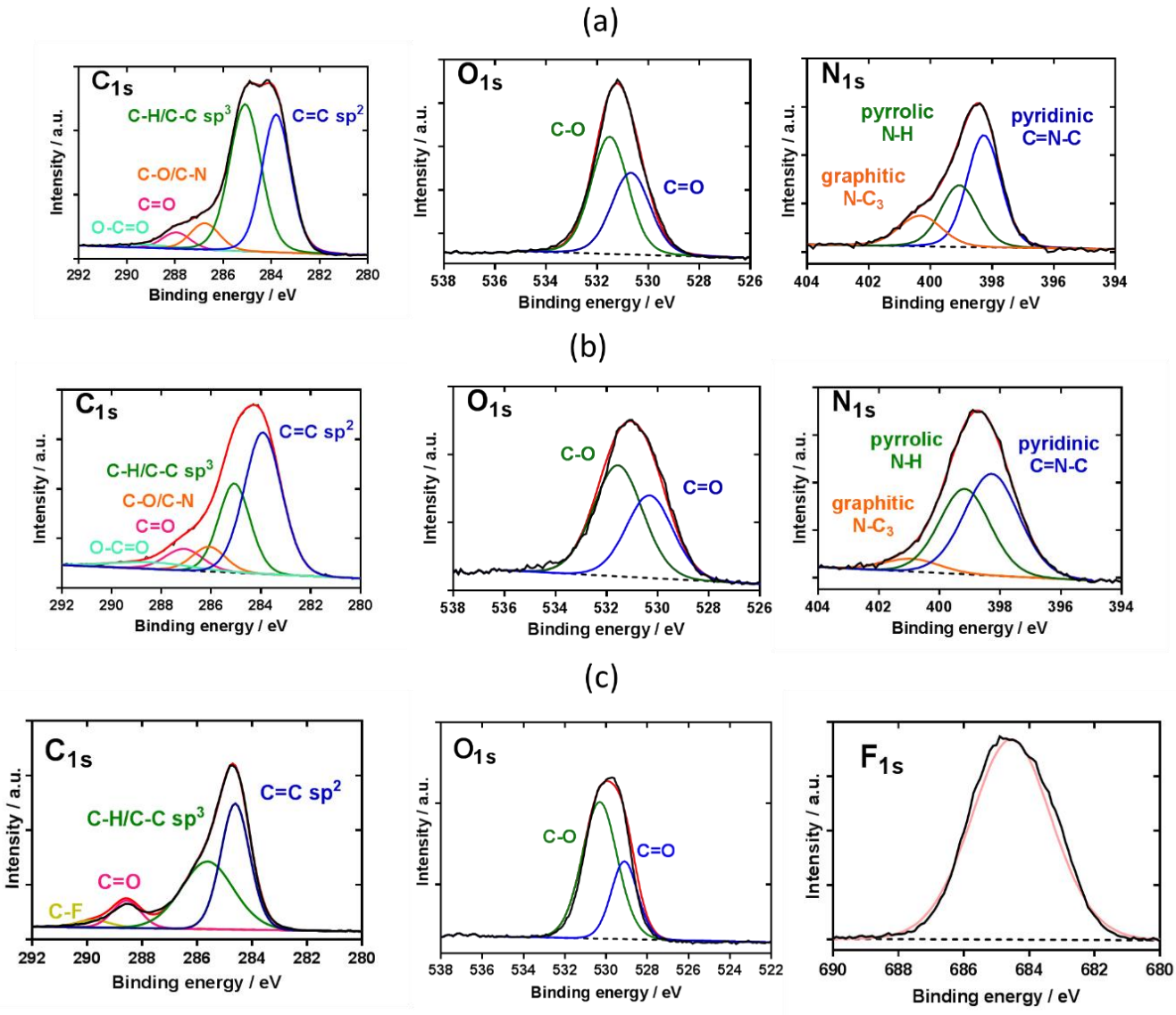

Figure 5.3. (**a**) XPS analysis of CQD-1: C_{1s}, O_{1s} and N_{1s}. (**b**) XPS analysis of CQD-2: C_{1s}, O_{1s} and N_{1s}. (**c**) XPS analysis of CQD-1: C_{1s}, O_{1s} and F_{1s}.

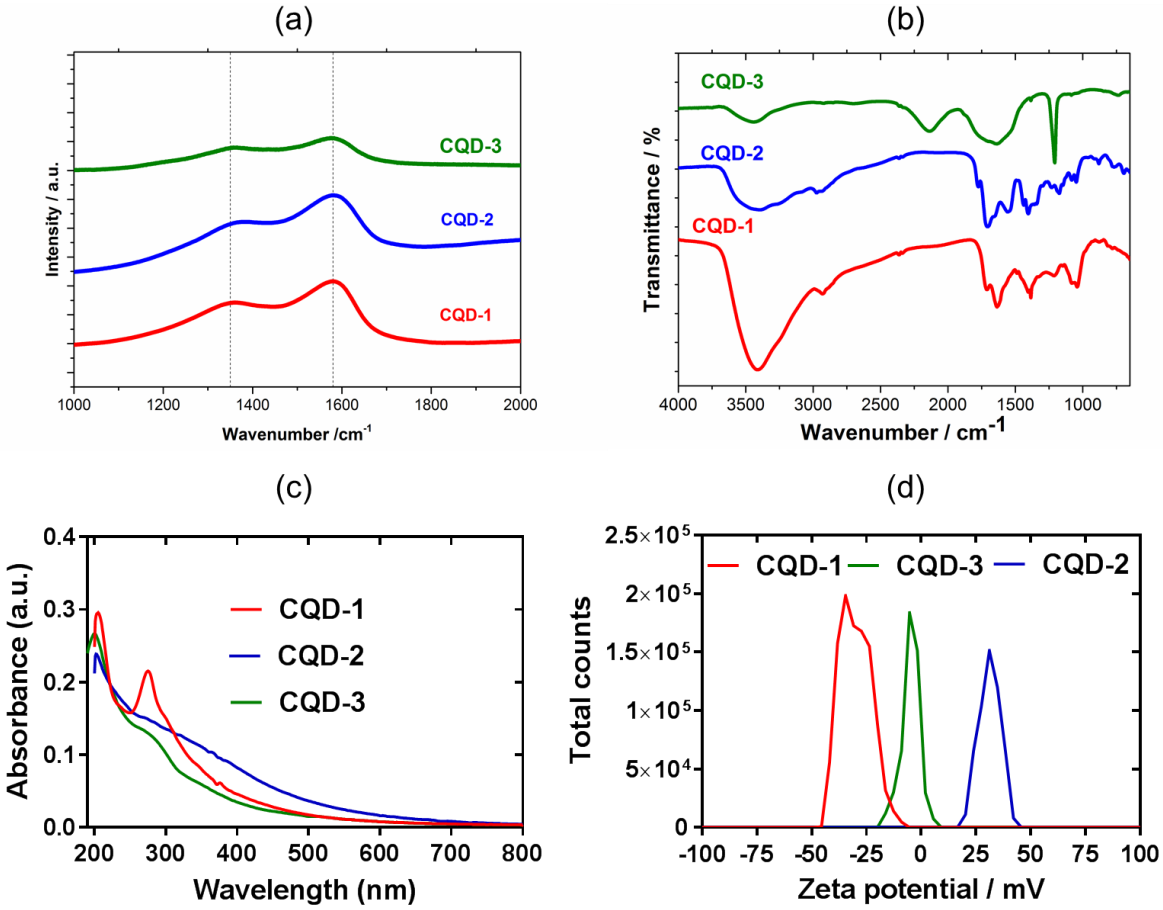

Figure 5.4. (**a**) Raman spectra of CQD-1, CQDs-2 and CQD-3. (**b**) FT-IR spectra of CQD-1, CQD-2 and CQD-3. (**c**) UV-Vis spectra of CQD-1, CQD-2 and CQD-3 at 20 μg mL^{-1} in PBS (pH 7.4, 0.01 M). (**d**) Zeta potential analysis of CQD-1, CQD-2 and CQD-3. Red, blue and green lines correspond to CQD-1, CQDs-2 and CQD-3 respectively.

Typical Raman spectra of CQD-1, CQD-2 and CQD-3 are presented in **Figure 5.4a**. The observed peaks are typical of sp^2 carbon materials at 1580 cm^{-1} (G-band) and 1378 cm^{-1} (D band), indicating that the material is graphitic in nature. The ID/IG ratio were 1.94, 1.56 and 1.32 corresponding to CQD-1, CQD-2 and CQD-3 respectively suggesting large surface disorder and amorphous nature.[313]

Bonding composition and functional groups of synthesized CQDs was further investigated by Fourier transform infrared (FT-IR) spectroscopy (**Figure 5.4b**). The FTIR spectrum of CQD-2 contains a broad band between 3410–3420 cm^{-1} attributed to the O–H/N–H stretching vibrations, while the C–H stretching and bending vibrations are located at 2932 and at 1384 cm^{-1}, respectively. The band at 1636 cm^{-1} is due to C=N and C=C bonds of the aromatic structure, and C=O stretching vibration (–NHCO–). Compared to CQD-2, the more intense peaks at 1083

and 1041 cm^{-1} in the FTIR spectrum of CQD-1 are associated with C–O stretching of either the residual carbohydrate or β-alanine. The sharp peak at 1710 cm^{-1} is assigned to the asymmetric stretching vibration of carboxylic acid moieties.[314] In case of CQD-3, a sharp peak at 1100 cm^{-1} corresponds to stretching vibrations of C−F, indicating the doping of quantum dots with fluorine. [315]

The CQDs absorb in the short-wavelength region with a maximum at around 220 nm due to p–p* transition of C=C and C=N carbon cores with a weak extending tail in the visible region (**Figure 5.4a**). An additional shoulder at approximatively 280 nm is attributed to p–p* transition of different sp2 domains.[316] The absorption shoulder at around 306 nm in CQD-1 is due to n–p* transitions of C=O. This contribution is decreased in CQD-2 due to the high content of ethylenediamine;[317] the strong absorption extending from 350 to 600 nm is related to surface passivation of CQDs-2 with ethylenediamine. The peak at 199 nm of CQD-3 testifies that the carbon dotes were doped with fluorine. [318]

The surface charge of carbon quantum dots can be seen from zeta potential distribution curves in **Figure 5.4d**. CQD-1 displays a negative zeta potential value (ζ = -24.0 ± 1.6 mV) in pure Milli-Q water. The negative surface charge confirms the functionalization of carbon dots with carboxylic groups. Whilst, a positive surface charge ζ = +32.5 ± 0.8 mV of CQD-2 underlines the presence of NH_3^+ groups. CQD-3 showed slightly negative charge ζ = -7.2 ± 2.4 mV due to the presence of fluorine on the surface.

The cytotoxic effect of CQD-1, CQD-2 and CQD-3 was check on the rat insulinoma (INS-1)[319] and mouse insulinoma (MIN-6)[320] cell lines using resazurin assay as described above. 1, 10 and 100 μg mL^{-1} of carbon quantum dots were applied to cells and incubated for 24 hours in order to check their viability. **Figure 5.5** depicts the viability results for INS-1 (a) and MIN-6 (b) cell lines. As it can be seen, there was no cytotoxic effect of carbon quantum dots at 1 and 10 μg mL^{-1} of CQD-1, CQD-2 and CQD-3, while increasing the concentration of quantum dots to 100 μg mL^{-1} in case of MIN-6 cell line, slightly reduce cell viability.

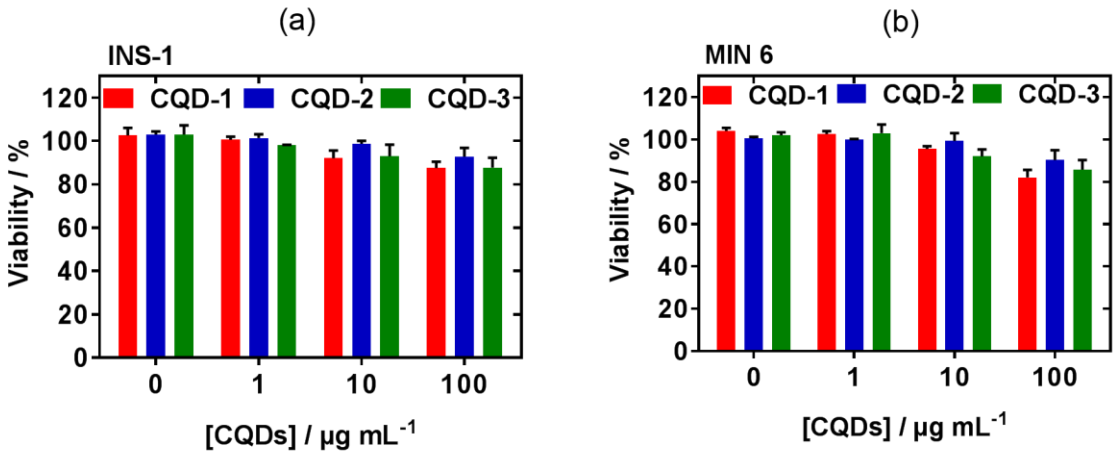

Figure 5.5. Cell viability of INS-1 cells (**a**) and MIN 6 cells (**b**) in the presence of carbon quantum dots CQD-1 (red), CQD-2 (blue) and CQD-3 (green) at different concentrations. Negative control: without CQDs.

5.3. Formation of hIAPP aggregates and an effect of carbon quantum dots on its disaggregation

According to a sigmoidal shape of hIAPP growth curve, the aggregation process can be divided into three phases: lag phase, elongation phase and saturation phase. The ThT fluorescence assay allows to easily differentiate them by variation in intensity of fluorescence. First few minutes correspond to a lag phase, when the fibrils are still not formed. During this time monomers undergo conformational rearrangement leading to formation of clusters that induce fibrillation. This step is considered as a critical and rate limiting. [321-323] Rapid increase in ThT fluorescence corresponds to an elongation phase which finally rapidly reaches to equilibrium**. Figure 5.6 (a-c)** depicts the aggregation profile of hIAPP following the addition of carbon quantum dots. 20 μM of hIAPP was first let to form aggregates for 6 hours and then the CQD-1 (**Figure 5.6a**), CQD-2 (**Figure 5.6b**) and CQD-3 (**Figure 5.6c**) at the concentration of 1, 10 and 100 μg mL^{-1} were added in order to affect the aggregation. We determined that CQD-1, CQD-2 and CQD-3 showed similar profile in hIAPP disaggregation. As expected, higher concentration of CQDs at 100 μg mL^{-1} dropped the intensity of fluorescence dramatically, while 10 μg mL^{-1} showed moderate decrease. Almost no effect was found, when 1 μg mL^{-1} of CQDs were added. The ability of CQDs to disintegrate hIAPP aggregated was further confirmed by atomic forced microscopy (AFM). **Figure 5.6d** exhibits the formation of hIAPP fibrils of diameter ≈100 nm. The AFM image of hIAPP fibers in the presence of 100 μg mL^{-1} CQD-2 (**Figure 5.6d**) indicates an inhibition of fibrillation with isolated aggregates.

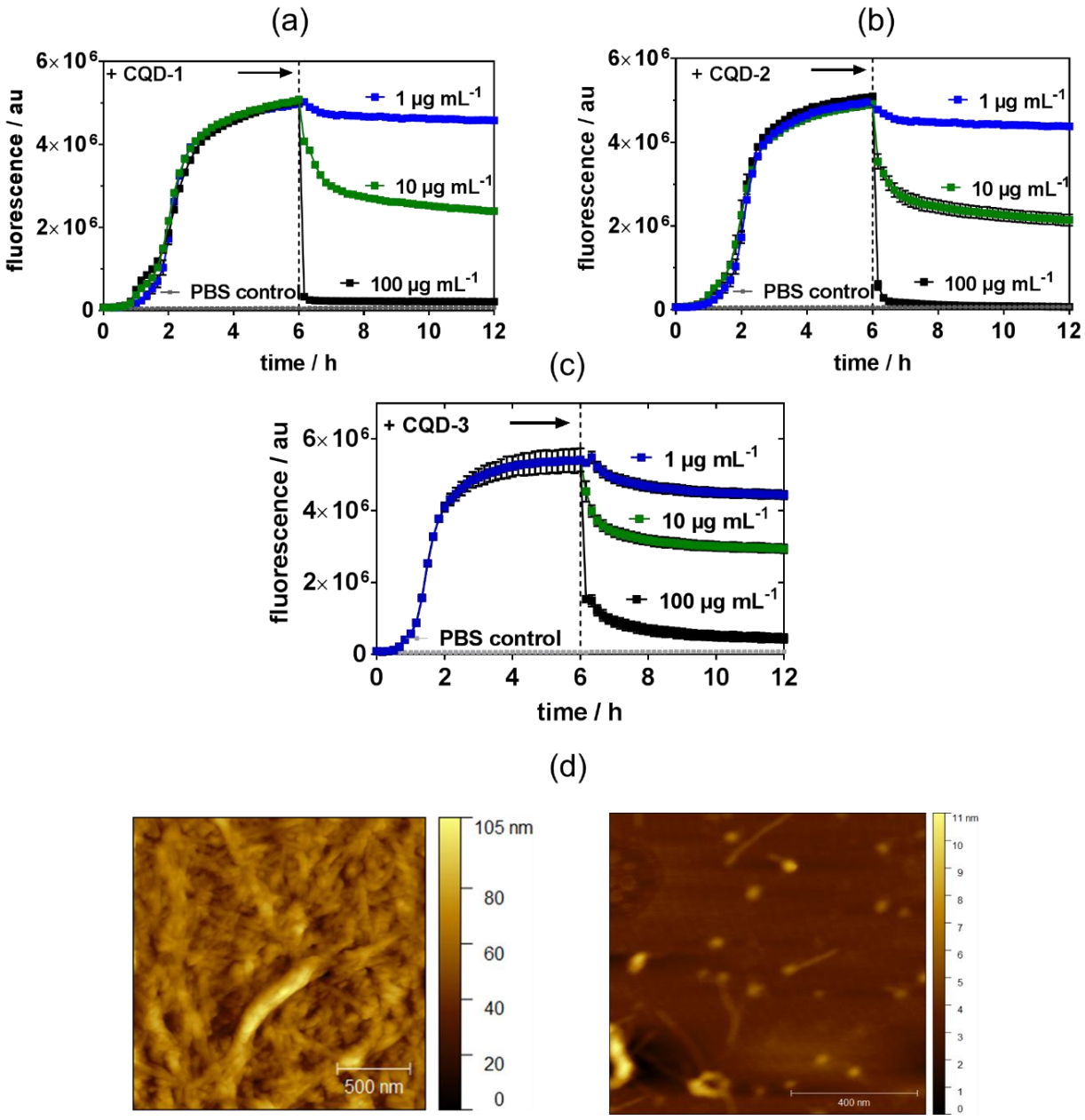

Figure 5.6. Aggregation profiles of hIAPP with addition of CQD-1 (**a**), CQD-2 (**b**) and CQD-3 (**c**). (**d**) AFM images of hIAPP aggregates in the absence and presence of CQDs.

5.4. The role of diabetogenic factors on the human amyloidogenesis process

To investigate the potential effect of glucose on hIAPP aggregation, 20 μM of hIAPP was incubated with 5, 11 and 33 mM glucose at 37°C and physiological conditions [324] **(Figure 5.7a)**.

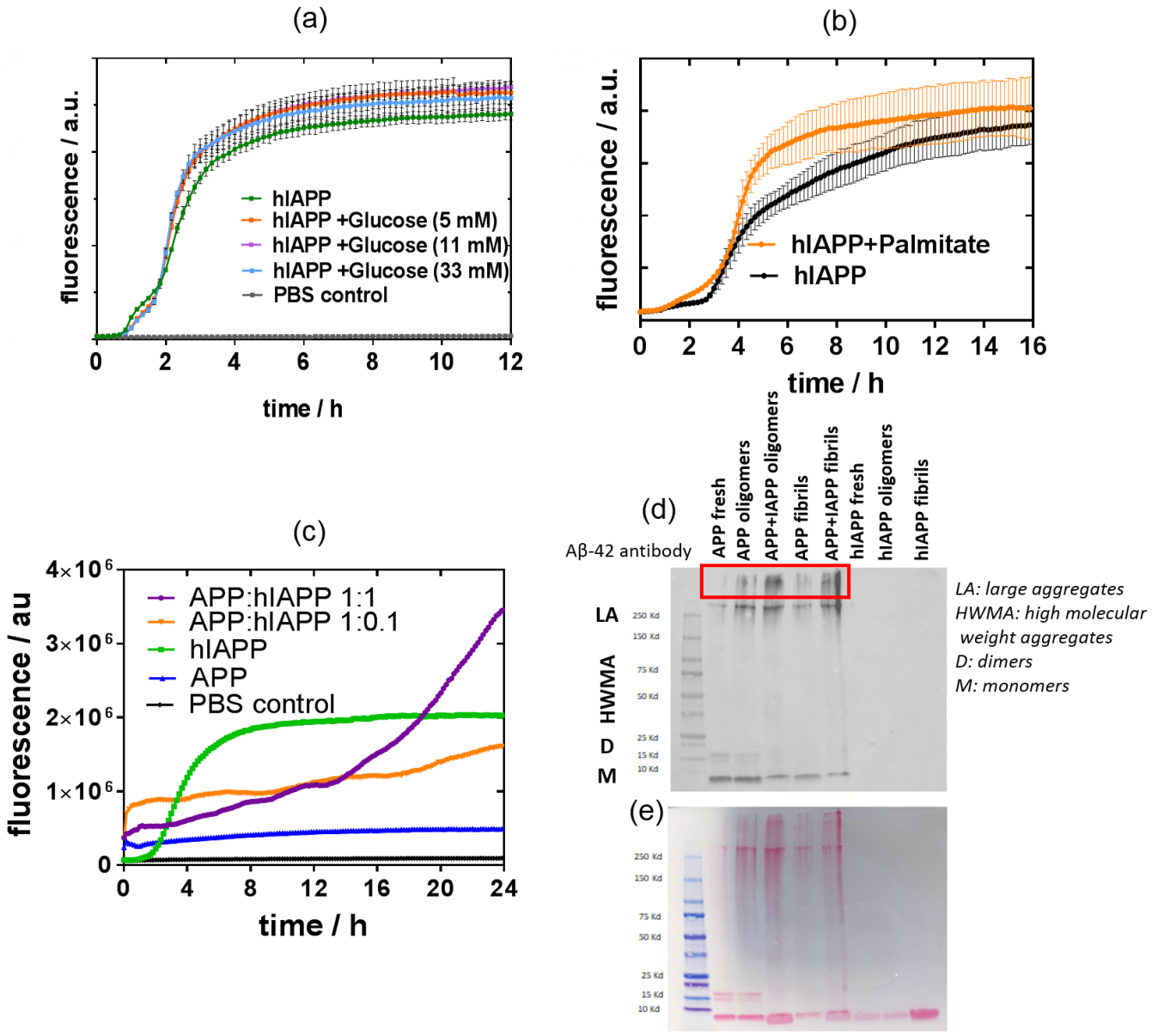

Figure 5.7. (a) Influence of glucose on hIAPP aggregation. **(b)** Effects of palmitate on the fibrillation of hIAPP. **(c)** Aggregation kinetics of β-amyloid from APP (amyloid beta precursor) (20 μM) alone and co-incubated with hIAPP at ratios 1:1 and 1:0.1 (**d**) Western immunoblotting analysis for heterocomplexes of hIAPP:APP (1:1). Oligomers were formed after incubation for 24 h at 4°C while fibrils were formed after incubation for 24 h at 37°C. (**e**) Ponceau S assay for hIAPP and APP heterocomplexes.

The slight increase in fluorescence indicates that more aggregates of hIAPP were formed in the presence of glucose, but no difference in glucose concentration was found. It was previously reported, that lipids can induce high amylin expression. [325-327] Consequently, the next step was to examine an influence of free fatty acid on hIAPP aggregation. For that reason, 20 μM of hIAPP was incubated without and with 125 μM of sodium palmitate. (**Figure 5.7b**). The result suggested that palmitate accelerates hIAPP fibrillation. Previous research investigated the effect of hIAPP on β-amyloid aggregation suggested the high amyloigenic nature of hIAPP can seed the formation of APP aggregates. [328] We next confirmed that co-incubation of hIAPP with APP can promote β-amyloid aggregation. (**Figure 5.7c**). We compared the aggregation profile of freshly prepared hIAPP, APP and co-incubated APP:hIAPP heterocomplexes. This process was also a ratio depended: increasing the ratio between hIAPP and APP from 0.1:1 to 1:1 markerly increased the aggregation rate starting from 16 h of aggregation.

The heterocomplexes formed due to co-incubation of hIAPP and APP were found to be toxic to β-cells. It has been shown that glucose and saturated fatty acid palmitate promote Aβ oligomerization and formation of distinct heterocomplex aggregates with hIAPP in a mechanism that is independent of cell function.[326, 329]

To confirm the changes observed in APP co-incubated with hIAPP aggregation profile, denaturing immunoblotting using antibodies against APP was performed to detect the formation of aggregates (**Figure 5.7a).** 20 μM hIAPP:APP (1:1) mixtures were left overnight at 4°C and 37 °C to form oligomers and fibrils respectively. Oligomerization and fibrillation of APP alone were compared to freshly prepared APP solution. All samples demonstrated an ability to form large aggregates (>250 kDa). Moreover, hIAPP:APP oligomers and fibrils demonstrated an increase in large aggregates formed.

To test a cytotoxicity of aggregates, rat insulinoma (INS-1) and mice insulinoma (MIN-6) cell lines were incubated with hIAPP:APP in diabetogenic conditions. In order to simulate the diabetogenic conditions, in addition to heterocomplexes, cell were exposed to 20 mM glucose, 0.5 mM palmitate and their mixture. As it can be seen from **Figure 5.8a**, the combination of both glucose (20 mM) and palmitate (0.5 mM) causes cell death in the presence of hIAPP:IAPP heterocomplexes. Similar pattern is pesented for MIN-6 cells (**Figure 5.8b**). In this case the cytotoxic effect was analogical to the one described for INS-1 cell line, however it was more pronounced.

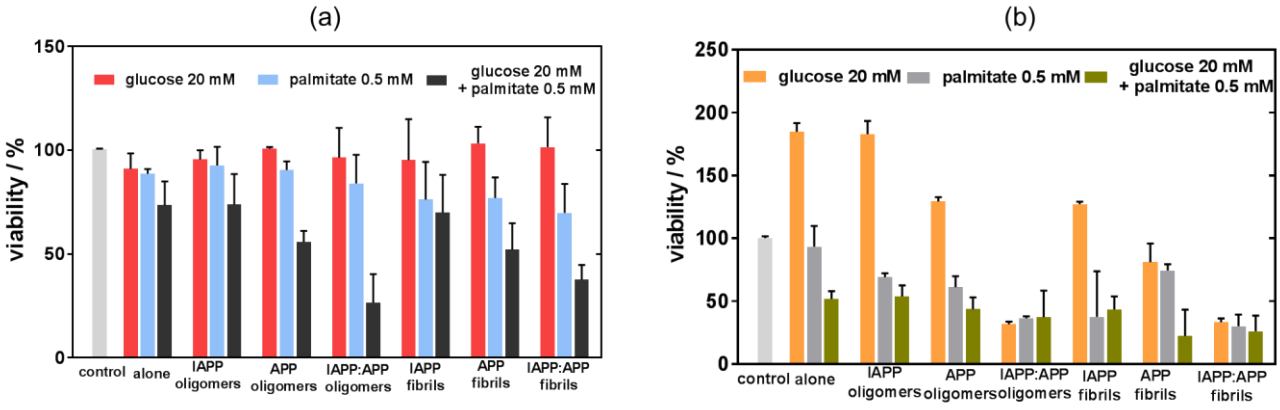

Figure 5.8. (**a**) INS-1 cells viability after incubation of APP:hIAPP heterocomplexes for 48h. (**b**) MIN-6 cells viability after incubation of APP:hIAPP heterocomplexes for 48h.

Conclusion

In this chapter, we demonstrated that 3 types of microwave prepared carbon quantum dots can disintegrated the hIAPP aggregates. The disaggregation was found to be CQDs dependent. In addition, we tested an influence of glucose and palmitate on the aggregation profile, where palmitate showed its effect unlike glucose. Also, aggregation kinetics of APP was effected by addition of hIAPP, which was confirmed by ThT fluorescence assay and Western blotting. The toxicity of formed aggregated was shown using 2 insulinoma cell lines cultured in diabetogenic conditions. The highest toxicity was found for the hIAPP/APP heterocomplexes, supporting the idea that the brain and pancreas amyloidosis might accelerate β-cell destruction in T2D. Future experiments will be to confirm the studies in islets β-cells and to check the inhibition effect of CQDs on aggregation of hIAPP, APP and hIAPP:APP heterocomplexes. Moreover, it would be interesting to investigate the the rescue effects of carbon dots in the harmful effects of APP+hIAPP mixture in the islets cell survival cultured with glucose and palmitate.

CHAPTER 6:

Conclusions and perspectives

As it was discussed in chapter 1, diabetes remains one of the leading diseases causing premature deaths all over the world. This thesis presents different attempts to develop personalized medicine for diabetic patients as well as to find new ways for improving their compliance by using alternative routes of antidiabetic drugs administration. In this respect, the potential of mucoadhesive patches and mucosa lining for delivery of insulin via oral cavity has been made possible via insulin loaded mucoadhesive PAA@rGO fibre mats, which can be activated on-demand via irradiation. Results from *ex vivo* experiments using porcine buccal mucosa suggested that photothermal activation allows to achieve insulin release in sufficient quantity with good penetration through buccal tissue. Considering porcine buccal mucosa being thicker than human one, insulin loaded mucoadhesive PAA@rGO fibre mats are expected to achieve even better on demand delivery of insulin in humans. Next to buccal, different transdermal delivery approaches have been outlined, ranging from insulin loaded polymeric microneedles to metformin hydrogels. Both systems contained photothermal agents such as rGO-COOH or MoS_2 in order to attain on-demand drug release. Released insulin and metformin stayed active and could be found in pigs and mice plasma after delivery.

In addition to finding new drug delivery ways for antidiabetic drugs, the use of carbon quantum dots as disaggregation agent for islet amyloid polypeptide fibrils (IAPP) has been proposed. The perspectives of such studies include experiments in islets of pancreatic cells and investigation of inhibition effect of carbon quantum dots on aggregation of islet amyloid polypeptide, β-amyloid and their mixtures. In addition, it is also essential to investigate the rescue effects of carbon quantum dots in the harmful effects of IAPP and β-amyloid mixture in the islets cell survival cultured with glucose and palmitate.

As cardiovascular diseases (CVD) are considered one of the macrovascular complications caused by diabetes, investigation of transdermal delivery of angiotensin-converting enzyme (ACE) inhibitors is a strategy, which further perspectives in the future using the knowledge obtained on the construction of transdermal bandages. In this respect, ramipril, one of the widely used ACE inhibitor prodrugs orally administered once or twice a day, might be an interesting candidate to pursue. Due to its hydrophobic character, limited solubility in aqueous medium and low biodistribution, large amounts have to be administered to obtain a therapeutic

effect. Ramipril with an octanol/water partition coefficient of 3.32 being only slight above the optimal partition coefficient for transdermal deliver (considered to be between a log P of 1-3) is ideally adapted for the transdermal route. In combination with enhanced delivery modes such as chemical enhancers, nanocarriers and heat, ramipril is considered as a candidate for *in vivo* transdermal administration in hypertension rats.

APPENDIX

S1. Chemicals

Metformin hydrochloride, hydrazine hydrate ($NH_2NH_2•H_2O$), chloroacetic acid ($Cl-CH_2COOH$), acetonitrile, potassium dihydrogen phosphate buffer (pH 6), sodium dodecyl sulfate (SDS), dexamethasone, polyacrylic acid (PAA, Mn 450 000 g mol^{-1}), β-cyclodextrin, artificial saliva solution, recombinant insulin, FITC-labeled insulin, phosphate-buffered saline (PBS 1X, pH 7.4), sodium hydroxide (NaOH), sodium chloride (NaCl), glucose, hydrofluoric acid (HF), Spectra/Por 3 dialysis tubing, formic acid (FA), carboxymethylcellulose (CMC), acetonitrile (ACN), hydrochloric acid (HCl), potassium bromide (KBr), Irgacure 2959, paraformaldehyde, gelatin, methacrylic anhydride (MA), polydimethylsiloxane (PDMS), thioflavin T (ThT), 1,1,1,3,3,3-Hexafluoro-2-propanol (HFIP), poly(ethylene glycol) diacrylate (PEGDA, average MW~700 g mol^{-1}), molybdenum(IV) sulfide (MoS_2), Dulbecco's modified Eagles medium (DMEM, Gibco®), fetal bovine serum (FBS, Gibco®), penicillin-streptomycin (Gibco®), RPMI 1640 Medium, Williams E medium, dexamethasone, sodium pyruvate, β-mercaptoethanol, sodium palmitate, resazurin, Mayer's hematoxylin solution, Y-eosin solution, ramipril, Thermofisher or Fisher Scientific.

Reduced graphene oxide (rGO) in powder form was purchased from Graphenea (Spain). Graphene oxide (GO) was purchased from Graphitene (UK).

RNeasy Lipid Tissue Kit was purchased from Qiagen, Germany. Isoflurane was obtained from Aerrane; Baxter, France.

Human skin for *ex vivo* experiments was provided by HypoSkin®, Genoskin SAS, Toulouse, France.

Clarity Western Peroxide Reagent, Clarity Western Luminol/Enhancer Reagent, Mini PROTEAN TGX Stain-Free precast gels for polyacrylamide gel electrophoresis, 10x Tris/Glycerine/SDS buffer, nitrocellulose membranes and Ponceau S solution were purchased from Bio-Rad, France. Human amylin [8-37] peptide (IAPP) and human beta-Amyloïd [1-42] (APP) were purchased from Cliniscience, France and Eurogentech, USA respectively. Beta Amyloid (1-42) Polyclonal Antibody, anti-rabbit HRP secondary antibody were purchased from Thermofisher. The water used for all experiment was purified with a Milli-Q system from Millipore Co (resistivity 18.2 MΩ.cm at 25°C).

S2. Synthesis

S2.1. Carboxylic acid enriched reduced graphene oxide (rGO-COOH)

To produce rGO-COOH, carboxylic acid enriched GO (GO-COOH) was first synthesized from GO.[285, 330] In short, sodium hydroxide (NaOH, 1.4 g) and chloroacetic acid (Cl-CH_2-COOH, 1 g) were added to 50 mL of GO (20 mg) aqueous solution and sonicated at 35 kHz for 2 h at 80 °C to convert hydroxyl groups present on GO to COOH via conjugation of acetic acid moieties and to partially reduce GO into rGO. The resulting rGO-COOH solution was quenched with HCl (20%), washed (four times) with distilled water until neutral pH and purified by repeated rinsing/centrifugation (4500 rpm, 30 min) cycles.

S2.2. Fabrication of metformin hydrogels

The metformin gel was fabricated by mixing GO or rGO-COOH (10 mg mL^{-1}) and metformin hydrochloride (10 mg mL^{-1}) at a volume ratio of 9:1 (v/v) and homogenized by sonication for 5 min prior to lyophilization for 12 h before use.

S2.3. Fabrication of PAA@rGO nanofiber mats via electrospinning

The electrospinning of nanofiber mats were performed according to the procedure described by us previsouly.[200] Briefly, dispersed aqueous rGO solution (1 mg mL^{-1}, 2.4 wt.%) was mixed with PAA (81.4 wt.%), and β-cyclodextrin (16.2 wt.%) and kept under magnetic stirring overnight. The resulting clear solution was electrospun using a 1 mL syringe fitted with a 14-gauge blunt needle at the rate of 0.35 mL min^{-1} at 15 kV. The distance was kept at 15 cm during the electrospinning process. Resulting electrospun fibres were cross-linked under vacuum at 140 °C for 30 min.

S2.4. Synthesis of Gelatin Methacrylate (GelMA)

Methacrylation of gelatin was carried out as described in a previous report with minor modifications.[331] In brief, 10 g of gelatin were added into 100 mL of PBS and heated to 50 °C under constant magnetic stirring. For a 1:1 ratio, 10 mL of methacrylic anhydride (MA) were gradually added to the above mixture and the reaction was kept under vigorous stirring for 3 h at 50 °C. The reaction was stopped by adding a five-fold volume (500 mL) of PBS. Residual salts and excess of MA were removed by dialysis in distilled water at 40 °C for one week using dialysis tubing with molecular weight cut-off of 12–14 kDa. Dialysis water was changed twice per day. After lyophilization for one week, GelMA was collected in the form of white porous foam and kept in the dark for further use.

S2.5. Preparation of microneedles (MNs)

S2.5.1. PDMS mold fabrication

A circular MNs array (named as C700, diameter 18 mm) was designed with 137 needles of a conical structure and micromachined on an aluminum surface to have a master mold. The needles have the following dimensions: 700 μm in height, 400 μm in length and tip-to-tip distance of 850 μm. This MNs array (tipped up) was covered with 10% cross-linked polydimethylsiloxane (PDMS) solution following vacuo to remove the bubbles and kept at 80 °C for 2 h. Hardened PDMS mold was gently separated from aluminum master mold.

S2.5.2. Microneedles' fabrication

Initially, 400 mg of GelMA were dissolved in 1.5 mL of PBS at 65 °C. Then, 10 mg of Irgacure 2959 as photoinitiator were mixed with 200 mg of PEGDA, 1.0 mg of MoS_2 and 0.2 mL of EtOH. This mixture was sonicated for 8 min. Afterwards, GelMA solution was mixed with other components and was complemented with 2.0 mL of PBS. The final solution was sonicated for another 8 min to remove the possible bubbles and 300 μL of GelMA:PEGDA (20:10 weight ratio) mixture was casted into preheated PDMS mold and kept under back vacuum for overnight at 30°C. UV irradiation (15 cm, 400 W, Delolux 3S) of the PDMS mold for 5 min resulted in the polymerization of the mixture immediately. The formed MNs were gently peeled from the mold, washed for 2 h in PBS to remove any non-polymerized monomers and stored in a desiccator until further use.

S2.6. Carbon quantum dots (CQDs)

S2.6.1. CQD-1 (carboxylated carbon quantum dots)

Carboxylated CQDs were synthesized according to a modified procedure.[332] To a stirring solution of glucosamine hydrochloride (1.00 g, 4.63 mmol) in distilled water (20 mL) in a 30 mL vial G30, b-alanine (0.454 g, 1.1 eq.) was added and stirred to ensure homogeneity. The reactor was then placed in a microwave (Monowave 450, Anton-Parr). The solution was heated under pressure for 2 min from room temperature to 200 1C and then maintained for 1 min at 200 °C under stirring (1200 rpm). The resulting brown solution was centrifuged at 4 °C (10 000g, 10 min) in order to remove big particles. The supernatant was dialyzed against water during 24 h (SpectraPor RC membranes, 1 kDa) and then kept (or lyophilized) to yield a brown solution.

S2.6.2. CQD-2 (aminated carbon quantum dots)

To a stirring solution of glucosamine hydrochloride (1.00 g, 4.63 mmol) in distilled water (20 mL) in a 30 mL vial G30, ethylenediamine (0.307 g, 1.1 eq.) was added and stirred to ensure homogeneity. The reactor was then placed in a microwave (Monowave 450, Anton-Parr). The solution was heated under pressure for 5 min from room temperature to 200 °C and then maintained for 10 min at 200 °C under stirring (1200 rpm). The resulting brown solution was centrifuged at 4 °C (10 000g, 10 min) in order to remove big particles. The supernatant was dialyzed against water during 24 h (SpectraPor RC membranes, 1 kDa) and then kept (or lyophilized) to yield a brown solution.

S2.6.3. CQD-3 (fluorinated carbon quantum dots)

Fluorinated CQDs were synthesized according to a procedure described previously [312] Briefly, 4 mL of hydrofluoric acid (HF) was mixed with 10 mL of 1 % glucose aqueous solution. The mixture was placed into microwave reactor (Monowave 450, Anton-Parr) and kept under continuous stirring at 180 °C for 1 h until brown color dispersion was produced. In order to remove larger particles, the dispersion was filtrated through a 0.2 μm filter and pH was neutralized with NaOH 1 M. The supernatant was dialyzed against water during 24 h (SpectraPor RC membranes, 1 kDa) and then kept (or lyophilized) to yield a brown solution.

S3. Characterisations of nanofiber mats

S3.1. Swelling degree

The swelling degree of PAA@rGO nanofibers was determined following the method reported by Mittal et al.[333] The nanofiber mat was cut into smaller pieces (1 × 1 cm) and dried at 70 °C for 24 h before weighting. The dried samples were then immersed in Milli-Q water at room temperature for 1 h and taken off at given time intervals (2 s - 10 min). The nanofiber pieces were dried with a cotton tissue in order to remove any remaining water and weighted using a microbalance. The swelling ratio of nanofiber mats was calculated as following:

$$\text{Swelling degree (\%)} = \frac{Wt - Wd}{Wd} \times 100$$

where W_t is the weight of wet nanofibers at time t and W_d is the weight of dry nanofibers.

S3.2. Weight and thickness

The measurements of weight and thickness were performed in triplicates on randomly selected patches from 5 independent batches. The thickness was determined using a thickness gage ID-C112XBS from Mitutoyo Corporation (Japan). For weight determination, the mats of 1×1 cm^2 in size were weighted on a digital balance.

S4. Drug loading

S4.1. Insulin loaded PAA@rGO electrospun nanofibers

Insulin-FITC and insulin loaded patches were produced by immersion of 3.0±1.0 mg PAA@rGO electrospun mats into 1 mL (200 μg mL^{-1}) of insulin-FITC or insulin aqueous solutions under continuous shaking at 150 rpm for 4 h at 4°C.

S4.2. Insulin loaded MoS_2-MNs

MNs array was immersed into 2.0 mL of 100 μg mL^{-1} insulin solution under continuous shaking at 150 rpm for 8 h at 4 °C.

S5. *Ex vivo* permeation experiments

S5.1. Murine skin for metformin loaded hydrogels

Skin permeation studies were performed using fresh mice skin. For this, mice C57BL/6 were anaesthetized with isoflurane, shaved with an electric shaver (Philips Series 7000) and further treated with a depilatory cream (Veet) for 1.5 min. Then mice were killed by cervical dislocation and the skin from the back of the mice was cut into pieces of at least 20 mm in diameter and preserved in Dulbecco's modified Eagle medium (DMEM) supplemented with gentamicin (0.4%).

Static Franz diffusion cell (Proviskin, France) exhibiting an effective area of 0.785 cm^2 were used for skin permeability tests. After filling the receptor compartment with degassed phosphate buffer saline (PBS, pH = 7.4) the solution was maintained at 32 °C using a circulating bath (Julabo) and stirred with a magnetic stirring bar at around 500 rpm. Freshly cut mouse skin was clamped between the donor and the receptor compartment (8 mL), pre-incubated for 20 min, and wetted with 30 μL of a glycerin solution (50%) to insure contact between the gel and the skin. At determined time intervals, 500 μL aliquots of diffused solution were removed from the receptor compartment and analyzed using HPLC. After each sampling, an equal volume of fresh diffusion medium was added to the receptor compartment to maintain a constant volume. All experiments were performed in triplicates.

To estimate the amount of metformin trapped in the mice skin, the skin was added into a water/ice mixture for 10 min and sonicated in the presence of ZrO_2 beads (4 mm in diameter), before being centrifuged for 30 min at 13500 rpm using an ultracentrifuge (Midi Scanfuge ORIGIO). The liquid phase was collected and filtrated through a 0.1 µm Nylon filter (Whatman Puradisc 13 mm) and the amount of metformin was determined. The metformin flux (J, µg cm-2 h^{-1}) was determined according to equation (1):

$$J = m/A \qquad (1)$$

with m being the linear slope of the cumulative metformin amount versus time curves in equilibrium conditions (µg h^{-1}), and A is the surface of the membrane of the Franz cell (0.785 cm^2).

S5.2. Porcine buccal mucosa and cornea for insulin loaded PAA@rGO nanofibers

All animal studies were conducted at the Plateforme de Recherche Expérimentale (University of Lille, France) in accordance with the ethnic protocol entitled "Délivrance transdermique, de substances pharmacologiques, contrôlée par l'utilisation d'une énergie thermique chez la souris et le mini-porc" (Nr. APAFIS#21080-2019111511521244). 3 female mini-pigs weighting 10-16 kg were used. Ex-vivo permeation experiments were performed using cornea and buccal mucosal lining from pigs. Fresh porcine buccal mucosa was separated from the underlining tissue using a scalpel and stored in PBS 1× at 4 °C not more than 12 h before the permeation experiment. Tissue with any visual damage was discarded. Intact mucosa was immersed in deionized water at 65 °C for 60 s in order to separate the epithelium from the connective tissue as reported previsouly.[334] Mucosa samples (thickness 310±80 µm) were gently cut into pieces (1 cm^2) and placed between the chambers of Franz diffusion cell and ex-vivo experiment was performed. In the case of pig cornea, they were gently cut into 1.8 cm^2 circular pieces prior to their use in the Franz diffusion cell. Insulin skin diffusion experiments were carried out using static Franz diffusion cell (Proviskin, France), exhibiting an effective area of 0.785 cm^2.The receptor chamber was filled with 1× PBS (pH 7.4) solution and maintained at 37 °C using a circulating bath (Julabo) with magnetic stirring at around 500 rpm. The cornea pieces were carefully clamped between the donor and the receptor chambers (8 mL) and pre-incubated for 20 min. The drug loaded electrospun mats were irradiated with a continuous wave laser at 980 nm for 10 min (laser power=1 Wcm^{-2}). At determined time intervals, 300 µL aliquots of diffused solution were removed from the receptor compartment and analysed by HPLC. After each sampling, an equal volume of fresh diffusion medium was added to the receptor chamber.

S6. *In vivo* insulin experiments on pigs

Microneedles penetration and insulin delivery in vivo were tested on female pigs weighing 52-60 kg. The animals were subjected to total pancreatectomy a day before each experiment. A tunneled central venous catheter into the external jugular vein was placed in each animal facilitating a blood sampling. The insulin loaded microneedles (2.8 IU) were placed on the pig's ear and fixed with adhesive tape (Sparadrap Micropore, 2133). The microneedles were photothermally-activated for 10 min to a temperature of ~50 °C. Glucose levels were measured directly from fresh blood using a commercial glucometer. Blood samples were obtained at definite time intervals. Blood samples were centrifuged at 5000 rpm for 10 min at 4 °C and the plasma was immediately separated and stored at –80 °C until analysis. Radioimmunoassay kits were used for the measurements of insulin (Bi-Insuline RIA ® ; Bio-Rad, Elexience, Verrières-le-Buisson, France). All the manipulations in pigs, including total pancreatectomy, placing of the catheter, microneedles and activation as well as blood samplings, were performed under general anesthesia with a 4% concentration of isoflurane (Aerrane; Baxter, France). Animal studies were approved by the Institutional Ethics Committees for the Care and Use of Experimental Animals of the University of Lille (protocol n°21080). All experiments were performed in accordance with the guidelines for animal use specified by the European Union Council Directive of September 22, 2010 (2010/63/EU).

S7. *In vitro* photothermal drug release studies

Release experiments were performed into 1 mL deionized water under passive conditions (without any stimulation) and upon illumination of the metformin based gels, insulin loaded MoS_2-MNs or insulin loaded PAA@rGO nanofibers using a 980 nm continuous wave laser (Gbox model, Fournier Medical Solution) at 0.5-1.0 W cm^{-2} for 10 min. The temperature changes were captured by an infrared camera (Thermovision A40) and treated using ThermaCam Researcher Pro 2.9 software. The amounts of metformin or insulin released were evaluated by high-performance liquid chromatography (HPLC) of the solution collected after irradiation using calibration curves generated for each drug.

S8. Tissue staining

To determine the integrity of the tissue after heat treatment, human skin, porcine mucosa and cornea were fixed with paraformaldehyde (4 %), embedded in paraffin and sectioned (5 µM pieces in thickness). Tissue sections were stained with hematoxylin and eosin (H&E) to observe the tissue structure.

S9. Tissue imaging

To evaluate the penetration of FITC-labeled insulin, porcine mucosa or cornea were frozen in OCT (Optimal Cutting Temperature) compound and cut with Leica CM3050 S cryostat (thickness of 10 μm) and placed on a glass slide. The glass slides were directly observed using a Cytation 5 Cell Imaging Multi-Mode Reader (BioTek Instruments SAS, France) equipped with a 4x or 20x objective (Plan Fluorite WD 6.7 NA 0.45). The fluorescence signal was acquired using excitation and emission filter sets for GFP (exc. 469/35 nm and em. 525/39 nm). All the images were further analyzed by Gen5iPlus 3.04 Imaging Software.

S10. Biological assays

S10.1. Determination of metformin activity

In vitro assessment of metformin activity was performed using the Immortalized Human Hepatocytes (IHH) as relevant Human hepatocyte cell model as they retain features of normal hepatocytes.[252] IHH cells (maintained at passages 25-35) were cultured in Williams E medium (Invitrogen) containing 11 mM glucose and supplemented with 10 % fetal bovine serum (FBS; Gibco®), 100 U/mL penicillin, 100 μg/mL streptomycin, 20 mU/mL insulin and 50 nM dexamethasone. The activity of metformin when heated at 45 °C, 55 °C and 65 °C was assessed by monitoring the glucose-6-phosphatase catalytic (G6PC) gene expression from IHH cells (4×10^5 cells) cultured in 12-well plates in a Dulbecco's Modified Eagle Medium (DMEM) supplemented with 5 mM glucose, 2 % FBS, 100 U/mL penicillin, 100 μg/mL streptomycin containing either PBS (Control) or 5 mM heated metformin for 24 h. Total RNA was extracted from IHH cells according to the manufacturer's protocol (RNeasy Lipid Tissue Kit, Qiagen). The RNA purity and concentration were determined by RNA Integrity Number (RNA 6000 Nano Kit, 2100 Bioanalyser, Agilent). Total RNA was transcribed into cDNA as described before.28 Each cDNA sample was quantified by quantitative real-time polymerase chain reaction using the fluorescent TaqMan 5′-nuclease assays or a BioRad MyiQ Single-Color Real-Time PCR Detection System using the BioRad iQ SYBR Green Supermix, with 100 nM primers and 1 μL of template per 20 μL of PCR and an annealing temperature of 60 °C. Gene expression analysis was normalized against TATA box Binding Protein (TBP) expression or 60S acidic ribosomal protein P0 (RPLP0). Primers for human RPLP0 (sense 5′-ACCTCCTTTTTCCAGGCTTT-3′; antisense 5′-CCCACTTTGTCTCCAGTCTTG -3′);Primers forhuman G6PC (sense 5'-AGACTCCCAGGACTGGTTCA-3'; antisense5'-

ACAGGTGACAGGGAACTGCT-3'); Primers for human TBP (sense 5'-GAACCACGGCACTGATTTTC-3' and antisense 5'- CCCCACCATGTTCTGAAT

S10.2. Determination of insulin activity

The activity of released insulin was evaluated, in vitro, on a immortalized human hepatocytes (IHH) cell line model using native insulin as a positive control and the same culture without insulin as a negative control as described previously.[90] After overnight culture in a serum-free and glucose-free culture medium, IHH cells were incubated for 1 h without insulin (negative control), with native insulin (positive control) and with released insulin at a physiological active concentration of 200 nM. After 1 h of incubation, cells were lysed and proteins were collected. Expression of p-Akt and Akt proteins was evaluated by Western blotting analysis. For Western blotting experiments, 40 µg of total proteins of each condition were loaded and separated onto a polyacrylamide gel, then transferred on a nitrocellulose membrane. β-actin was used as an internal control. Immunoblotting for p-Akt and Akt was performed using anti p-Akt specific antibody (Thr-308, Cell signaling), anti Akt specific antibody (sc-8312, Santa Cruz) and fluorescence-coupled secondary antibodies against both mouse and rabbit primary antibodies. Analysis of the Western blot was performed using Odyssey revelation process and ImageJ quantification technique. A one-way ANOVA test was carried out.

S10.3. Cytotoxicity tests of PAA@rGO bandage

The ARPE-19 spontaneously immortalized cell line of human retinal pigment epithelium and the HeLa cells, derived from cervical carcinoma from a 31-year old female [ATCC® CCL-2™, ECACC, Sigma Aldrich, Saint-Quentin Fallavier, France], were cultured and maintained in Dulbecco's Modified Eagle's medium (DMEM, Gibco®) high glucose with 2 mM Glutamine, DMEM/F12 media with 2 mM Glutamine and DMEM supplemented with 10% fetal bovine serum (FBS, Gibco®) and 1% penicillin-streptomycin (Gibco®), respectively, in a humidified incubator at 37 °C and 5% CO_2. Cells were seeded at a density of $5x10^5$ cells/well in a 12-well plate and grown for 24 h before assay. The day of experiment, the cell medium was changed and pieces of PAA@rGO mats were immersed into the cell medium allowing to swell. Passive and active mode (with 10 min 980 nm laser patch activation at 0.7 W cm^{-2}) were applied in order to check viability of cells without and with laser irradiation of nanofiber mats. After 10 min the mats were removed and the cell viability was evaluated using resazurin cell viability method. Briefly, 1 mL of the resazurin solution (11 µg mL^{-1}) in complete medium was added to each well containing the gel and the plate was incubated for 4 h in the humidified incubator.

The fluorescence emission of each well was measured at 593 nm (20-nm bandwidth) with an excitation at 554 nm (18-nm bandwidth) using a Cytation™ 5 Cell Imaging Multi-Mode Reader (BioTek Instruments SAS, France). Each condition was replicated three times.

S10.4. Cytotoxicity tests of CQDs

Cytotoxicity of prepared carbon quantum dots was tested at the concentrations of 1, 10 and 100 μg mL^{-1}. The rat insulinoma cell line (INS-1E) was cultured in RPMI-1640 medium supplemented with 10% fetal bovine serum (FBS, Gibco®), 1% penicillin-streptomycin (Gibco®), 1% sodium pyruvate, 50 μM β –mercaptoethanol. The MIN-6 cell line derived from a mouse insulinoma was cultured in Dulbecco's Modified Eagle's medium (DMEM, Gibco®) high glucose with 4 mM glutamine supplemented with 10% fetal bovine serum (FBS, Gibco®) 1% penicillin-streptomycin and 0.1 mM β-mercaptoethanol. Both cells were seeded at a density of 10^5 cells/well in a 96-well plate and grown for 24 h before assay. The culture medium was replaced with a fresh medium that contains the CQDs at 1, 10 and 100 μg mL^{-1}. After 24 h, the old medium was aspirated and cells were washed with PBS. The cell viability was evaluated using resazurin cell viability assay as described above.

S10.5. Thioflavin T kinetics assay

To assess the fibrillization kinetics of IAPP and APP in the presence of CQDs, a freshly prepared 573.8 μM ThT solution was mixed with samples at a 1:2 molar ratio of ThT:peptide. The final concentrations of ThT and IAPP were 10 μM and 20 μM respectively. The assays were performed at 37 ºC on a Nunc™ MicroWell™ white polystyrene 96-well plate and changes in ThT fluorescence were recorded every 10 min over 15-25 h, at excitation/emission 440/484 nm using Cytation™ 5 multi-mode microplate reader. All samples were analyzed in triplicate.

S10.6. Influence of glucose on hIAPP aggregation

To perform the fibrillization of hIAPP in the presence of glucose, 2.5 mM stock solution of hIAPP in DMSO was mixed with a freshly prepared 573.8 μM ThT solution and 1 M glucose stock solution in PBS to get the final glucose concentration of 5 mM. 11 mM and 33 mM. The final concentration of ThT and hIAPP were 10 μM and 20 μM respectively. The assays were performed at 37 ºC on a Nunc™ MicroWell™ white polystyrene 96-well plate and changes in ThT fluorescence were recorded every 10 min over 15-25 h, at excitation/emission 440/484 nm using Cytation™ 5 multi-mode microplate reader. All samples were analyzed in triplicate.

S10.7. Influence of palmitate on hIAPP aggregation

To perform the fibrillization of hIAPP in the presence of palmitate, 2.5 mM stock solution of hIAPP in DMSO was mixed with a freshly prepared 573.8 μM ThT solution and 150 mM sodium palmitate stock solution in 50% ethanol-10% bovine serum albumin (BSA) solution to get the final palmitate concentration of 125 μM. The final concentrations of ThT and hIAPP were 10 μM and 20 μM respectively. The assays were performed at 37 ºC on a Nunc™ MicroWell™ white polystyrene 96-well plate and changes in ThT fluorescence were recorded every 10 min over 15-25 h, at excitation/emission 440/484 nm using Cytation™ 5 multi-mode microplate reader. All samples were analyzed in triplicate.

S10.8. Preparation of peptides (hIAPP, APP) and heterocomplexes (IAPP/APP)

Dry peptides were weighed and dissolved in 1,1,1,3,3,3-hexafluoro-2-propanol (HFIP, Sigma-Aldrich) for 1 h at room temperature (RT) and then separated into 100 μg aliquots. The HFIP was left to evaporate overnight at RT, producing dry peptide films which were stored at –20 °C for future use. Before each experiment, fresh APP and IAPP solutions were prepared by initially solubilizing the dry peptide in dimethyl sulfoxide (DMSO, Thermofisher) to make a 2.5 mM stock. The IAPP and APP were mixed in a ratio of 1:1 to obtain the final concentration of 200 μM. The peptide solutions were incubated at 4 °C and 37 °C for 24 h to allow formation of oligomers and fibrils.

S10.9. Western blotting of APP/IAPP aggregates

To perform Western blotting, first, the proteins were denatured for 3 min at 95°C. For a gel electrophoresis, 50 μg of total proteins was separated in precast 4-15% TGX stain free gels at 200 V for 30 min. Subsequently, gels were blotted to nitrocellulose membranes at 250 mA for 2 h. Immunoblotting for aggregates was performed using beta Amyloid (1-42) rabbit specific primary antibody and anti-rabbit HRP secondary antibody. Analysis of the Western blot was performed using Clarity ECL substrates based on chemiluminescent revelation process. The imaging of the membrane was performed using ChemiDoc MP Imaging System. The ImageJ was used for quantification.

S10.10. Cytotoxicity of heterocomplexes (IAPP/APP) in diabetogenic condition

Cytotoxicity of prepared heterocomlexes was tested on INS-1E and MIN6 cells. The rat insulinoma cell line (INS-1E) was cultured in RPMI-1640 medium supplemented with 10% fetal bovine serum (FBS, Gibco®), 1% penicillin-streptomycin (Gibco®), 1% sodium pyruvate, 50 μM β –mercaptoethanol. The MIN-6 cell line derived from a mouse insulinoma was cultured

in Dulbecco's Modified Eagle's medium (DMEM, Gibco®) high glucose with 4 mM glutamine supplemented with 10% fetal bovine serum (FBS, Gibco®) 1% penicillin-streptomycin and 0.1 mM β-mercaptoethanol. Both cells were seeded at a density of 10^5 cells/well in a 96-well plate and grown for 24 h before assay. The heterocomplexes were allowed to form according to a procedure described above. The day of experiment the medium of cells was replaced by a fresh medium containing glucose solution (final concentration 20 mM), palmitate solution in 50% EtOH-10% bovine serum albumin (BSA) (final concentration 0.5 mM) or glucose and palmitate mixture (final concentrations 20 mM and 0.5 mM respectively). The heterocomplexes and fresh peptides as a control were added to get a final concentration of 20 μM. The cells were allowed to incubate for 48 h at 37°C. All samples were analyzed in triplicate. The cell viability was evaluated using resazurin cell viability assay as described above.

S11. Instrumentation

S11.1. Fourier transform infrared spectroscopy (FT-IR)

FT-IR analyses were performed on Thermo Fisher Scientific Inc. Nicolet 8700, in the frequency range between 650 and 4000 cm^{-1} with a resolution of 6 cm cm^{-1}. Samples (around 1 mg) were mixed with potassium bromide powder (200 mg) in an agar mortar. The mixture was pressed into a pellet under 7 tons, and the spectrum was recorded immediately. An average of 64 scans was carried out for each sample.

S11.2. Raman spectroscopy measurements

Raman spectroscopy measurements were performed on a Horiba Jobin Yvon LabRam high resolution micro-Raman system combined with a 473 nm (1 mW) laser diode as excitation source. Visible light is focused by a 100× objective. The scattered light is collected by the same objective in backscattering configuration, dispersed by a monochromator with 1800 mm focal length and detected by a CCD camera.

S11.3. Scanning electron microscopy (SEM)

Scanning electron microscopy (SEM) micrographs of prepared mats were performed with an electron microscope Hitachi S-4800 FE-SEM (Hitachi Technologies Corp., Tokyo, Japan). The samples were sputtered with a gold/palladium layer before scanning. The accelerating voltage was 10 kV, the probe current was 9800 nA.

S11.4. Transmission electron microscopy (TEM)

The morphology and sizes of CQDs were characterized using FEI Tecnai G2-20 microscope.

S11.5. Atomic force microscopy (AFM)

AFM images were recorded in tapping mode on a Dimensiont 3100 (Digital Instruments) in air at a scan rate of 1 Hz, and with an antimony doped n-type silicon cantilever (resistivity: 0.01–0.025 ohm cm, frequency resonance ranging from 130 to 250 kHz – with a constant stiffness k ~ 48 N m^{-1}). Samples were diluted by 15 with filtered PBS, deposited on freshly cleaved mica substrates, dried in air and then rinsed three times with water. Data were analyzed with a Gwyddion software (2.56).

S11.6. pH measurements

The pH values of solutions were adjusted with HCl and NaOH solutions using a SevenCompact pH meter S210-Std-Kit (Mettler Toledo, USA).

S11.7. High-performance Liquid Chromatography (HPLC)

HPLC analysis was performed using a Shimadzu LC2010-HT system (Shimadzu, Tokyo, Japan) on a C18 stationary phase (2.6 µm, 150 × 4.6 mm i.d.) from (Interchim, Montluçon, France) heated to 40 ^{o}C. The mobile phase consisted of formic acid (0.1%) in water as eluent A and the eluent B was formic acid (0.1%) in acetonitrile:water (90:10 %, v/v) (flux: 1 mL min^{-1}). Detection was performed using 2789 UV-Vis detector at 215 nm.

S11.8. Microwave reactor

Synthesis of carbon quantum dots was performed in the microwave glass or silicon carbide (SiC) reactor placed in a Monowave 450, Anton-Parr microwave. The time of reaction was controlled from 1 to 3 h.

S11.9. Size and zeta-potential measurements

DLS measurements were carried out by Zetasizer Nano-ZS (Malvern Instruments Inc. Worcestershire, UK). Nanomaterials were diluted to 1 nM and measured in Milli-Q water.

S11.10. X-ray photoelectron spectroscopy (XPS)

X-ray photoelectron spectroscopy (XPS) was recorded using ESCALAB 220 XL spectrometer from Vacuum Generators featuring a monochromatic Al Kα X-ray source (1486.6 eV) and a spherical energy analyzer operated in the CAE (constant analyzer energy) mode (CAE = 100 eV for survey spectra and CAE = 40 eV for high-resolution spectra), using the electromagnetic

lens mode. The angle between the incident X-rays and the analyzer is 58° and the detection angle of the photoelectrons is 30°.

S11.11. UV-Vis Absorption

UV-Vis Absorption spectra were recorded using a Perkin Elmer Lambda UV-Vis 950 spectrophotometer in a 1-cm quartz cuvette. The wavelength range was 200-1100 nm

S11.12. Fluorescence spectroscopy

Emission and excitation fluorescence spectra were recorded between 200–900 nm using a Xenius XC spectrofluorometer (Safas S.A., Monaco). Fluorescence measurements of CQDs were performed in PBS (pH 7.4, 0.01 M, Gibco®)at 20 $mgmL^{-1}$ (excitation and emission band width =10 nm, step = 1 nm, PMT voltage = 460 V, ultrascan). For quantum yield measurements, fluorescence emissions were recorded from 350–900 nm with an excitation wavelength of 350 nm (excitation and emission bandwidth = 10 nm, step = 1 nm, PMT voltage = 260 V, ultrascan). Integrated fluorescence emissions were calculated from 365 to 680 nm.

S11.13. Photothermal effect measurements

The photothermal effect was assessed using a 980 nm-continuous wave laser (Gbox model, Fournier Medical Solution) with an output light at 980 nm at power densities 0.5, 0.7 and 1 W cm^{-2}. This laser was injected into a lens (position 25) and placed at 10.5 cm from the bottom of the wells. The output was not collimated and the resulting beam divergence allowed to illuminate uniformly every well. The temperature changes on the surface of the samples were captured by an infrared camera (Thermovision A40) and treated using ThermaCam Researcher Pro 2.9 software

S11.14. Adhesive strength measurements

Mechanical properties of elastomeric PAA@rGO fibers were investigated via a TA XT plus C Texture Analyser. The fiber samples were soaked in water and squeezed between tensile grips; a tension test was applied using the following parameters with a pre-test speed of 1.0 mm/s, test speed of 0.5 mm/s and a post-test speed of 10 mm/s. Tensile test was performed until seeing a macroscopic damage of the fibers. Relative analysis was applied to calculate stress, strain and Young modulus of elasticity.

PUBLICATIONS

Anna Voronova, Cristina Prieto, Maria Pardo-Figuerez, Jose Maria Lagaron, Amitav Sanyal, Bilal Demir, Thomas Hubert, Valerie Plaisance, Valerie Pawlowski, Severine Vignoud, Alexandre Barras, Amar Abderrahmani, Rabah Boukherroub: *Photothermal activatable mucoadhesive fibre mats for on-demand delivery of insulin via buccal mucosa and corneal* (**Submitted**)

Bilal Demir, Lea Rosselle, Anna Voronova, Quentin Pagneux, Audrey Quenon, Valery Gmyr, Dorothee Jary, Nadia Skandrani, Nathalie Hennuyer, Bart Staels, Thomas Hubert, Amar Abderrahmani, Valerie Plaisance, Valerie Pawlowski, Rabah Boukherroub, Severine Vignoud, Sabine Szunerits: *Innovative transdermal delivery of insulin using gelatin methacrylate-based Microneedle Patches in Mice and Mini-pigs* (**Submitted**)

Sabine Szunerits, Sorin Melinte, Alexandre Barras, Quentin Pagneux, Anna Voronova, Amar Abderrahmani and Rabah Boukherroub : *The impact of chemical engineering and technological advances on managing diabetes: Present and future concepts.* **Chem. Soc. Rev.**, 2021,**50**, 2102-2146

Li Chengnan, Quentin Pagneux, Anna Voronova, Alexandre Barras, Amar Abderrahmani, Valérie Plaisance, Valerie Pawlowski, Nathalie Hennuyer, Bart Staels, Lea Rosselle, Nadia Skandrani, Musen Li, Rabah Boukherroub and Sabine Szunerits : *Near-infrared light activatable hydrogels for metformin delivery.* **Nanoscale**, 2019, **11**, 15810–15820

REFERENCES

1. Cho, N. H.; Shaw, J. E.; Karuranga, S.; Huang, Y.; da Rocha Fernandes, J. D.; Ohlrogge, A. W.; Malanda, B., IDF Diabetes Atlas: Global estimates of diabetes prevalence for 2017 and projections for 2045. *Diabetes Res Clin Pract* **2018,** *138*, 271-281.

2. Deshpande, D. A. H.-H., M.; Schootman, M., Epidemiology of Diabetes and Diabetes-Related Complications. *Physical Therapy* **2008,** *88* (11).

3. Katulanda, P.; Dissanayake, H. A.; Ranathunga, I.; Ratnasamy, V.; Wijewickrama, P. S. A.; Yogendranathan, N.; Gamage, K. K. K.; de Silva, N. L.; Sumanatilleke, M.; Somasundaram, N. P.; Matthews, D. R., Prevention and management of COVID-19 among patients with diabetes: an appraisal of the literature. *Diabetologia* **2020,** *63* (8), 1440-1452.

4. American Diabetes, A., (2) Classification and diagnosis of diabetes. *Diabetes Care* **2015,** *38 Suppl*, S8-S16.

5. DeFronzo, R. A.; Ferrannini, E.; Groop, L.; Henry, R. R.; Herman, W. H.; Holst, J. J.; Hu, F. B.; Kahn, C. R.; Raz, I.; Shulman, G. I., Type 2 diabetes mellitus. *Nature reviews Disease primers* **2015,** *1* (1), 1-22.

6. Ginter, E.; Simko, V., Type 2 diabetes mellitus, pandemic in 21st century. *Diabetes* **2013**, 42-50.

7. Inzucchi, S. E.; Sherwin, R. S., Type 2 diabetes mellitus. *Cecil Medicine. 24th ed. Philadelphia, Pa: Saunders Elsevier* **2011**.

8. Hardy, O. T.; Czech, M. P.; Corvera, S., What causes the insulin resistance underlying obesity? *Curr Opin Endocrinol Diabetes Obes* **2012,** *19* (2), 81-7.

9. Czech, M. P., Insulin action and resistance in obesity and type 2 diabetes. *Nat Med* **2017,** *23* (7), 804-814.

10. White, M. G.; Shaw, J. A.; Taylor, R., Type 2 Diabetes: The Pathologic Basis of Reversible beta-Cell Dysfunction. *Diabetes Care* **2016,** *39* (11), 2080-2088.

11. Colberg, S. R.; Sigal, R. J.; Fernhall, B.; Regensteiner, J. G.; Blissmer, B. J.; Rubin, R. R.; Chasan-Taber, L.; Albright, A. L.; Braun, B.; American College of Sports, M.; American Diabetes, A., Exercise and type 2 diabetes: the American College of Sports Medicine and the American Diabetes Association: joint position statement. *Diabetes Care* **2010,** *33* (12), e147-67.

12. Association, A. D., Screening for diabetes. *Diabetes care* **2002,** *25* (suppl 1), s21-s24.

13. Wilcox, N. S.; Rui, J.; Hebrok, M.; Herold, K. C., Life and death of beta cells in Type 1 diabetes: A comprehensive review. *J Autoimmun* **2016,** *71*, 51-8.

14. Noble, J. A.; Valdes, A. M., Genetics of the HLA region in the prediction of type 1 diabetes. *Curr Diab Rep* **2011,** *11* (6), 533-42.

15. Sanyoura, M.; Philipson, L. H.; Naylor, R., Monogenic Diabetes in Children and Adolescents: Recognition and Treatment Options. *Curr Diab Rep* **2018,** *18* (8), 58.

16. Lemelman, M. B.; Letourneau, L.; Greeley, S. A. W., Neonatal Diabetes Mellitus: An Update on Diagnosis and Management. *Clin Perinatol* **2018,** *45* (1), 41-59.

17. Rakocevic, G.; Floeter, M. K., Autoimmune stiff person syndrome and related myelopathies: Understanding of electrophysiological and immunological processes. *Muscle & Nerve* **2012,** *45* (5), 623-634.

18. Martins, L. M.; Fernandes, V. O.; Carvalho, M. M. D.; Gadelha, D. D.; Queiroz, P. C.; Montenegro Junior, R. M., Type B insulin resistance syndrome: a systematic review. *Arch Endocrinol Metab* **2020,** *64* (4), 337-348.

19. Sato, N.; Ohsawa, I.; Takagi, M.; Gohda, T.; Horikoshi, S.; Shirato, I.; Yamaguchi, Y.; Tomino, Y., Type B insulin resistance syndrome with systemic lupus erythematosus. *Clinical nephrology* **2010,** *73* (2), 157-162.

20. Ostwal, V.; Oak, J., Type B insulin resistance in a systemic lupus erythematosus patient. *International journal of rheumatic diseases* **2009,** *12* (2), 174-176.

21. Gillespie, K. M.; Dix, R. J.; Williams, A. J.; Newton, R.; Robinson, Z. F.; Bingley, P. J.; Gale, E. A.; Shield, J. P., Islet autoimmunity in children with Down's syndrome. *Diabetes* **2006,** *55* (11), 3185-8.

22. Bojesen, A.; Kristensen, K.; Birkebaek, N. H.; Fedder, J.; Mosekilde, L.; Bennett, P.; Laurberg, P.; Frystyk, J.; Flyvbjerg, A.; Christiansen, J. S.; Gravholt, C. H., The metabolic syndrome is frequent in Klinefelter's syndrome and is associated with abdominal obesity and hypogonadism. *Diabetes Care* **2006,** *29* (7), 1591-8.

23. Robinson, S.; Kessling, A., 9 Diabetes secondary to genetic disorders. *Baillière's clinical endocrinology and metabolism* **1992,** *6* (4), 867-898.

24. Ferner, R., 8 Drug-induced diabetes. *Baillière's clinical endocrinology and metabolism* **1992,** *6* (4), 849-866.

25. Fathallah, N.; Slim, R.; Larif, S.; Hmouda, H.; Salem, C. B., Drug-induced hyperglycaemia and diabetes. *Drug safety* **2015,** *38* (12), 1153-1168.

26. Repaske, D. R., Medication-induced diabetes mellitus. *Pediatr Diabetes* **2016,** *17* (6), 392-7.

27. Stalenhoef, J. E.; Alisjahbana, B.; Nelwan, E. J.; van der Ven-Jongekrijg, J.; Ottenhoff, T. H.; van der Meer, J. W.; Nelwan, R. H.; Netea, M. G.; van Crevel, R., The role of interferon-gamma in the increased tuberculosis risk in type 2 diabetes mellitus. *Eur J Clin Microbiol Infect Dis* **2008,** *27* (2), 97-103.

28. Resmini, E.; Minuto, F.; Colao, A.; Ferone, D., Secondary diabetes associated with principal endocrinopathies: the impact of new treatment modalities. *Acta Diabetol* **2009,** *46* (2), 85-95.

29. Geiss, L. S.; Herman, W. H.; Smith, P. J., Mortality in non-insulin-dependent diabetes. *Diabetes in America* **1995,** *2*, 233-55.

30. La Sala, L.; Prattichizzo, F.; Ceriello, A., The link between diabetes and atherosclerosis. *European journal of preventive cardiology* **2019,** *26* (2_suppl), 15-24.

31. Mogensen, C., Long-term antihypertensive treatment inhibiting progression of diabetic nephropathy. *Br Med J (Clin Res Ed)* **1982,** *285* (6343), 685-688.

32. Chudyk, A.; Petrella, R. J., Effects of exercise on cardiovascular risk factors in type 2 diabetes: a meta-analysis. *Diabetes care* **2011,** *34* (5), 1228-1237.

33. Candrilli, S. D.; Davis, K. L.; Kan, H. J.; Lucero, M. A.; Rousculp, M. D., Prevalence and the associated burden of illness of symptoms of diabetic peripheral neuropathy and diabetic retinopathy. *Journal of Diabetes and its Complications* **2007,** *21* (5), 306-314.

34. Gregg, E. W.; Sorlie, P.; Paulose-Ram, R.; Gu, Q.; Eberhardt, M. S.; Wolz, M.; Burt, V.; Curtin, L.; Engelgau, M.; Geiss, L., Prevalence of lower-extremity disease in the US adult population≥ 40 years of age with and without diabetes: 1999–2000 national health and nutrition examination survey. *Diabetes care* **2004,** *27* (7), 1591-1597.

35. Pirart, J., Diabetes mellitus and its degenerative complications: a prospective study of 4,400 patients observed between 1947 and 1973 (author's transl). *Diabete & metabolisme* **1977,** *3* (2), 97-107.

36. Adler, A. I.; Boyko, E. J.; Ahroni, J. H.; Stensel, V.; Forsberg, R. C.; Smith, D. G., Risk factors for diabetic peripheral sensory neuropathy: results of the Seattle Prospective Diabetic Foot Study. *Diabetes care* **1997,** *20* (7), 1162-1167.

37. Shaw, J.; Zimmet, P., The epidemiology of diabetic neuropathy. *Diabetes Review* **1999,** *7* (4), 245-252.

38. Perkins, B. A.; Greene, D. A.; Bril, V., Glycemic control is related to the morphological severity of diabetic sensorimotor polyneuropathy. *Diabetes care* **2001,** *24* (4), 748-752.

39. Tesfaye, S.; Chaturvedi, N.; Eaton, S. E.; Ward, J. D.; Manes, C.; Ionescu-Tirgoviste, C.; Witte, D. R.; Fuller, J. H., Vascular risk factors and diabetic neuropathy. *New England Journal of Medicine* **2005,** *352* (4), 341-350.

40. WageaAllaBalla, D. I.; Abdalla, A. M.; Elrayah, Z.; Elazomi, A.; Mohamed, E. I.; Bahroun, S., Vitamin D Deficiency in Sudanese patients with type 2 Diabetes Mellitus: with and without Diabetic Retinopathy.

41. Stratton, I. M.; Aldington, S. J.; Taylor, D. J.; Adler, A. I.; Scanlon, P. H., A simple risk stratification for time to development of sight-threatening diabetic retinopathy. *Diabetes care* **2013,** *36* (3), 580-585.

42. Solomon, S. D.; Chew, E.; Duh, E. J.; Sobrin, L.; Sun, J. K.; VanderBeek, B. L.; Wykoff, C. C.; Gardner, T. W., Diabetic retinopathy: a position statement by the American Diabetes Association. *Diabetes care* **2017,** *40* (3), 412-418.

43. Control, C. f. D.; Prevention, National diabetes fact sheet: national estimates and general information on diabetes and prediabetes in the United States, 2011. *Atlanta, GA: US department of health and human services, centers for disease control and prevention* **2011,** *201* (1), 2568-2569.

44. Dunstan, D. W.; Zimmet, P. Z.; Welborn, T. A.; De Courten, M. P.; Cameron, A. J.; Sicree, R. A.; Dwyer, T.; Colagiuri, S.; Jolley, D.; Knuiman, M., The rising prevalence of diabetes and impaired glucose tolerance: the Australian Diabetes, Obesity and Lifestyle Study. *Diabetes care* **2002,** *25* (5), 829-834.

45. Whittemore, R.; Vilar-Compte, M.; De La Cerda, S.; Marron, D.; Conover, R.; Delvy, R.; Lozano-Marrufo, A.; Perez-Escamilla, R., Challenges to diabetes self-management for adults with type 2 diabetes in low-resource settings in Mexico City: a qualitative descriptive study. *Int J Equity Health* **2019,** *18* (1), 133.

46. Granhall, C.; Sondergaard, F. L.; Thomsen, M.; Anderson, T. W., Pharmacokinetics, Safety and Tolerability of Oral Semaglutide in Subjects with Renal Impairment. *Clin Pharmacokinet* **2018,** *57* (12), 1571-1580.

47. Twarog, C.; Fattah, S.; Heade, J.; Maher, S.; Fattal, E.; Brayden, D. J., Intestinal Permeation Enhancers for Oral Delivery of Macromolecules: A Comparison between Salcaprozate Sodium (SNAC) and Sodium Caprate (C10). *Pharmaceutics* **2019,** *11* (2).

48. Buckley, S. T.; Bækdal, T. A.; Vegge, A.; Maarbjerg, S. J.; Pyke, C.; Ahnfelt-Rønne, J.; Madsen, K. G.; Schéele, S. G.; Alanentalo, T.; Kirk, R. K., Transcellular stomach absorption of a derivatized glucagon-like peptide-1 receptor agonist. *Science translational medicine* **2018,** *10* (467).

49. Brugger, S. D.; Bomar, L.; Lemon, K. P., Commensal-Pathogen Interactions along the Human Nasal Passages. *PLoS Pathog* **2016,** *12* (7), e1005633.

50. Strong, P.; Ito, K.; Murray, J.; Rapeport, G., Current approaches to the discovery of novel inhaled medicines. *Drug Discov Today* **2018,** *23* (10), 1705-1717.

51. Bitter, C.; Suter-Zimmermann, K.; Surber, C., Nasal drug delivery in humans. *Curr Probl Dermatol* **2011,** *40*, 20-35.

52. Duan, X. M., S., New strategies to improve the intranasal absorption of insulin. *Drug Discovery Today* **2010,** *15* (11-12), 416-427.

53. Amidi, M.; Romeijn, S. G.; Borchard, G.; Junginger, H. E.; Hennink, W. E.; Jiskoot, W., Preparation and characterization of protein-loaded N-trimethyl chitosan nanoparticles as nasal delivery system. *J Control Release* **2006,** *111* (1-2), 107-16.

54. Illum, L., Nasal drug delivery—possibilities, problems and solutions. *Journal of Controlled Release* **2003,** *87* (1-3), 187-198.

55. Brown, T. D.; Whitehead, K. A.; Mitragotri, S., Materials for oral delivery of proteins and peptides. *Nature Reviews Materials* **2019,** *5* (2), 127-148.

56. Sélam, J.-L., Inhaled Insulin: Promises and Concerns. *Journal of Diabetes Science and Technology* **2008,** *2* (2), 311-315.

57. Lochhead, J. J.; Kellohen, K. L.; Ronaldson, P. T.; Davis, T. P., Distribution of insulin in trigeminal nerve and brain after intranasal administration. *Scientific reports* **2019,** *9* (1), 1-9.

58. Schmid, V.; Kullmann, S.; Gfrörer, W.; Hund, V.; Hallschmid, M.; Lipp, H. P.; Häring, H. U.; Preissl, H.; Fritsche, A.; Heni, M., Safety of intranasal human insulin: A review. *Diabetes, Obesity and Metabolism* **2018,** *20* (7), 1563-1577.

59. Kim, N. A.; Thapa, R.; Jeong, S. H.; Bae, H.-d.; Maeng, J.; Lee, K.; Park, K., Enhanced intranasal insulin delivery by formulations and tumor protein-derived protein transduction domain as an absorption enhancer. *Journal of Controlled Release* **2019,** *294*, 226-236.

60. Pillion, D. J.; Fyrberg, M. D.; Meezan, E., Nasal absorption of mixtures of fast-acting and long-acting insulins. *International journal of pharmaceutics* **2010,** *388* (1-2), 202-208.

61. Kullmann, S.; Veit, R.; Peter, A.; Pohmann, R.; Scheffler, K.; Häring, H.-U.; Fritsche, A.; Preissl, H.; Heni, M., Dose-dependent effects of intranasal insulin on resting-state brain activity. *The Journal of Clinical Endocrinology & Metabolism* **2018,** *103* (1), 253-262.

62. Shen, D.; Yu, H.; Wang, L.; Khan, A.; Haq, F.; Chen, X.; Huang, Q.; Teng, L., Recent progress in design and preparation of glucose-responsive insulin delivery systems. *Journal of Controlled Release* **2020,** *321*, 236-258.

63. Ross, S. A.; Gulve, E. A.; Wang, M., Chemistry and biochemistry of type 2 diabetes. *Chemical reviews* **2004,** *104* (3), 1255-1282.

64. Aguilar-Bryan, L.; Nichols, C. G.; Wechsler, S. W.; Clement, J. t.; Boyd, A. r.; Gonzalez, G.; Herrera-Sosa, H.; Nguy, K.; Bryan, J.; Nelson, D. A., Cloning of the beta cell high-affinity sulfonylurea receptor: a regulator of insulin secretion. *Science* **1995,** *268* (5209), 423-426.

65. Group, U. P. D. S., UK Prospective Diabetes Study 16: overview of 6 years' therapy of type II diabetes: a progressive disease. *Diabetes* **1995,** *44* (11), 1249-1258.

66. Kahn, S. E.; Haffner, S. M.; Heise, M. A.; Herman, W. H.; Holman, R. R.; Jones, N. P.; Kravitz, B. G.; Lachin, J. M.; O'Neill, M. C.; Zinman, B., Glycemic durability of rosiglitazone, metformin, or glyburide monotherapy. *New England Journal of Medicine* **2006,** *355* (23), 2427-2443.

67. Bennett, W. L.; Maruthur, N. M.; Singh, S.; Segal, J. B.; Wilson, L. M.; Chatterjee, R.; Marinopoulos, S. S.; Puhan, M. A.; Ranasinghe, P.; Block, L., Comparative effectiveness and safety of medications for type 2 diabetes: an update including new drugs and 2-drug combinations. *Annals of internal medicine* **2011,** *154* (9), 602-613.

68. Akiyoshi, M.; Kakei, M.; Nakazaki, M.; Tanaka, H., A new hypoglycemic agent, A-4166, inhibits ATP-sensitive potassium channels in rat pancreatic beta-cells. *American Journal of Physiology-Endocrinology And Metabolism* **1995,** *268* (2), E185-E193.

69. Kahn, S. E.; Montgomery, B.; Howell, W.; Ligueros-Saylan, M.; Hsu, C.-H.; Devineni, D.; McLeod, J. F.; Horowitz, A.; Foley, J. E., Importance of early phase insulin secretion to intravenous glucose tolerance in subjects with type 2 diabetes mellitus. *The Journal of Clinical Endocrinology & Metabolism* **2001,** *86* (12), 5824-5829.

70. Hollander, P. A.; Schwartz, S. L.; Gatlin, M. R.; Haas, S. J.; Zheng, H.; Foley, J. E.; Dunning, B. E., Importance of early insulin secretion: comparison of nateglinide and glyburide in previously diet-treated patients with type 2 diabetes. *Diabetes care* **2001,** *24* (6), 983-988.

71. Group, N. S., Effect of nateglinide on the incidence of diabetes and cardiovascular events. *New England Journal of Medicine* **2010,** *362* (16), 1463-1476.

72. Inzucchi, S. E.; Bergenstal, R. M.; Buse, J. B.; Diamant, M.; Ferrannini, E.; Nauck, M.; Peters, A. L.; Tsapas, A.; Wender, R.; Matthews, D. R., Management of hyperglycemia in type 2 diabetes: a patient-centered approach: position statement of the American Diabetes Association (ADA) and the European Association for the Study of Diabetes (EASD). *Diabetes Spectrum* **2012,** *25* (3), 154-171.

73. Viollet, B.; Guigas, B.; Garcia, N. S.; Leclerc, J.; Foretz, M.; Andreelli, F., Cellular and molecular mechanisms of metformin: an overview. *Clinical science* **2012,** *122* (6), 253-270.

74. Boussageon, R.; Supper, I.; Bejan-Angoulvant, T.; Kellou, N.; Cucherat, M.; Boissel, J.-P.; Kassai, B.; Moreau, A.; Gueyffier, F.; Cornu, C., Reappraisal of metformin efficacy in the treatment of type 2 diabetes: a meta-analysis of randomised controlled trials. *PLoS medicine* **2012,** *9* (4), e1001204.

75. Scheen, A. J.; Paquot, N., Metformin revisited: A critical review of the benefit–risk balance in at-risk patients with type 2 diabetes. *Diabetes & metabolism* **2013,** *39* (3), 179-190.

76. Bischoff, H., The mechanism of alpha-glucosidase inhibition in the management of diabetes. *Clinical and investigative medicine. Medecine clinique et experimentale* **1995,** *18* (4), 303-311.

77. Chiasson, J.-L.; Josse, R. G.; Hunt, J. A.; Palmason, C.; Rodger, N. W.; Ross, S. A.; Ryan, E. A.; Tan, M. H.; Wolever*, T. M., The efficacy of acarbose in the treatment of patients

with non–insulin-dependent diabetes mellitus: A multicenter, controlled clinical trial. *Annals of internal medicine* **1994,** *121* (12), 928-935.

78. Van De Laar, F. A.; Lucassen, P. L.; Akkermans, R. P.; Van De Lisdonk, E. H.; Rutten, G. E.; Van Weel, C., α-Glucosidase inhibitors for patients with type 2 diabetes: results from a Cochrane systematic review and meta-analysis. *Diabetes care* **2005,** *28* (1), 154-163.

79. Holman, R. R.; Cull, C. A.; Turner, R. C., A randomized double-blind trial of acarbose in type 2 diabetes shows improved glycemic control over 3 years (UK Prospective Diabetes Study 44). *Diabetes care* **1999,** *22* (6), 960-964.

80. Yki-Järvinen, H., Thiazolidinediones. *New England Journal of Medicine* **2004,** *351* (11), 1106-1118.

81. Sanyal, A. J.; Chalasani, N.; Kowdley, K. V.; McCullough, A.; Diehl, A. M.; Bass, N. M.; Neuschwander-Tetri, B. A.; Lavine, J. E.; Tonascia, J.; Unalp, A., Pioglitazone, vitamin E, or placebo for nonalcoholic steatohepatitis. *New England Journal of Medicine* **2010,** *362* (18), 1675-1685.

82. Kahn, S. E.; Zinman, B.; Lachin, J. M.; Haffner, S. M.; Herman, W. H.; Holman, R. R.; Kravitz, B. G.; Yu, D.; Heise, M. A.; Aftring, R. P., Rosiglitazone-associated fractures in type 2 diabetes: an Analysis from A Diabetes Outcome Progression Trial (ADOPT). *Diabetes care* **2008,** *31* (5), 845-851.

83. Azoulay, L.; Yin, H.; Filion, K. B.; Assayag, J.; Majdan, A.; Pollak, M. N.; Suissa, S., The use of pioglitazone and the risk of bladder cancer in people with type 2 diabetes: nested case-control study. *Bmj* **2012,** *344*.

84. Rao, V. U.; Alokozai, D.; Voloshko, P.; Schiller, N. B., EFFECT OF THE DUAL PEROXISOME PROLIFERATOR-ACTIVATED RECEPTOR ALPHA/GAMMA AGONIST, MURAGLITAZAR, ON CARDIAC STRUCTURE AND FUNCTION IN TYPE 2 DIABETIC PATIENTS. *Journal of the American College of Cardiology* **2010,** *55* (10S), A157. E1467-A157. E1467.

85. Lee, C.-H.; Olson, P.; Hevener, A.; Mehl, I.; Chong, L.-W.; Olefsky, J. M.; Gonzalez, F. J.; Ham, J.; Kang, H.; Peters, J. M., PPARδ regulates glucose metabolism and insulin sensitivity. *Proceedings of the National Academy of Sciences* **2006,** *103* (9), 3444-3449.

86. Cariou, B.; Hanf, R.; Lambert-Porcheron, S.; Zaïr, Y.; Sauvinet, V.; Noël, B.; Flet, L.; Vidal, H.; Staels, B.; Laville, M., Dual Peroxisome Proliferator–Activated Receptor α/δ agonist GFT505 improves hepatic and peripheral insulin sensitivity in abdominally obese subjects. *Diabetes care* **2013,** *36* (10), 2923-2930.

87. Markowicz-Piasecka, M.; M Huttunen, K.; Mateusiak, L.; Mikiciuk-Olasik, E.; Sikora, J., Is metformin a perfect drug? Updates in pharmacokinetics and pharmacodynamics. *Current pharmaceutical design* **2017,** *23* (17), 2532-2550.

88. Bailey, C. J., Metformin: historical overview. *Diabetologia* **2017,** *60* (9), 1566-1576.

89. Rena, G.; Hardie, D. G.; Pearson, E. R., The mechanisms of action of metformin. *Diabetologia* **2017,** *60* (9), 1577-1585.

90. Abderrahmani, A.; Yengo, L.; Caiazzo, R.; Canouil, M.; Cauchi, S.; Raverdy, V.; Plaisance, V.; Pawlowski, V.; Lobbens, S.; Maillet, J., Increased hepatic PDGF-AA signaling mediates liver insulin resistance in obesity-associated type 2 diabetes. *Diabetes* **2018,** *67* (7), 1310-1321.

91. Dowling, R. J.; Goodwin, P. J.; Stambolic, V., Understanding the benefit of metformin use in cancer treatment. *BMC medicine* **2011,** *9* (1), 1-6.

92. Sharma, S.; Ray, A.; Sadasivam, B., Metformin in COVID-19: a possible role beyond diabetes. *Diabetes research and clinical practice* **2020,** *164*, 108183.

93. Graham, G. G.; Punt, J.; Arora, M.; Day, R. O.; Doogue, M. P.; Duong, J.; Furlong, T. J.; Greenfield, J. R.; Greenup, L. C.; Kirkpatrick, C. M., Clinical pharmacokinetics of metformin. *Clinical pharmacokinetics* **2011,** *50* (2), 81-98.

94. Boldhane, S. P.; Kuchekar, B. S., Gastroretentive drug delivery of metformin hydrochloride: formulation and in vitro evaluation using 32 full factorial design. *Current drug delivery* **2009,** *6* (5), 477-485.

95. Kajbaf, F.; Bennis, Y.; Hurtel-Lemaire, A. S.; Andréjak, M.; Lalau, J. D., Unexpectedly long half-life of metformin elimination in cases of metformin accumulation. *Diabetic Medicine* **2016,** *33* (1), 105-110.

96. DeFronzo, R.; Fleming, G. A.; Chen, K.; Bicsak, T. A., Metformin-associated lactic acidosis: current perspectives on causes and risk. *Metabolism* **2016,** *65* (2), 20-29.

97. Cetin, M.; Sahin, S., Microparticulate and nanoparticulate drug delivery systems for metformin hydrochloride. *Drug delivery* **2016,** *23* (8), 2796-2805.

98. García-Briones, G. S.; Ocampo-Pérez, R.; Gómez-Durán, C. F.; Neri-Gómez, T.; Palestino, G., Porous silicon microcarriers for extended release of metformin: Design, biological evaluation and 3D kinetics modeling. *Chemical Engineering Journal* **2019,** *365*, 415-428.

99. Abdulmalek, S. A.; Balbaa, M., Synergistic effect of nano-selenium and metformin on type 2 diabetic rat model: Diabetic complications alleviation through insulin sensitivity, oxidative mediators and inflammatory markers. *PloS one* **2019,** *14* (8), e0220779.

100. Wang, F.-Z.; Xie, Z.-S.; Xing, L.; Zhang, B.-F.; Zhang, J.-L.; Cui, P.-F.; Qiao, J.-B.; Shi, K.; Cho, C.-S.; Cho, M.-H., Biocompatible polymeric nanocomplexes as an intracellular stimuli-sensitive prodrug for type-2 diabetes combination therapy. *Biomaterials* **2015,** *73*, 149-159.

101. Maestrelli, F.; Mura, P.; González-Rodríguez, M. L.; Cózar-Bernal, M. J.; Rabasco, A. M.; Mannelli, L. D. C.; Ghelardini, C., Calcium alginate microspheres containing metformin hydrochloride niosomes and chitosomes aimed for oral therapy of type 2 diabetes mellitus. *International journal of pharmaceutics* **2017,** *530* (1-2), 430-439.

102. Migdadi, E. M.; Courtenay, A. J.; Tekko, I. A.; McCrudden, M. T.; Kearney, M.-C.; McAlister, E.; McCarthy, H. O.; Donnelly, R. F., Hydrogel-forming microneedles enhance transdermal delivery of metformin hydrochloride. *Journal of controlled release* **2018,** *285*, 142-151.

103. Sushma, M.; Raju, Y. P.; Sundaresan, C. R.; Vandana, K. R.; Kumar, N. V.; Chowdary, V. H., Transmucosal delivery of metformin- a comprehensive study. *Curr Drug Deliv* **2014,** *11* (2), 172-8.

104. Zaykov, A. N.; Mayer, J. P.; DiMarchi, R. D., Pursuit of a perfect insulin. *Nature Reviews Drug Discovery* **2016,** *15* (6), 425-439.

105. Rys, P. M.; Ludwig-Slomczynska, A. H.; Cyganek, K.; Malecki, M. T., Continuous subcutaneous insulin infusion vs multiple daily injections in pregnant women with type 1

diabetes mellitus: a systematic review and meta-analysis of randomised controlled trials and observational studies. *European journal of endocrinology* **2018,** *178* (5), 545-563.

106. Owens, D. R.; Monnier, L.; Barnett, A. H., Future challenges and therapeutic opportunities in type 2 diabetes: C hanging the paradigm of current therapy. *Diabetes, Obesity and Metabolism* **2017,** *19* (10), 1339-1352.

107. Spollett, G.; Edelman, S. V.; Mehner, P.; Walter, C.; Penfornis, A., Improvement of insulin injection technique: examination of current issues and recommendations. *The Diabetes Educator* **2016,** *42* (4), 379-394.

108. Cemeroglu, A. P.; Can, A.; Davis, A. T.; Cemeroglu, O.; Kleis, L.; Daniel, M. S.; Bustraan, J.; Koehler, T. J., Fear of needles in children with type 1 diabetes mellitus on multiple daily injections and continuous subcutaneous insulin infusion. *Endocrine Practice* **2015,** *21* (1), 46-53.

109. Bally, L.; Thabit, H.; Hovorka, R., Finding the right route for insulin delivery–an overview of implantable pump therapy. *Expert opinion on drug delivery* **2017,** *14* (9), 1103-1111.

110. Lenzer, J., Inhaled insulin is approved in Europe and United States. British Medical Journal Publishing Group: 2006.

111. Nazar, H.; Caliceti, P.; Carpenter, B.; El-Mallah, A.; Fatouros, D.; Roldo, M.; Van der Merwe, S.; Tsibouklis, J., A once-a-day dosage form for the delivery of insulin through the nasal route: in vitro assessment and in vivo evaluation. *Biomaterials science* **2013,** *1* (3), 306-314.

112. Hollander, P. A., Evolution of a pulmonary insulin delivery system (Exubera) for patients with diabetes. *Medscape General Medicine* **2007,** *9* (1), 45.

113. Klonoff, D. C., Afrezza inhaled insulin: the fastest-acting FDA-approved insulin on the market has favorable properties. *J Diabetes Sci Technol* **2014,** *8* (6), 1071-3.

114. Han, J.; Zhou, F.; Fei, Y.; Chen, X.; Fu, J.; Qian, H., Preparation and pharmaceutical characterizations of lipidated dimeric Xenopus glucagon-like peptide-1 conjugates. *Bioconjugate chemistry* **2018,** *29* (2), 390-402.

115. Mumuni, M. A.; Kenechukwu, F. C.; Ofokansi, K. C.; Attama, A. A.; Díaz, D. D., Insulin-loaded mucoadhesive nanoparticles based on mucin-chitosan complexes for oral delivery and diabetes treatment. *Carbohydrate polymers* **2020,** *229*, 115506.

116. Grigoras, A. G., Polymer-lipid hybrid systems used as carriers for insulin delivery. *Nanomedicine: Nanotechnology, Biology and Medicine* **2017,** *13* (8), 2425-2437.

117. Czuba, E.; Diop, M.; Mura, C.; Schaschkow, A.; Langlois, A.; Bietiger, W.; Neidl, R.; Virciglio, A.; Auberval, N.; Julien-David, D., Oral insulin delivery, the challenge to increase insulin bioavailability: Influence of surface charge in nanoparticle system. *International journal of pharmaceutics* **2018,** *542* (1-2), 47-55.

118. Lakkireddy, H. R.; Urmann, M.; Besenius, M.; Werner, U.; Haack, T.; Brun, P.; Alié, J.; Illel, B.; Hortala, L.; Vogel, R., Oral delivery of diabetes peptides—Comparing standard formulations incorporating functional excipients and nanotechnologies in the translational context. *Advanced drug delivery reviews* **2016,** *106*, 196-222.

119. Fonte, P.; Araújo, F.; Silva, C.; Pereira, C.; Reis, S.; Santos, H. A.; Sarmento, B., Polymer-based nanoparticles for oral insulin delivery: Revisited approaches. *Biotechnology advances* **2015,** *33* (6), 1342-1354.

120. Bakhru, S. H.; Furtado, S.; Morello, A. P.; Mathiowitz, E., Oral delivery of proteins by biodegradable nanoparticles. *Advanced drug delivery reviews* **2013,** *65* (6), 811-821.

121. Setenay, Ö.; Kerimoğlu, O.; Uğurlu, T., Nanocarriers: novel approaches to oral delivery of insulin. *Clinical and Experimental Health Sciences* **2017,** *7* (3), 115-122.

122. Essa, D.; Kondiah, P. P.; Choonara, Y. E.; Pillay, V., The design of poly (lactide-co-glycolide) nanocarriers for medical applications. *Frontiers in bioengineering and biotechnology* **2020,** *8*, 48.

123. Mohammadpour, F.; Hadizadeh, F.; Tafaghodi, M.; Sadri, K.; Mohammadpour, A. H.; Kalani, M. R.; Gholami, L.; Mahmoudi, A.; Chamani, J., Preparation, in vitro and in vivo evaluation of PLGA/Chitosan based nano-complex as a novel insulin delivery formulation. *International journal of pharmaceutics* **2019,** *572*, 118710.

124. Wang, M.; Yao, P.; Gao, M.; Jin, J.; Yu, Y., Novel fatty chain-modified GLP-1R G-protein biased agonist exerts prolonged anti-diabetic effects through targeting receptor binding sites. *RSC Advances* **2020,** *10* (14), 8044-8053.

125. Shan, W.; Zhu, X.; Liu, M.; Li, L.; Zhong, J.; Sun, W.; Zhang, Z.; Huang, Y., Overcoming the diffusion barrier of mucus and absorption barrier of epithelium by self-assembled nanoparticles for oral delivery of insulin. *ACS nano* **2015,** *9* (3), 2345-2356.

126. Shan, W.; Zhu, X.; Tao, W.; Cui, Y.; Liu, M.; Wu, L.; Li, L.; Zheng, Y.; Huang, Y., Enhanced oral delivery of protein drugs using zwitterion-functionalized nanoparticles to overcome both the diffusion and absorption barriers. *ACS applied materials & interfaces* **2016,** *8* (38), 25444-25453.

127. Wu, J.; Zheng, Y.; Liu, M.; Shan, W.; Zhang, Z.; Huang, Y., Biomimetic viruslike and charge reversible nanoparticles to sequentially overcome mucus and epithelial barriers for oral insulin delivery. *ACS applied materials & interfaces* **2018,** *10* (12), 9916-9928.

128. Wang, A.; Yang, T.; Fan, W.; Yang, Y.; Zhu, Q.; Guo, S.; Zhu, C.; Yuan, Y.; Zhang, T.; Gan, Y., Protein corona liposomes achieve efficient oral insulin delivery by overcoming mucus and epithelial barriers. *Advanced healthcare materials* **2019,** *8* (12), 1801123.

129. Cheng, H.; Zhang, X.; Qin, L.; Huo, Y.; Cui, Z.; Liu, C.; Sun, Y.; Guan, J.; Mao, S., Design of self-polymerized insulin loaded poly (n-butylcyanoacrylate) nanoparticles for tunable oral delivery. *Journal of Controlled Release* **2020,** *321*, 641-653.

130. Liu, L.; Zhang, Y.; Yu, S.; Zhang, Z.; He, C.; Chen, X., pH-and amylase-responsive carboxymethyl starch/poly (2-isobutyl-acrylic acid) hybrid microgels as effective enteric carriers for oral insulin delivery. *Biomacromolecules* **2018,** *19* (6), 2123-2136.

131. Banerjee, A.; Chen, R.; Arafin, S.; Mitragotri, S., Intestinal iontophoresis from mucoadhesive patches: a strategy for oral delivery. *Journal of Controlled Release* **2019,** *297*, 71-78.

132. Banerjee, A.; Ibsen, K.; Brown, T.; Chen, R.; Agatemor, C.; Mitragotri, S., Ionic liquids for oral insulin delivery. *Proceedings of the National Academy of Sciences* **2018,** *115* (28), 7296-7301.

133. Abramson, A.; Caffarel-Salvador, E.; Soares, V.; Minahan, D.; Tian, R. Y.; Lu, X.; Dellal, D.; Gao, Y.; Kim, S.; Wainer, J., A luminal unfolding microneedle injector for oral delivery of macromolecules. *Nature medicine* **2019,** *25* (10), 1512-1518.

134. Abramson, A.; Caffarel-Salvador, E.; Khang, M.; Dellal, D.; Silverstein, D.; Gao, Y.; Frederiksen, M. R.; Vegge, A.; Hubálek, F.; Water, J. J., An ingestible self-orienting system for oral delivery of macromolecules. *Science* **2019,** *363* (6427), 611-615.

135. Gandhi, R. B.; Robinson, J. R., Bioadhesion in drug delivery. *Indian Journal of Pharmaceutical Sciences* **1988,** *50* (3), 145.

136. Kajdič, S.; Planinšek, O.; Gašperlin, M.; Kocbek, P., Electrospun nanofibers for customized drug-delivery systems. *Journal of Drug Delivery Science and Technology* **2019,** *51*, 672-681.

137. Perez-Gonzalez, G. L.; Villarreal-Gomez, L. J.; Serrano-Medina, A.; Torres-Martinez, E. J.; Cornejo-Bravo, J. M., Mucoadhesive electrospun nanofibers for drug delivery systems: applications of polymers and the parameters' roles. *Int J Nanomedicine* **2019,** *14*, 5271-5285.

138. Nalbandian, M. J.-C., *Development and optimization of chemically-active electrospun nanofibers for treatment of impaired water sources*. University of California, Riverside: 2014.

139. Sharma, A.; Gupta, A.; Rath, G.; Goyal, A.; Mathur, R. B.; Dhakate, S. R., Electrospun composite nanofiber-based transmucosal patch for anti-diabetic drug delivery. *J Mater Chem B* **2013,** *1* (27), 3410-3418.

140. Harris, D.; Robinson, J. R., Drug delivery via the mucous membranes of the oral cavity. *Journal of pharmaceutical sciences* **1992,** *81* (1), 1-10.

141. Gandhi, R. B.; Robinson, J. R., Oral cavity as a site for bioadhesive drug delivery. *Advanced drug delivery reviews* **1994,** *13* (1-2), 43-74.

142. Hosny, E.; Elkheshen, S.; Saleh, S., Buccoadhesive tablets for insulin delivery: in-vitro and in-vivo studies. *Bollettino chimico farmaceutico* **2002,** *141* (3), 210-217.

143. Giovino, C.; Ayensu, I.; Tetteh, J.; Boateng, J. S., An integrated buccal delivery system combining chitosan films impregnated with peptide loaded PEG-b-PLA nanoparticles. *Colloids and Surfaces B: Biointerfaces* **2013,** *112*, 9-15.

144. Zhang, H.; Zhang, J.; Streisand, J. B., Oral Mucosal Drug DeliveryClinical Pharmacokinetics and Therapeutic ApplicationsHao Zhang,1 Jie Zhang2and James B. Streisand. *Clin. Pharmacokinet.* **2002,** *41*, 661-680.

145. Shaikh, R.; Singh, T. R. R.; Garland, M. J.; Woolfson, A. D.; Donnelly, R. F., Mucoadhesive drug delivery systems. *J. Pharm. Bioallied. Sci.* **2011,** *3*, 89–100.

146. Mortazavian, E.; Dorkoosh, F. A.; Rafiee-Tehrani, M., Design, characterization and ex vivo evaluation of chitosan film integrating of insulin nanoparticles composed of thiolated chitosan derivative for buccal delivery of insulin. *Drug Dev Ind Pharm* **2014,** *40* (5), 691-8.

147. Ramadon, D.; McCrudden, M. T. C.; Courtenay, A. J.; Donnelly, R. F., Enhancement strategies for transdermal drug delivery systems: current trends and applications. *Drug Deliv Transl Res* **2021**.

148. Sattar, M.; Sayed, O. M.; Lane, M. E., Oral transmucosal drug delivery–current status and future prospects. *International journal of pharmaceutics* **2014,** *471* (1-2), 498-506.

149. Rastogi, V.; Yadav, P., Transdermal drug delivery system: An overview. *Asian Journal of Pharmaceutics (AJP): Free full text articles from Asian J Pharm* **2014,** *6* (3).

150. Siepmann, J.; Siepmann, F., Sink conditions do not guarantee the absence of saturation effects. *International journal of pharmaceutics* **2020,** *577*, 119009.

151. Jijie, R.; Barras, A.; Boukherroub, R.; Szunerits, S., Nanomaterials for transdermal drug delivery: beyond the state of the art of liposomal structures. *J. Mater. Chem. B* **2017,** *5* (44), 8653-8675.

152. Park, J.; Lee, H.; Lim, G.-S.; Kim, N.; Kim, D.; Kim, Y.-C., Enhanced transdermal drug delivery by sonophoresis and simultaneous application of sonophoresis and iontophoresis. *AAPS PharmSciTech* **2019,** *20* (3), 1-7.

153. Prausnitz, M. R.; Lau, B. S.; Milano, C. D.; Conner, S.; Langer, R.; Weaver, J. C., A quantitative study of electroporation showing a plateau in net molecular transport. *Biophysical journal* **1993,** *65* (1), 414-422.

154. Gangarosa Sr, L.; Hill, J. M., Modern iontophoresis for local drug delivery. *International journal of pharmaceutics* **1995,** *123* (2), 159-171.

155. Kassan, D. G.; Lynch, A. M.; Stiller, M. J., Physical enhancement of dermatologic drug delivery: iontophoresis and phonophoresis. *Journal of the American Academy of Dermatology* **1996,** *34* (4), 657-666.

156. Dhote, V.; Bhatnagar, P.; Mishra, P. K.; Mahajan, S. C.; Mishra, D. K., Iontophoresis: a potential emergence of a transdermal drug delivery system. *Scientia pharmaceutica* **2012,** *80* (1), 1-28.

157. Gross, J.; Kelly, J. G., Intradermal drug delivery device and method for intradermal delivery of drugs. Google Patents: 1996.

158. Jang, K. K., Skin perforating device for transdermal medication. Google Patents: 1997.

159. Jurčíček, P.; Zou, H.; Zhang, S.; Liu, C., Design and fabrication of hollow out-of-plane silicon microneedles. *Micro & Nano Letters* **2013,** *8* (2), 78-81.

160. Cormier, M.; Johnson, B.; Ameri, M.; Nyam, K.; Libiran, L.; Zhang, D. D.; Daddona, P., Transdermal delivery of desmopressin using a coated microneedle array patch system. *Journal of controlled release* **2004,** *97* (3), 503-511.

161. Vora, L. K.; Courtenay, A. J.; Tekko, I. A.; Larrañeta, E.; Donnelly, R. F., Pullulan-based dissolving microneedle arrays for enhanced transdermal delivery of small and large biomolecules. *International journal of biological macromolecules* **2020,** *146*, 290-298.

162. Rodgers, A. M.; McCrudden, M. T.; Vincente-Perez, E. M.; Dubois, A. V.; Ingram, R. J.; Larrañeta, E.; Kissenpfennig, A.; Donnelly, R. F., Design and characterisation of a dissolving microneedle patch for intradermal vaccination with heat-inactivated bacteria: A proof of concept study. *International journal of pharmaceutics* **2018,** *549* (1-2), 87-95.

163. Courtenay, A. J.; McCrudden, M. T.; McAvoy, K. J.; McCarthy, H. O.; Donnelly, R. F., Microneedle-mediated transdermal delivery of bevacizumab. *Molecular pharmaceutics* **2018,** *15* (8), 3545-3556.

164. Courtenay, A. J.; Rodgers, A. M.; McCrudden, M. T.; McCarthy, H. O.; Donnelly, R. F., Novel hydrogel-forming microneedle array for intradermal vaccination in mice using ovalbumin as a model protein antigen. *Molecular pharmaceutics* **2018,** *16* (1), 118-127.

165. McAllister, D. V.; Wang, P. M.; Davis, S. P.; Park, J.-H.; Canatella, P. J.; Allen, M. G.; Prausnitz, M. R., Microfabricated needles for transdermal delivery of macromolecules and nanoparticles: fabrication methods and transport studies. *Proceedings of the National Academy of Sciences* **2003,** *100* (24), 13755-13760.

166. Henry, S.; McAllister, D. V.; Allen, M. G.; Prausnitz, M. R., Microfabricated microneedles: a novel approach to transdermal drug delivery. *Journal of pharmaceutical sciences* **1998,** *87* (8), 922-925.

167. Park, J.-H.; Allen, M. G.; Prausnitz, M. R., Biodegradable polymer microneedles: fabrication, mechanics and transdermal drug delivery. *Journal of controlled release* **2005,** *104* (1), 51-66.

168. Ross, S.; Scoutaris, N.; Lamprou, D.; Mallinson, D.; Douroumis, D., Inkjet printing of insulin microneedles for transdermal delivery. *Drug delivery and translational research* **2015,** *5* (4), 451-461.

169. Mc Crudden, M. T.; Larrañeta, E.; Clark, A.; Jarrahian, C.; Rein-Weston, A.; Lachau-Durand, S.; Niemeijer, N.; Williams, P.; Haeck, C.; McCarthy, H. O., Design, formulation and evaluation of novel dissolving microarray patches containing a long-acting rilpivirine nanosuspension. *Journal of Controlled Release* **2018,** *292*, 119-129.

170. Leone, M.; Priester, M. I.; Romeijn, S.; Nejadnik, M. R.; Mönkäre, J.; O'Mahony, C.; Jiskoot, W.; Kersten, G.; Bouwstra, J. A., Hyaluronan-based dissolving microneedles with high antigen content for intradermal vaccination: Formulation, physicochemical characterization and immunogenicity assessment. *European journal of pharmaceutics and biopharmaceutics* **2019,** *134*, 49-59.

171. Chen, X.; Wang, L.; Yu, H.; Li, C.; Feng, J.; Haq, F.; Khan, A.; Khan, R. U., Preparation, properties and challenges of the microneedles-based insulin delivery system. *Journal of Controlled Release* **2018,** *288*, 173-188.

172. Demir, Y. K.; Akan, Z.; Kerimoglu, O., Characterization of polymeric microneedle arrays for transdermal drug delivery. *PloS one* **2013,** *8* (10), e77289.

173. Hardy, J. G.; Larrañeta, E.; Donnelly, R. F.; McGoldrick, N.; Migalska, K.; McCrudden, M. T.; Irwin, N. J.; Donnelly, L.; McCoy, C. P., Hydrogel-forming microneedle arrays made from light-responsive materials for on-demand transdermal drug delivery. *Molecular pharmaceutics* **2016,** *13* (3), 907-914.

174. Ramöller, I. K.; McAlister, E.; Bogan, A.; Cordeiro, A. S.; Donnelly, R. F., Novel design approaches in the fabrication of polymeric microarray patches via micromoulding. *Micromachines* **2020,** *11* (6), 554.

175. Kearney, M.-C.; Caffarel-Salvador, E.; Fallows, S. J.; McCarthy, H. O.; Donnelly, R. F., Microneedle-mediated delivery of donepezil: potential for improved treatment options in Alzheimer's disease. *European Journal of Pharmaceutics and Biopharmaceutics* **2016,** *103*, 43-50.

176. Chih-Hung Lin, I. A. A. J.-Y. F., Lasers as an approach for promoting drug delivery via skin. *Expert Opin Drug Deliv* **2014,** *11* (4), 599-614.

177. Szunerits, S.; Boukherroub, R., Heat: A Highly Efficient Skin Enhancer for Transdermal Drug Delivery. *Front. Bioeng. Biotechnol.* **2018,** *6*, 15.

178. Park, S.; An, J.; Jung, I.; Piner, R. D.; An, S. J.; Li, X.; Velamakanni, A.; Ruoff, R. S., Colloidal suspensions of highly reduced graphene oxide in a wide variety of organic solvents. *Nano letters* **2009,** *9* (4), 1593-1597.

179. Markovic, Z. M.; Harhaji-Trajkovic, L. M.; Todorovic-Markovic, B. M.; Kepić, D. P.; Arsikin, K. M.; Jovanović, S. P.; Pantovic, A. C.; Dramićanin, M. D.; Trajkovic, V. S., In vitro

comparison of the photothermal anticancer activity of graphene nanoparticles and carbon nanotubes. *Biomaterials* **2011,** *32* (4), 1121-1129.

180. Teodorescu, F.; Oz, Y.; Queniat, G.; Abderrahmani, A.; Foulon, C.; Lecoeur, M.; Sanyal, R.; Sanyal, A.; Boukherroub, R.; Szunerits, S., Photothermally triggered on-demand insulin release from reduced graphene oxide modified hydrogels. *J. Control Release* **2017,** *246*, 164-173.

181. Brown, E. R., Fundamentals of Lasers and Light Devices in Dermatology. In *Practical Introduction to Laser Dermatology*, Springer: 2020; pp 1-52.

182. Plastiras, O.-E.; Deliyanni, E.; Samanidou, V., Applications of Graphene-Based Nanomaterials in Environmental Analysis. *Applied Sciences* **2021,** *11* (7), 3028.

183. Marzban, L.; Park, K.; Verchere, C. B., Islet amyloid polypeptide and type 2 diabetes. *Experimental gerontology* **2003,** *38* (4), 347-351.

184. Asthana, S.; Mallick, B.; Alexandrescu, A. T.; Jha, S., IAPP in type II diabetes: Basic research on structure, molecular interactions, and disease mechanisms suggests potential intervention strategies. *Biochimica et Biophysica Acta (BBA)-Biomembranes* **2018,** *1860* (9), 1765-1782.

185. Ke, P. C.; Sani, M.-A.; Ding, F.; Kakinen, A.; Javed, I.; Separovic, F.; Davis, T. P.; Mezzenga, R., Implications of peptide assemblies in amyloid diseases. *Chemical Society Reviews* **2017,** *46* (21), 6492-6531.

186. Cheng, B.; Gong, H.; Xiao, H.; Petersen, R. B.; Zheng, L.; Huang, K., Inhibiting toxic aggregation of amyloidogenic proteins: a therapeutic strategy for protein misfolding diseases. *Biochimica et Biophysica Acta (BBA)-General Subjects* **2013,** *1830* (10), 4860-4871.

187. Asthana, S.; Mallick, B.; Alexandrescu, A. T.; Jha, S., IAPP in type II diabetes: Basic research on structure, molecular interactions, and disease mechanisms suggests potential intervention strategies. *Biochim Biophys Acta Biomembr* **2018**.

188. Mishra, R.; Bulic, B.; Sellin, D.; Jha, S.; Waldmann, H.; Winter, R., Small-molecule inhibitors of islet amyloid polypeptide fibril formation. *Angewandte Chemie* **2008,** *120* (25), 4757-4760.

189. Jeong, K.; Chung, W. Y.; Kye, Y.-S.; Kim, D., Cu (II) cyclen cleavage agent for human islet amyloid peptide. *Bioorganic & medicinal chemistry* **2010,** *18* (7), 2598-2601.

190. Zhang, M.; Mao, X.; Yu, Y.; Wang, C. X.; Yang, Y. L.; Wang, C., Nanomaterials for reducing amyloid cytotoxicity. *Advanced materials* **2013,** *25* (28), 3780-3801.

191. Li, Q.; Liu, L.; Zhang, S.; Xu, M.; Wang, X.; Wang, C.; Besenbacher, F.; Dong, M., Modulating Aβ33–42 peptide assembly by graphene oxide. *Chemistry–A European Journal* **2014,** *20* (24), 7236-7240.

192. Koppel, K.; Tang, H.; Javed, I.; Parsa, M.; Mortimer, M.; Davis, T. P.; Lin, S.; Chaffee, A. L.; Ding, F.; Ke, P. C., Elevated amyloidoses of human IAPP and amyloid beta by lipopolysaccharide and their mitigation by carbon quantum dots. *Nanoscale* **2020,** *12* (23), 12317-12328.

193. Celebioglu, A.; Uyar, T., Hydrocortisone/cyclodextrin complex electrospun nanofibers for a fast-dissolving oral drug delivery system. *RSC Med Chem* **2020,** *11* (2), 245-258.

194. Huang, C.; Soenen, S. J.; Rejman, J.; Lucas, B.; Braeckmans, K.; Demeester, J.; De Smedt, S. C., Stimuli-responsive electrospun fibers and their applications. *Chem Soc Rev* **2011,** *40* (5), 2417-34.

195. Li, L.; Hsieh, Y.-L., Ultra-fine polyelectrolyte fibers from electrospinning of poly(acrylic acid). *Polymer* **2005,** *46* (14), 5133-5139.

196. Topuz, F.; Uyar, T., Electrospinning of Cyclodextrin Functional Nanofibers for Drug Delivery Applications. *Pharmaceutics* **2018,** *11* (1).

197. Xue, J.; Wu, T.; Dai, Y.; Xia, Y., Electrospinning and Electrospun Nanofibers: Methods, Materials, and Applications. *Chem Rev* **2019,** *119* (8), 5298-5415.

198. Ning, Y.; Shen, W.; Ao, F., Application of blocking and immobilization of electrospun fiber in the biomedical field. *RSC Advances* **2020,** *10* (61), 37246-37265.

199. Patel, V. F.; Fang, L.; Brown, M. B., Advances in oral transmucosal drug delivery. *J. Control. Release* **2020,** *153*, 106-116.

200. Altinbasak, I.; Jijie, R.; Barras, A.; Golba, B.; Sanyal, R.; Bouckaert, J.; Drider, D.; Bilyy, R.; Dumych, T.; Paryzhak, S.; Vovk, V.; Boukherroub, R.; Sanyal, A.; Szunerits, S., Reduced Graphene Oxide Embedded Polymeric Nanofiber Mats: An 'On-Demand' Photothermally-Triggered Antibiotic Release Platform *ACS Appl. Mater. Interfaces* **2018,** *10*, 41098-41106.

201. Illangakoon, U. E.; Gill, H.; Sherman, G. C.; Parhizkar, M.; S., M.; Chatterton, N. P.; Williams, G. R., Fast dissolving paracetamol/caffeine nanofibers prepared by electrosphinning. *Int. J. Pharm.* **2014,** *477*, 369-379.

202. Li, L.; Hsieh, Y.-L., Ultra-fine polyelectrolyte fibers from electrospinning of poly(acrylic acid). *Polymer* **2005,** *46*, 5133-5139.

203. Fonseca, D. F. S.; Costa, P. C.; Almeida, I. F.; Dias-Pereira, P.; Correia-Sa, I.; Bastos, V.; Oliveira, H.; Duarte-Araujo, M.; Morato, M.; Vilel, C.; Silvestr, A. J. D.; Freire, C. S. R., Pullulan Microneedle Pathces for the efficient *Carbohydr. Polym.* **2020,** *241*, 116314.

204. Vaidyaa, A.; Mitragotri, S., Ionic liquid-mediated delivery of insulin to buccal mucosa. *J. Control. Release* **2020,** *327*, 26.

205. Park, H.; Robinson, J. R., Mechanisms of mucoadhesion of poly (acrylic acid) hydrogels. *Pharmaceutical research* **1987,** *4* (6), 457-464.

206. Cook, S. L.; Bull, S. P.; Methven, L.; Parker, J. K.; Khutoryanskiy, V. V., Mucoadhesion: A food perspective. *Food Hydrocolloids* **2017,** *72*, 281-296.

207. Wright, A. K.; Kontopantelis, E.; Emsley, R.; Buchan, I.; Sattar, N.; Rutter, M. K.; Ashcroft, D. M., Life Expectancy and Cause-Specific Mortality in Type 2 Diabetes: A Population-Based Cohort Study Quantifying Relationships in Ethnic Subgroups. *Diabetes Care* **2017,** *40*, 338–345.

208. Pagneux, Q.; Ye, R.; Li, C.; Barras, A.; Hennuyer, N.; Staels, B.; Caina, D.; Avila Osses, J. I.; Abderrahmani, A.; Plaisance, V.; Pawlowski, V.; Boukherroub, R.; Melinte, S.; Szunerits, S., Electrothermal patches driving the transdermal delivery of insulin. *Nanoscale Horizon* **2020,** *5*, 663-670

209. Teodorescu, F.; Oz , Y.; Quéniat, G.; Abderrahmani, A.; Foulon, C.; Lecoeur, M.; Sanyal, R.; Sanyal, A.; Boukherroub, R.; Szunerits, S., Photothermally triggered on-demand

insulin release from reduced graphene oxide modified hydrogels. *J. Control. Release* **2017,** *246*, 164-173.

210. Thirion-Delalande, C.; Gervais, F.; Fisch, C.; Cuiné, J.; Baron-Bodo, V.; Moingeon, P.; Mascarell, L., Comparative analysis of the oral mucosae from rodents and non-rodents: Application to the nonclinical evaluation of sublingual immunotherapy products. *PLOS One* **2017,** *12*, e0183398.

211. Pinto, S.; Pintado, M. E.; Sarmento, B., In vivo,ex vivo and in vitro assessment of buccal permeation of drugs from delivery systems, . *Expert Opin. Drug Deliv.* **2020,** *17*, 33-48.

212. Pillai, O.; Panchagnula, R., *J. Control. Release* **2003,** *89*, 127.

213. Jin, X.; Zhu, D. D.; Chen, B. Z.; Ashfaq, M.; Guo, X. D., Insulin delivery systems combined with microneedle technology. *Adv Drug Deliv Rev* **2018,** *127*, 119-137.

214. Chen, S.; Matsumoto, H.; Moro-oka, Y.; Tanaka, M.; Miyahara, Y.; Suganami, T.; Matsumoto, A., Microneedle-Array Patch Fabricated with Enzyme-Free Polymeric Components Capable of On-Demand Insulin Delivery. *Advanced Functional Materials* **2018,** *29* (7), 1807369.

215. Kirkby, M.; Hutton, A. R. J.; Donnelly, R. F., Microneedle Mediated Transdermal Delivery of Protein, Peptide and Antibody Based Therapeutics: Current Status and Future Considerations. *Pharm Res* **2020,** *37* (6), 117.

216. Azmana, M.; Mahmood, S.; Hilles, A. R.; Mandal, U. K.; Saeed Al-Japairai, K. A.; Raman, S., Transdermal drug delivery system through polymeric microneedle: A recent update. *Journal of Drug Delivery Science and Technology* **2020,** *60*, 101877.

217. Liu, T.; Luo, G.; Xing, M.; Tengfei Liu, G. L., Malcolm Xing, Biomedical Applications of Polymeric Microneedles for Transdermal Therapeutic Delivery and Diagnosis: Current Status and Future Perspectives. *Adv. Therap.* **20202018,** *3* (9), 900140.

218. Seong, K.-Y.; Se, M.-S.; Hwang, D. Y.; O'Cearbhaill, E. D.; Sreenan, S.; Karp, J. M.; Yang, S. Y., A self-adherent, bullet-shaped microneedle patch for controlled transdermal delivery of insulin. *J. Control Release* **2017,** *265*, 48-56.

219. Zhang, Y.; Jiang, G.; Yu, W.; Liu, D.; Xu, B., Microneedles fabricated from alginate and maltose for transdermal delivery of insulin on diabetic rats

Mater Sci Eng C Mater Biol Appl **2018,** *85*, 18-26.

220. Zhuang, J.; Rao, F.; Wu, D.; Huang, Y.; Xu, H.; Gao, W.; Zhang, J.; Sun, J., Study on the fabrication and characterization of tip-loaded dissolving microneedles for transdermal drug delivery. *Eur. J. Pharma. Biopharm.* **2020,** *157*, 66-73.

221. Lee, J. W.; Han, M.-R.; Park, J.-H., Polymer microneedles for transdermal drug delivery. *J. Drug Target* **2013,** *21*, 211-223.

222. Kim, S.; Yang, H.; Eum, J.; Ma, Y.; Lahiji, S. F.; Jung, H., Implantable powder-carrying microneedles for transdermal delivery of high-dose insulin with enhanced activity. *Biomaterials* **2020,** *232*, 119733.

223. Chen, M.-C.; Ling, M.-H.; Wang, K.-W.; Lin, Z.-W.; Lai, B.-H.; Chen, D.-H., Near-infrared light-responsive composite microneedles for on-demand transdermal drug delivery. *Biomacromol.* **2015,** *16* (5), 1598-1607.

224. Azmana, M.; Mahmood, S.; Hilles, A. R.; Mandal, U. K.; Saeed Al-Japairai, K. A. S.; Raman, S., Transdermal drug dleiveyr system though polymeric microneele: A recent update. *J. Drug. Del. Sci. Technol.* **2020,** *60*, 101877.

225. Yadav, P. R.; Munni, M. N.; Campbell, L.; Mostofa, G.; Dobson, L.; Shittu, M.; Pattanayek, S. K.; Uddin, M. J.; Das, D. B., Translation of Polymeric Microneedles for Treatment of Human Diseases: Recent Trends, Progress, and Challenges. *Paramaceutics* **2021,** *13*, 1132.

226. Chen, S.; Matsumoto, H.; Moro-oka, Y.; Tanaka, M.; Miyahara, Y.; Suganami, T.; Matsumoto, A., Microneedle-Array Patch Fabricated with Enzyme-Free Polymeric Components Capable of On-Demand Insulin Delivery. *Adv. Funct. Mater.* **2018,** *29*, 1807369.

227. Wang, S.; Zhu, M.; Zhao, L.; Kuang, D.; Kundu, S. C.; Lu, S., Insulin-Loaded Silk Fibroin Microneedles as Sustained Release System. *ACS Biomater. Sci. Eng.* **2019,** *5* (4), 1887-1894.

228. Zhu, M.; Liu, Y.; Jiang, F.; Cao, J.; Kundu, S. C.; Lu, S., Combined Silk Fibroin Microneedles for Insulin Delivery. *ACS Biomater. Sci. Eng.* **2020,** *6*, 3422-3429.

229. Chen, S.; Matsumoto, H.; Moro-oka, Y.; Tanaka, M.; Miyahara, Y.; Suganami, T.; Matsumoto, A., Smart Microneedle Fabricated with Silk Fibroin Combined Semi-interpenetrating Network Hydrogel for Glucose-Responsive Insulin Delivery. *ACS Biomater. Sci. Eng.* **2019,** *5* (11), 5781–5789.

230. Migdadi, E. M.; Courtenay, A. J.; Ismaiel A Tekko, I. A.; McCrudden, M. T. C.; Kearney, M.-C.; McAlister, E.; McCarthy, H. O.; Donnelly, R. F., Hydrogel-forming microneedles enhance transdermal delivery of metformin hydrochloride. *J. Control Release* **2018,** *285*, 142-151.

231. Donnelly, R. F.; Singh, T. R. R.; Garland, M. J.; Migalska, K.; Majithiya, R.; McCrudden, C. M.; Laxman Kole, P. L.; Mahmood, T. M. T.; McCarthy, H. O.; Woolfson, A. D., Hydrogel-Forming Microneedle Arrays for Enhanced Transdermal Drug Delivery. *Adv. Funct. Mater.* **2012,** *22*, 4879.

232. Kim, H.; Lee, H.; Seong, K.-Y.; Lee, E.; Yang, S. Y.; Yoon, J., Visible Light-Triggered On-Demand Drug Release from Hybrid Hydrogels and its Application in Transdermal Patches. *Adv. Healthc. Mater.* **2015,** *4* (14), 2071-2077.

233. Donnelly, R. F.; McCrudden, C. M.; Aklkilani, A. Z.; Larrañeta, E.; McAlister, E.; Courtenay, A. J.; Kearney, M.-C.; Sing, T. R. R.; McCarthy, H. O.; Kett, V. L.; Caffarel-Salvador , E.; Al-Zahrani , S.; Woolfson, A. D., Hydrogel-forming microneedles prepared from "super swelling" polymers combined with lyophilised wafers for transdermal drug delivery. *PLoS One* **2014,** *9*, 111547.

234. Hardy, J. G.; Eneko Larrañeta, E.; Donnelly, R. F.; McGoldrick, N.; Migalska, K.; McCrudden, M. T. C.; Donnely, L.; McCoy, C. P., Hydrogel-forming microneedle arrays made from stimuli-responsive materials for on- demand drug delivery. . *Mol. Pharamceutics* **2016,** *13*, 907-914.

235. Chen, B. Z.; Zhang, L. Q.; Xia, Y. Y.; Zhang, X. P.; Guo, X. D., A basal-bolus insulin regimen integrated microneedle patch for intraday postprandial glucose control. *Sci. Adv.* **2020,** *6*, eaba7260.

236. Davis, S. P.; Martanto, W.; Allen, M. G.; Prausnitz, M. R., Hollow metal microneedles for insulin delivery to diabetic rats. *IEEE Trans. Biomed. Eng.* **2005,** *52* (5), 909.

237. Zhao, X.; Lang, Q.; Yildirimer, L.; Lin, Z. Y.; Cui, W.; Annabi, N.; Ng, K. W.; Dokmeci, M. R.; Ghaemmaghami, A. M.; Khademhosseini, A., Photocrosslinkable gelatin hydrogel for epidermal tissue engineering. *Adv. Healthc. Mater.* **2016,** *5*, 108–118.

238. Sutter, M.; Siepmann, J. H., W.E.; Jiskoot, W. , Recombinant gelatin hydrogels for the sustained release of proteins. *J. Control. Release* **2007,** *119*.

239. Chou, S. S.; Kaehr, B.; Kim, J.; Foley, B. M.; De, M.; Hopkins, P. E.; Huang, J.; Brinker, C. J.; Dravid, V. P., Chemically Exfoliated MoS_2 as Near-Infrared Photothermal Agents. *Angew. Chem. Int. Ed. Engl.* **2013,** *52*, 4160–4164

240. Yin, W.; Yu, J.; Lv, F.; Yan, L.; Zheng, L. R.; Gu, Z.; Zhao, Y., Functionalized Nano-MoS_2 with peroxidase catalytic and near-infrared photothermal activities for safe and synergetic wound antibacterial applications. *ACS Nano* **2016,** *10*, 11000–11011.

241. Park, C. H.; Kim, T.; Lee, G. H.; Ku, K. H.; Kim, S.-H.; Kim, B. J., Fluorescent Polymer-MoS_2-Embedded Microgels for Photothermal Heating and Colorimetric Monitoring. *ACS Appl. Mater. Interfaces* **2020,** *12*, 35415–35423.

242. Chen, Y. C.; Yang, Y.; Xian, Y.; Singh, P. F., J.; Cui, S.; Carrier, A.; Oakes, K.; Luan, T.; Zhang, X., Multifunctional Graphene-Oxide-Reinforced Dissolvable Polymeric Microneedles for Transdermal Drug Delivery. *ACS Appl. Mater. Interfaces* **2020,** *12*, 352-360.

243. Koheler, F. M.; Jacobsen, A.; Ohn, T.; Ensslin, K.; Stark, W. J., Chemical modification of graphene characterized by Raman and transport experiments. *Nanoscale* **2012,** *4*, 3781.

244. Altinbasak, I.; Jijie, R.; Barras, A.; Golba, B.; Sanyal, R.; Bouckaert, J.; Drider, D.; Bilyy, R.; Dumych, T.; Paryzhak, S.; Vovk, V.; Boukherroub, R.; Sanyal, A.; Szunerits, S., Reduced Graphene Oxide Embedded PolymericNanofiber Mats: An 'On-Demand'Photothermally-Triggered Antibiotic Release Platform. *ACS Appl. Mater. Interfaces* **2018,** *10* (48), 41098-41106.

245. Tsang, D. K. H.; Lieberthal, T. J.; Watts, C.; Dunlop, I. E.; Ramadan, S.; del Rio Hernandez, A. E.; Klein, N., Chemically Functionalised Graphene FET Biosensor for the Label-free Sensing of Exosomes. *Sci. Rpt.* **2019,** *9*, 13946.

246. Oz, Y.; Barras, A.; Sanyal, R.; Boukherorub, R.; Szunerits, S.; Sanyal, A., unctionalization of Reduced Graphene Oxide viaThiol–Maleimide "Click" Chemistry: Facile Fabricationof Targeted Drug Delivery Vehicles. *ACS Appl. Mater. Interfaces* **2017,** *9*, 34194 - 34203.

247. Teodorescu, F.; Oz, Y.; Quéniat, G.; Abderrahmani, A.; Foulon, C.; Lecoeur, M.; anyal, R.; Sanyal, A.; Boukherroub, R.; Szunerits, S., Photothermally triggered on-demand insulin release from reduced graphene oxide modified hydrogels. *J. Control. Release* **2017**.

248. Xiao, M.; Wei, S.; Li, Y.; Jasensky, J.; Chen, J.; Brooks, C. L.; Chen, Z., Molecular interactions between single layered MoS_2 and biological molecules. *Chem Sci. 9* (7), 1769–1773.

249. Ahmad, R.; Srivastava, R.; Yadav, S.; Singh, D.; Gupta, G.; Chand, S.; Sapra, S., Functionalized Molybdenum Disulfide Nanosheets for OD-2D hyrbid nanostructures: p^hotoinduced charge transfer and ehnaced photorspns. *J. Phys. Chem. Lett.* **2017,** *8*, 1729-1738.

250. Pagneux, Q.; Ye, R.; Chengnan, L.; Barras, A.; Hennuyer, N.; Staels, B.; Caina, D.; Avila Osses, J. I.; Abderrahmani, A.; Plaisance, V.; Pawlowski, V.; Boukherroub, R.; Melinte,

S.; Szunerits, S., Electrothermal patches driving the transdermal delivery of insulin. *Nanoscale Horiz.* **2020,** *5*, 663-670

251. Pillai, O.; Panchagnula, R., Transdermal delviery of insulin from poloxamer gel: ex vivo and in vivo skin permeation studies in rat using itontophoresis and chemical enhances. *J. Control. Release* **2003,** *89*, 127.

252. Abderrahmani, A.; Yengo, L.; Caiazzo, R.; Canouil, M.; Cauchi, S.; Raverdy, V.; Plaisance, V.; Pawlowski, V.; Lobbens, S.; Maillet, J.; Rolland, L.; Boutry, R.; Queniat, G.; Kwapich, M.; Tenenbaum, M.; Bricambert, J.; Saussenthaler, S.; Anthony, E.; Jha, P.; Derop, J.; Sand, O.; Rabearivelo, I.; Leloire, A.; Pigeyre, M.; Daujat-Chavanieu, M.; Gerbal-Chaloin, S.; Dayeh, T.; Lassailly, G.; Mathurin, P.; Staels, B.; Auwerx, J.; Schurmann, A.; Postic, C.; Schafmayer, C.; Hampe, J.; Bonnefond, A.; Pattou, F.; Froguel, P., Increased Hepatic PDGF-AA Signaling Mediates Liver Insulin Resistance in Obesity-Associated Type 2 Diabetes. *Diabetes* **2018,** *67* (7), 1310-1321.

253. Larsen, M. O.; Rolin, B., Use of the Göttingen minipig as a model of diabetes, with special focus on type 1 diabetes research. *ILAR journal* **2004,** *45* (3), 303-313.

254. Yu, J.; Wang, J.; Zhang, Y.; Chen, G.; Mao, W.; Ye, Y.; Kahkoska, A. R.; Buse, J. B.; Langer, R.; Gu, Z., Glucose-responsive insulin patch for the regulation of blood glucose in mice and minipigs. *Nature biomedical engineering* **2020,** *4* (5), 499-506.

255. Sterkers, A.; Hubert, T.; Gmyr, V.; Torres, F.; Baud, G.; Delalleau, N.; Vantyghem, M.; Kerr-Conte, J.; Caiazzo, R.; Pattou, F., Islet survival and function following intramuscular autotransplantation in the minipig. *American Journal of Transplantation* **2013,** *13* (4), 891-898.

256. Mura, S.; Nicolas, J.; Couvreur, P., Stimuli-responsive nanocarriers for drug delivery. *Nat Mater* **2013,** *12* (11), 991-1003.

257. Linsley, C. S. W., B.M. , Recent advances in light-responsive on-demand drug-delivery systems. *Ther. Deliv.* **2017,** *8* (2), 89-107.

258. Qiu, M.; Wang, D.; Liang, W.; Liu, L.; Zhang, Y.; Chen, X.; Sang, D. K.; Xing, C.; Li, Z.; Dong, B.; Xing, F.; Fan, D.; Bao, S.; Zhang, H.; Cao, Y., Novel concept of the smart NIR-light-controlled drug release of black phosphorus nanostructure for cancer therapy. *Proc Natl Acad Sci U S A* **2018,** *115* (3), 501-506.

259. Zhang, Y.; Wang, D.; Gao, M.; Xu, B.; Zhu, J.; Yu, W.; Liu, D.; Jiang, G., Separable Microneedles for Near-Infrared Light-Triggered Transdermal Delivery of Metformin in Diabetic Rats. *ACS Biomater Sci Eng* **2018,** *4* (8), 2879-2888.

260. Zhang, L.; Li, Y.; Jin, Z.; Yu, J. C.; Chan, K. M., An NIR-triggered and thermally responsive drug delivery platform through DNA/copper sulfide gates. *Nanoscale* **2015,** *7* (29), 12614-24.

261. Teodorescu, F.; Queniat, G.; Foulon, C.; Lecoeur, M.; Barras, A.; Boulahneche, S.; Medjram, M. S.; Hubert, T.; Abderrahmani, A.; Boukherroub, R.; Szunerits, S., Transdermal skin patch based on reduced graphene oxide: A new approach for photothermal triggered permeation of ondansetron across porcine skin. *J Control Release* **2017,** *245*, 137-146.

262. Altinbasak, I.; Jijie, R.; Barras, A.; Golba, B.; Sanyal, R.; Bouckaert, J.; Drider, D.; Bilyy, R.; Dumych, T.; Paryzhak, S.; Vovk, V.; Boukherroub, R.; Sanyal, A.; Szunerits, S., Reduced Graphene-Oxide-Embedded Polymeric Nanofiber Mats: An "On-Demand" Photothermally Triggered Antibiotic Release Platform. *ACS Appl Mater Interfaces* **2018,** *10* (48), 41098-41106.

263. Zhao, P.; Zheng, M.; Luo, Z.; Gong, P.; Gao, G.; Sheng, Z.; Zheng, C.; Ma, Y.; Cai, L., NIR-driven Smart Theranostic Nanomedicine for On-demand Drug Release and Synergistic Antitumour Therapy. *Sci Rep* **2015,** *5*, 14258.

264. Lu, H.; Zhang, S.; Guo, L.; Li, W., Applications of graphene-based composite hydrogels: a review. *RSC Advances* **2017,** *7* (80), 51008-51020.

265. Liao, G.; Hu, J.; Chen, Z.; Zhang, R.; Wang, G.; Kuang, T., Preparation, Properties, and Applications of Graphene-Based Hydrogels. *Front Chem* **2018,** *6*, 450.

266. Xu, Y. S., K.; Li, C.; Shi, G., Self-Assembled Graphene Hydrogel via a One-Step Hydrothermal Process. *American Chemical Society* **2010,** *4* (7), 4324-4330.

267. Fan, Z.; Liu, B.; Wang, J.; Zhang, S.; Lin, Q.; Gong, P.; Ma, L.; Yang, S., A Novel Wound Dressing Based on Ag/Graphene Polymer Hydrogel: Effectively Kill Bacteria and Accelerate Wound Healing. *Advanced Functional Materials* **2014,** *24* (25), 3933-3943.

268. Gong, P.; Ji, S.; Wang, J.; Dai, D.; Wang, F.; Tian, M.; Zhang, L.; Guo, F.; Liu, Z., Fluorescence-switchable ultrasmall fluorinated graphene oxide with high near-infrared absorption for controlled and targeted drug delivery. *Chemical Engineering Journal* **2018,** *348*, 438-446.

269. Tao, C.-a.; Wang, J.; Qin, S.; Lv, Y.; Long, Y.; Zhu, H.; Jiang, Z., Fabrication of pH-sensitive graphene oxide–drug supramolecular hydrogels as controlled release systems. *Journal of Materials Chemistry* **2012,** *22* (47), 24856.

270. Chen, M. C.; Lin, Z. W.; Ling, M. H., Near-Infrared Light-Activatable Microneedle System for Treating Superficial Tumors by Combination of Chemotherapy and Photothermal Therapy. *ACS Nano* **2016,** *10* (1), 93-101.

271. Yu, J.; Zhang, Y.; Kahkoska, A. R.; Gu, Z., Bioresponsive transcutaneous patches. *Curr Opin Biotechnol* **2017,** *48*, 28-32.

272. Pastore, M. N.; Kalia, Y. N.; Horstmann, M.; Roberts, M. S., Transdermal patches: history, development and pharmacology. *Br J Pharmacol* **2015,** *172* (9), 2179-209.

273. Viollet, B.; Guigas, B.; Sanz Garcia, N.; Leclerc, J.; Foretz, M.; Andreelli, F., Cellular and molecular mechanisms of metformin: an overview. *Clin Sci (Lond)* **2012,** *122* (6), 253-70.

274. Graham, G. G. P., J.; Arora,M.; Day, R. O.; Doogue, M. P.; Duong, J. K. ; Furlong,T. J.; Greenfield,J. R. ; Greenup, L. C. ; Kirkpatrick,C. M.; Ray, J. E.; Timmins, P. ; Williams, K. M. , Clinical Pharmacokinetics of Metformin. *Clin Pharmacokinet* **2011,** *50* (2), 81-98.

275. Zhang, Y.; Jiang, G.; Hong, W.; Gao, M.; Xu, B.; Zhu, J.; Song, G.; Liu, T., Polymeric Microneedles Integrated with Metformin-Loaded and PDA/LA-Coated Hollow Mesoporous SiO2 for NIR-Triggered Transdermal Delivery on Diabetic Rats. *ACS Applied Bio Materials* **2018,** *1* (6), 1906-1917.

276. Yu, X.; Jin, Y.; Du, L.; Sun, M.; Wang, J.; Li, Q.; Zhang, X.; Gao, Z.; Ding, P., Transdermal Cubic Phases of Metformin Hydrochloride: In Silico and in Vitro Studies of Delivery Mechanisms. *Mol Pharm* **2018,** *15* (8), 3121-3132.

277. Migdadi, E. M.; Courtenay, A. J.; Tekko, I. A.; McCrudden, M. T. C.; Kearney, M. C.; McAlister, E.; McCarthy, H. O.; Donnelly, R. F., Hydrogel-forming microneedles enhance transdermal delivery of metformin hydrochloride. *J Control Release* **2018,** *285*, 142-151.

278. Yu, W.; Jiang, G.; Zhang, Y.; Liu, D.; Xu, B.; Zhou, J., Near-infrared light triggered and separable microneedles for transdermal delivery of metformin in diabetic rats. *J Mater Chem B* **2017,** *5* (48), 9507-9513.

279. Lee, H.; Choi, T. K.; Lee, Y. B.; Cho, H. R.; Ghaffari, R.; Wang, L.; Choi, H. J.; Chung, T. D.; Lu, N.; Hyeon, T.; Choi, S. H.; Kim, D. H., A graphene-based electrochemical device with thermoresponsive microneedles for diabetes monitoring and therapy. *Nat Nanotechnol* **2016,** *11* (6), 566-572.

280. Li, J.; Mooney, D. J., Designing hydrogels for controlled drug delivery. *Nat Rev Mater* **2016,** *1* (12).

281. Madsen, A.; Bozickovic, O.; Bjune, J. I.; Mellgren, G.; Sagen, J. V., Metformin inhibits hepatocellular glucose, lipid and cholesterol biosynthetic pathways by transcriptionally suppressing steroid receptor coactivator 2 (SRC-2). *Sci Rep* **2015,** *5*, 16430.

282. Lai, Q.; Zhu, S.; Luo, X.; Zou, M.; Huang, S., Ultraviolet-visible spectroscopy of graphene oxides. *AIP Advances* **2012,** *2* (3), 032146.

283. Gong, P.; Du, J.; Wang, D.; Cao, B.; Tian, M.; Wang, Y.; Sun, L.; Ji, S.; Liu, Z., Fluorinated graphene as an anticancer nanocarrier: an experimental and DFT study. *J Mater Chem B* **2018,** *6* (18), 2769-2777.

284. Yang, K.; Wan, J.; Zhang, S.; Tian, B.; Zhang, Y.; Liu, Z., The influence of surface chemistry and size of nanoscale graphene oxide on photothermal therapy of cancer using ultra-low laser power. *Biomaterials* **2012,** *33* (7), 2206-14.

285. Turcheniuk, K.; Hage, C. H.; Spadavecchia, J.; Serrano, A. Y.; Larroulet, I.; Pesquera, A.; Zurutuza, A.; Pisfil, M. G.; Heliot, L.; Boukaert, J.; Boukherroub, R.; Szunerits, S., Plasmonic photothermal destruction of uropathogenic E. coli with reduced graphene oxide and core/shell nanocomposites of gold nanorods/reduced graphene oxide. *J Mater Chem B* **2015,** *3* (3), 375-386.

286. Im, I.-T.; Youn, S. B.; Kim, K., Numerical Study on the Temperature Profiles and Degree of Burns in Human Skin Tissue During Combined Thermal Therapy. *Numerical Heat Transfer, Part A: Applications* **2015,** *67* (9), 921-933.

287. Zhang, Y.; Jiang, G.; Yu, W.; Liu, D.; Xu, B., Microneedles fabricated from alginate and maltose for transdermal delivery of insulin on diabetic rats. *Mater. Sci. Eng. C. Mater. Biol. Appl.* **2018,** *85*, 18-26.

288. Press, M.; Jung, T.; Konig, J.; Grune, T.; Hohn, A., Protein aggregates and proteostasis in aging: Amylin and beta-cell function. *Mech Ageing Dev* **2019,** *177*, 46-54.

289. Ferreira, S.; Raimundo, A. F.; Menezes, R.; Martins, I. C., Islet amyloid polypeptide & amyloid beta peptide roles in Alzheimer's disease: two triggers, one disease. *Neural Regen Res* **2021,** *16* (6), 1127-1130.

290. Paul, A.; Kalita, S.; Kalita, S.; Sukumar, P.; Mandal, B., Disaggregation of Amylin Aggregate by Novel Conformationally Restricted Aminobenzoic Acid containing alpha/beta and alpha/gamma Hybrid Peptidomimetics. *Sci Rep* **2017,** *7*, 40095.

291. Jurgens, C. A.; Toukatly, M. N.; Fligner, C. L.; Udayasankar, J.; Subramanian, S. L.; Zraika, S.; Aston-Mourney, K.; Carr, D. B.; Westermark, P.; Westermark, G. T.; Kahn, S. E.; Hull, R. L., beta-cell loss and beta-cell apoptosis in human type 2 diabetes are related to islet amyloid deposition. *Am J Pathol* **2011,** *178* (6), 2632-40.

292. Bharadwaj, P.; Solomon, T.; Sahoo, B. R.; Ignasiak, K.; Gaskin, S.; Rowles, J.; Verdile, G.; Howard, M. J.; Bond, C. S.; Ramamoorthy, A.; Martins, R. N.; Newsholme, P., Amylin and beta amyloid proteins interact to form amorphous heterocomplexes with enhanced toxicity in neuronal cells. *Sci Rep* **2020,** *10* (1), 10356.

293. Miklossy, J.; Qing, H.; Radenovic, A.; Kis, A.; Vileno, B.; Laszlo, F.; Miller, L.; Martins, R. N.; Waeber, G.; Mooser, V.; Bosman, F.; Khalili, K.; Darbinian, N.; McGeer, P. L., Beta amyloid and hyperphosphorylated tau deposits in the pancreas in type 2 diabetes. *Neurobiol Aging* **2010,** *31* (9), 1503-15.

294. Kulas, J. A.; Puig, K. L.; Combs, C. K., Amyloid precursor protein in pancreatic islets. *J Endocrinol* **2017,** *235* (1), 49-67.

295. Pithadia, A.; Brender, J. R.; Fierke, C. A.; Ramamoorthy, A., Inhibition of IAPP Aggregation and Toxicity by Natural Products and Derivatives. *J Diabetes Res* **2016,** *2016*, 2046327.

296. Wang, S. S.-S.; Chen, Y.-T.; Chou, S.-W., Inhibition of amyloid fibril formation of β-amyloid peptides via the amphiphilic surfactants. *Biochimica et Biophysica Acta (BBA)-Molecular Basis of Disease* **2005,** *1741* (3), 307-313.

297. Findeis, M. A., Peptide inhibitors of beta amyloid aggregation. *Current topics in medicinal chemistry* **2002,** *2* (4), 417-423.

298. Nie, Q.; Du, X. G.; Geng, M. Y., Small molecule inhibitors of amyloid beta peptide aggregation as a potential therapeutic strategy for Alzheimer's disease. *Acta Pharmacol Sin* **2011,** *32* (5), 545-51.

299. Bachhuber, T.; Katzmarski, N.; McCarter, J. F.; Loreth, D.; Tahirovic, S.; Kamp, F.; Abou-Ajram, C.; Nuscher, B.; Serrano-Pozo, A.; Muller, A.; Prinz, M.; Steiner, H.; Hyman, B. T.; Haass, C.; Meyer-Luehmann, M., Inhibition of amyloid-beta plaque formation by alpha-synuclein. *Nat Med* **2015,** *21* (7), 802-7.

300. Griner, S. L.; Seidler, P.; Bowler, J.; Murray, K. A.; Yang, T. P.; Sahay, S.; Sawaya, M. R.; Cascio, D.; Rodriguez, J. A.; Philipp, S.; Sosna, J.; Glabe, C. G.; Gonen, T.; Eisenberg, D. S., Structure-based inhibitors of amyloid beta core suggest a common interface with tau. *Elife* **2019,** *8*.

301. Lu, J.; Cao, Q.; Wang, C.; Zheng, J.; Luo, F.; Xie, J.; Li, Y.; Ma, X.; He, L.; Eisenberg, D., Structure-based peptide inhibitor design of amyloid-β aggregation. *Frontiers in molecular neuroscience* **2019,** *12*, 54.

302. Pagano, K.; Tomaselli, S.; Molinari, H.; Ragona, L., Natural Compounds as Inhibitors of Aβ Peptide Aggregation: Chemical Requirements and Molecular Mechanisms. *Frontiers in Neuroscience* **2020,** *14*.

303. Neddenriep, B.; Calciano, A.; Conti, D.; Sauve, E.; Paterson, M.; Bruno, E.; Moffet, D. A., Short Peptides as Inhibitors of Amyloid Aggregation. *Open Biotechnol J* **2011,** *5*, 39-46.

304. Gao, N.; Sun, H.; Dong, K.; Ren, J.; Qu, X., Gold-Nanoparticle-Based Multifunctional Amyloid-β Inhibitor against Alzheimer's Disease. *Chemistry–A European Journal* **2015,** *21* (2), 829-835.

305. Liu, G.; Men, P.; Kudo, W.; Perry, G.; Smith, M. A., Nanoparticle-chelator conjugates as inhibitors of amyloid-beta aggregation and neurotoxicity: a novel therapeutic approach for Alzheimer disease. *Neurosci Lett* **2009,** *455* (3), 187-90.

306. Jha, A.; Ghormade, V.; Kolge, H.; Paknikar, K. M., Dual effect of chitosan-based nanoparticles on the inhibition of β-amyloid peptide aggregation and disintegration of the preformed fibrils. *Journal of Materials Chemistry B* **2019,** *7* (21), 3362-3373.

307. Guo, J.; Li, J.; Zhang, Y.; Jin, X.; Liu, H.; Yao, X., Exploring the influence of carbon nanoparticles on the formation of beta-sheet-rich oligomers of IAPP(2)(2)(-)(2)(8) peptide by molecular dynamics simulation. *PLoS One* **2013,** *8* (6), e65579.

308. Nedumpully-Govindan, P.; Gurzov, E. N.; Chen, P.; Pilkington, E. H.; Stanley, W. J.; Litwak, S. A.; Davis, T. P.; Ke, P. C.; Ding, F., Graphene oxide inhibits hIAPP amyloid fibrillation and toxicity in insulin-producing NIT-1 cells. *Phys Chem Chem Phys* **2016,** *18* (1), 94-100.

309. Loczechin, A.; Seron, K.; Barras, A.; Giovanelli, E.; Belouzard, S.; Chen, Y. T.; Metzler-Nolte, N.; Boukherroub, R.; Dubuisson, J.; Szunerits, S., Functional Carbon Quantum Dots as Medical Countermeasures to Human Coronavirus. *ACS Appl Mater Interfaces* **2019,** *11* (46), 42964-42974.

310. Nekoueian, K.; Amiri, M.; Sillanpaa, M.; Marken, F.; Boukherroub, R.; Szunerits, S., Carbon-based quantum particles: an electroanalytical and biomedical perspective. *Chem Soc Rev* **2019,** *48* (15), 4281-4316.

311. de Medeiros, T. V.; Manioudakis, J.; Noun, F.; Macairan, J.-R.; Victoria, F.; Naccache, R., Microwave-assisted synthesis of carbon dots and their applications. *Journal of Materials Chemistry C* **2019,** *7* (24), 7175-7195.

312. Yousaf, M.; Huang, H.; Li, P.; Wang, C.; Yang, Y., Fluorine Functionalized Graphene Quantum Dots as Inhibitor against hIAPP Amyloid Aggregation. *ACS Chem Neurosci* **2017,** *8* (6), 1368-1377.

313. Wu, J. B.; Lin, M. L.; Cong, X.; Liu, H. N.; Tan, P. H., Raman spectroscopy of graphene-based materials and its applications in related devices. *Chem Soc Rev* **2018,** *47* (5), 1822-1873.

314. Chandra, S.; Pradhan, S.; Mitra, S.; Patra, P.; Bhattacharya, A.; Pramanik, P.; Goswami, A., High throughput electron transfer from carbon dots to chloroplast: a rationale of enhanced photosynthesis. *Nanoscale* **2014,** *6* (7), 3647-55.

315. Liu, L.; Zhang, M.; Xiong, Z.; Hu, D.; Wu, G.; Chen, P., Ammonia borane assisted solid exfoliation of graphite fluoride for facile preparation of fluorinated graphene nanosheets. *Carbon* **2015,** *81*, 702-709.

316. Zhu, P.; Tan, K.; Chen, Q.; Xiong, J.; Gao, L., Origins of Efficient Multiemission Luminescence in Carbon Dots. *Chemistry of Materials* **2019,** *31* (13), 4732-4742.

317. Zhang, W.; Wang, Y.; Liu, X.; Meng, X.; Xu, H.; Xu, Y.; Liu, B.; Fang, X.; Li, H. B.; Ding, T., Insight into the multiple quasi-molecular states in ethylenediamine reduced graphene nanodots. *Phys Chem Chem Phys* **2017,** *19* (42), 28653-28665.

318. Zuo, W.; Tang, L.; Xiang, J.; Ji, R.; Luo, L.; Rogée, L.; Ping Lau, S., Functionalization of graphene quantum dots by fluorine: Preparation, properties, application, and their mechanisms. *Applied Physics Letters* **2017,** *110* (22), 221901.

319. Moriscot, C.; Richard, M. J.; Favrot, M. C.; Benhamou, P. Y., Protection of insulin-secreting INS-1 cells against oxidative stress through adenoviral-mediated glutathione peroxidase overexpression. *Diabetes & Metabolism* **2003,** *29* (2), 145-151.

320. Cheng, K.; Delghingaro-Augusto, V.; Nolan, C. J.; Turner, N.; Hallahan, N.; Andrikopoulos, S.; Gunton, J. E., High passage MIN6 cells have impaired insulin secretion with impaired glucose and lipid oxidation. *PLoS One* **2012,** *7* (7), e40868.

321. Khurana, R.; Coleman, C.; Ionescu-Zanetti, C.; Carter, S. A.; Krishna, V.; Grover, R. K.; Roy, R.; Singh, S., Mechanism of thioflavin T binding to amyloid fibrils. *J Struct Biol* **2005,** *151* (3), 229-38.

322. Tay, W. M.; Huang, D.; Rosenberry, T. L.; Paravastu, A. K., The Alzheimer's amyloid-beta(1-42) peptide forms off-pathway oligomers and fibrils that are distinguished structurally by intermolecular organization. *J Mol Biol* **2013,** *425* (14), 2494-508.

323. Liu, Y.; Xu, L. P.; Dai, W.; Dong, H.; Wen, Y.; Zhang, X., Graphene quantum dots for the inhibition of beta amyloid aggregation. *Nanoscale* **2015,** *7* (45), 19060-5.

324. Mukherjee, A.; Morales-Scheihing, D.; Salvadores, N.; Moreno-Gonzalez, I.; Gonzalez, C.; Taylor-Presse, K.; Mendez, N.; Shahnawaz, M.; Gaber, A. O.; Sabek, O. M.; Fraga, D. W.; Soto, C., Induction of IAPP amyloid deposition and associated diabetic abnormalities by a prion-like mechanism. *J Exp Med* **2017,** *214* (9), 2591-2610.

325. Hoppener, J. W.; Jacobs, H. M.; Wierup, N.; Sotthewes, G.; Sprong, M.; de Vos, P.; Berger, R.; Sundler, F.; Ahren, B., Human islet amyloid polypeptide transgenic mice: in vivo and ex vivo models for the role of hIAPP in type 2 diabetes mellitus. *Exp Diabetes Res* **2008,** *2008*, 697035.

326. Ma, Z. W., G.T., Effects of Free Fatty Acid on Polymerization of Islet Amyloid Polypeptide (IAPP) In Vitro and on Amyloid Fibril Formation in Cultivated Isolated Islets of Transgenic Mice Overexpressing Human IAPP. *Molecular Medicine* **2002,** *8* (12), 863-868.

327. &, D. T. M. M. T. S.; Kahn, S. Z. R. L. H. S. E., Islet amyloid formation is an important determinant for inducing islet inflammation in high-fat-fed human IAPP transgenic mice. *Diabetologia 57* **2014,** *57*, 1884-1888.

328. Ono, K.; Takahashi, R.; Ikeda, T.; Mizuguchi, M.; Hamaguchi, T.; Yamada, M., Exogenous amyloidogenic proteins function as seeds in amyloid beta-protein aggregation. *Biochim Biophys Acta* **2014,** *1842* (4), 646-53.

329. Kedia, N.; Almisry, M.; Bieschke, J., Glucose directs amyloid-beta into membrane-active oligomers. *Phys Chem Chem Phys* **2017,** *19* (27), 18036-18046.

330. Sun, X.; Liu, Z.; Welsher, K.; Robinson, J. T.; Goodwin, A.; Zaric, S.; Dai, H., Nano-Graphene Oxide for Cellular Imaging and Drug Delivery. *Nano Res* **2008,** *1* (3), 203-212.

331. Loessner, D.; Meinert, C.; Kaemmerer, E.; Martine, L. C.; Yue, K.; Levett, P. A.; Klein, T. J.; Melchels, F. P.; Khademhosseini, A.; Hutmacher, D. W., Functionalization, preparation and use of cell-laden gelatin methacryloyl–based hydrogels as modular tissue culture platforms. *Nature protocols* **2016,** *11* (4), 727-746.

332. Hill, S. A.; Benito-Alifonso, D.; Davis, S. A.; Morgan, D. J.; Berry, M.; Galan, M. C., Practical Three-Minute Synthesis of Acid-Coated Fluorescent Carbon Dots with Tuneable Core Structure. *Sci Rep* **2018,** *8* (1), 12234.

333. Mittal, A.; Garg, S.; Kohli, D.; Maiti, M.; Jana, A. K.; Bajpai, S., Effect of cross linking of PVA/starch and reinforcement of modified barley husk on the properties of composite films. *Carbohydr Polym* **2016,** *151*, 926-938.

334. Franz-Montan, M.; Serpe, L.; Martinelli, C. C. M.; da Silva, C. B.; Santos, C. P. d.; Novaes, P. D.; Volpato, M. C.; de Paula, E.; Lopez, R. F. V.; Groppo, F. C., Evaluation of

different pig oral mucosa sites as permeability barrier models for drug permeation studies. *European Journal of Pharmaceutical Sciences* **2016,** *81*, 52-59.

ABBREVIATIONS AND ACRONYMS

2

2D – two dimensional

A

Aβ – beta amyloid

ACE – angiotensin-converting enzyme

ACN – acetonitrile

ADA – American diabetes association

APP – amyloid beta precursor

AFM – atomic force microscopy

ARPE-19 – arising retinal pigment epithelia cells

B

BCF – β-cell function

BCM – β-cell mass

BGL – blood glucose level

BSA – bovine serum albumin

C

CAE – constant analyzer energy

CDD – charge-coupled device

cDNA – complementary DNA

Cl-CH_2COOH – chloroacetic acid

CMC – carboxymethylcellulose

CQDs – carbon quantum dots

CVD – cardiovascular diseases

D

DMEM – Dulbecco's Modified Eagle's medium

DNA – deoxyribonucleic acid

DLS – dynamic light scattering

DPN – diabetic peripheral neuropathy

E

Er:YAG – erbium-doped yttrium aluminium garnet laser

F

FDA – Food and Drug Administration

FA – formic acid

FBS – fetal-bovine serum

FITC – fluorescein isothiocyanate

FTIR – Fourier transform infrared

G

G6PC – Glucose-6-phosphatase, catalytic subunit

G6P – Glucose-6 Phosphatase

GAD – glutamic acid decarboxylase

GelMA – gelatin methacrylate

GI – gastrointestinal tract

GO – graphene oxide

GQDs – graphene quantum dots

Abbreviations and acronyms

H

HCl – hydrochloric acid

HDL – high-density lipoprotein

HFIP – 1,1,1,3,3,3-hexafluoro-2-propanol

hIAPP – human islet amyloid polypeptide

HIV/AIDS – human immunodeficiency virus infection and acquired immunodeficiency syndrome

H&E – hematoxylin and eosin

HeLa – Henrietta Lacks' immortal cells

HF – hydrofluoric acid

HPLC – high performance liquid chromatography

I

IAPP – islet amyloid polypeptide

IHH – immortalized human hepatocyte cells

INS-1 – rat insulinoma cell line

IU – international units

K

KBr – potassium bromide

L

LDL – low density lipoprotein

LPS – lipopolysaccharide

M

MA – methacrylic anhydride

MIN-6 – mouse insulinoma cell line

MNs – microneedles

MODY – maturity onset of the diabetes of the young

MoS_2 NSs – molybdenum (IV) sulfide nanosheets

μPsip – porous silicon-based microparticles

N

NaCl – sodium chloride

NaOH – sodium hydroxide

$NH_2NH_2•H_2O$ – hydrazine hydrate

NIR – near-infrared

NPs – nanoparticles

O

OCT – optimal cutting temperature

P

PAA – poly(acrylic acid)

PBS – phosphate buffer saline

PCR – polymerase chain reaction

PDMS – polydimethylsiloxane

PEG – polyethylene glycol

PEGDA – polyethylene glycol diacrylate

PM – personalized medicine

PVA – poly(vinylic alcohol)

R

rGO – reduced graphene oxide

rGO-COOH – carboxylated reduced graphene oxide

RNA – ribonucleic acid

RPM – revolutions per minute

RPLP0 – ribosomal protein lateral stalk subunit P0

S

SC – stratum corneum

SDS – sodium dodecyl sulfate

Se NPs – Selenium nanoparticles

SEM – scanning electron microscopy

SiC – silicon carbide

SWCNTs – single-walled carbon nanotubes

T

T1D – type 1 diabetes

T2D – type 2 diabetes

TBT – TATA-box binding protein

TDD – transdermal drug delivery

TEM – transmission electron microscopy

TGX – tris-glycine eXtended

ThT – thioflavin T

U

UV-Vis–ultraviolet–visible spectrophotometry

W

WHO – World Health Organization

X

XPS – X-ray photoelectron spectroscopy

Blank page